Radiation, optical, power flow, and electrical diagnostics at the Z Facility: layout and techniques utilized to operate in the harsh environment

T. J. Webb[1, a)], D. E. Bliss[1], G. A. Chandler[1], D. H. Dolan[1], G. Dunham[1], A. Edens[1], E. Harding[1], M. D. Johnston[1], M. C. Jones[1], S. Langendorf[2], M. Mangan[1], A.J. Maurer[1], C. A. McCoy[1], N. W. Moore[1], R. Presura[3], A. M. Steiner[1], M. Wu[1], D. A. Yager-Elorriaga[1], K. C. Yates[1]

[1]Sandia National Laboratories, P.O. Box 5800, Albuquerque, New Mexico, 87185, USA

[2]Los Alamos National Laboratory, P.O. Box 1663, Los Alamos, NM 87545, USA

[3]Nevada National Security Site, Albuquerque Operations, Albuquerque, New Mexico 87185, USA

[a)] Author to whom correspondence should be addressed: tjwebb@sandia.gov

Abstract

The Z Machine is a current driver producing up to 30 MA in 100 ns that utilizes a wide range of diagnostics to assess accelerator performance and target behavior conduct experiments that use the Z target as a source of radiation or high pressures. We review the existing suite of diagnostic systems including their locations and primary configurations. The diagnostics are grouped in the following categories: pulsed power diagnostics, x-ray power and energy (P&E), x-ray spectroscopy, x-ray imaging including backlighting, power flow, velocimetry, and nuclear detectors including neutron activation. We will also briefly summarize the primary imaging detectors we use at Z: image plates, x-ray and visible film, microchannel plates (MCP), and the Ultrafast x-ray imager (UXI). The Z shot produces a harsh environment which interferes with diagnostic operation and data retrieval. We term these detrimental processes “threats” of which only partial quantifications and precise sources are known. We summarize the threats and describe techniques utilized in many of the systems to reduce noise and backgrounds.

Table of Contents

List of Acronyms

ACD	Aerogel Cherenkov Detector
A-K	Anode-Cathode
APD	Avalanche Photodiode
APE	Axial Pinhole Imager
AR	Axially Resolving
CCP	Convex Crystal PEAS
CIDZ	Cathode Ion Detector on Z
CRITR	Compact, Rugged In-Chamber Transmission Spectrometer
CS	Center Section
CVD	Chemical Vapor Deposition (detector)
CVR	Current-Viewing Resistor
DH	Dynamic Hohlraum
DMP	Dynamic Material Properties
ECP	Elliptically-Curved PEAS
EHP	Electron-Hole Pair
EMI	Electromagnetic Interference
EMP	Electromagnetic Pulse
EOS	Equation of State
FCAP	Faraday Cup in Anode Post
FCUP	Faraday Cup
FOA	Final Optics Assembly
FOV	Field-of-View
GRH	Gamma Reaction History
HEDP	High Energy Density Physics

IDTL	Inductively-Driven Transmission Line
IP	Image Plate
IS	Intermediate Store (Capacitor)
LOS	Line-of-Sight
LTGS	Laser Triggered Gas Switch
LTS	Laser-Triggering System
MCP	Microchannel Plate
MCVD	MITL Chemical Vapor Deposition (detector)
MIF	Magneto-Inertial Fusion
MIP	Mirror Imager PEAS
MITL	Magnetically Insulated Transmission Line
MLM	Multi-Layer Mirror
MONSSTR	Multi-Optic Novel Spherical Crystal Spectrometer
MTG	Marx Trigger Generator
NTOF	Neutron Time-of-Flight
ODIN	One-Dimensional Imager of Neutrons
OTL	Output Transmission Line
P&E	Power and Energy
PCD	Photoconducting Detector
PDI	Photonic Displacement Interferometer
PDV	Photonic Doppler Velocimetry
PEAS	Plasma Emission Acquisition System
PF	Power Flow
PFL	Pulse Forming Line
PODD	Pinned Optically-Aligned Diagnostic Dock
PRT	Proton Recoil Telescope
RR	Radially Resolving
RS	Radiation Sciences
SCDI	Spherical Crystal Diffraction Imager
SEGOI	Self-Emission Gated Optical Imager
SID	Silicon Diode
SNR	Signal-to-Noise Ratio
SOI	Silicon-On-Insulator
SOPI	Side-On Pinhole Imager
SVS	Streaked Visible Spectroscopy
TEP	Total Energy and Power
TiGHER	Time-Gated High Energy Radiation (spectrometer)
TIPC	Time-Integrated Pinhole Camera
TIXTL	Time-Integrated Crystal Spectrometer
TLDs	Thermoluminescent Dosimeters
TREX	Time-Resolved Elliptical Spectrometer

TTI	Time Transit Isolator
UXI	Ultrafast X-ray Imager
VISAR	Velocity Interferometer System from Any Reflector
XRD	X-ray Detector or X-ray Diffraction
XRS3	X-ray Scattering Spherical Spectrometer
ZBL	Z Backlighter
ZLV	Z Line VISAR
ZR	Z Refurbished

I. Introduction

Diagnostics are an indispensable component of all experiments[1] that occur at the Z facility at Sandia National Laboratories. The Z machine[2] is an 80 TW, 22 MJ driver that applies up to 30 MA to a target within 100 ns, depending on the details of the target geometry, and transmission line configuration near the load. The number and complexity of the diagnostic systems have increased considerably in the twenty-six years since the PBFA2 accelerator was converted to Z. In early years, prior to when Z was converted to ZR in 2007 when wire arrays were the dominant load type, diagnostics were heavily focused on x-ray power and energy detectors. Focus has expanded considerably, especially to magneto-inertial fusion (MIF), and the need arose to expand existing x-ray spectroscopy, imaging, velocimetry, neutron diagnostics, and establish new capabilities such as radiography. The diagnostic systems currently fielded at Z are summarized here with a reasonable degree of completeness, even those which are exploratory and developmental. Other publications[3,4] describe some prior configurations and capabilities which may be now retired, subsumed, or displaced in favor of the existing systems.

Diagnostics at Z may perform (but are not limited to) the following set of tasks, many of which are essential to the primary goals of the experiment to which they are applied:

- Evaluate pulsed power current/voltage delivery and coupling to the Z target
- Measure the radiation source output and spectrum.
- Study the details of plasma, chemical or nuclear reactions, or material conditions near or at the target
- Incorporated as components of experiments that use the Z load as a radiation source or a method of producing high pressure on materials for equation of state (EOS) studies[5,6]. These experiments occur in the fundamental science realm[7,8,9] or applied to specific goals within applied science programs

The nominally planned 150 yearly shots at Z are divided up in over 100 campaigns (depending on how they are categorized) involving over two dozen principal investigators. At the risk of oversimplification, the majority of the load types at Z can be very generally categorized in the following types:

- Dynamic material properties (DMP). These use geometries using the Z load current to produce pressures on materials, shock or shock-less, from which EOS information on the material is obtained. The primary diagnostics are usually velocimetry, but other types are used such as x-ray diffraction. An example load is shown in Figure 1A.

- Power Flow (PF). Power Flow targets are designed to study current coupling to the load, plasma conditions in the MITLs, and current loss mechanisms[10]. Often non-imploding loads with carefully designed inductances are used. X-ray measurements are infrequently used, replaced by visible spectroscopy, localized current probes, faraday cups, and velocimetry. Figure 1B gives an example PF target.
- Magneto-inertial fusion (MIF). These utilize imploding loads that apply to the generation of neutrons or the study of geometries or physics applicable to MIF though not all loads are specifically designed to produce neutrons. Typical diagnostics include neutron detectors (when neutrons are predicted), x-ray imagers, and x-ray spectroscopy. An example MagLIF[11,12,13] load shown in Figure 1C. There are also a number of high energy density physics (HEDP) experiments at Z exploring instabilities and related plasma physics that use many of the same diagnostics.
- Radiation sciences (RS) targets. These loads emit a spectrum of x-rays of various intensities, yields, and ranges. Target spectra are considered "cold" or "warm" considering mainly of x-ray fluorescence from highly ionized plasmas with the dividing line somewhat arbitrarily drawn at about 10 keV. Many of these experiments are "application" shots where the x-ray source is used to drive effects localized in other cassettes or samples. A prime example is an "Opacity" experiment where the Z pinch produced by an imploding wire array both heats and backlights a wafer from which plasma opacity data is obtained[14,15]. For these loads and experiments, x-ray spectrometer and power and energy (P&E) diagnostics are the primary diagnostics besides the systems associated with driven physics experiments. Example loads include gas puff[16,17] the dynamic hohlraum (DH)[18,19], and wire arrays[20,21,22]. A picture of a DH load is shown in Figure 1D.

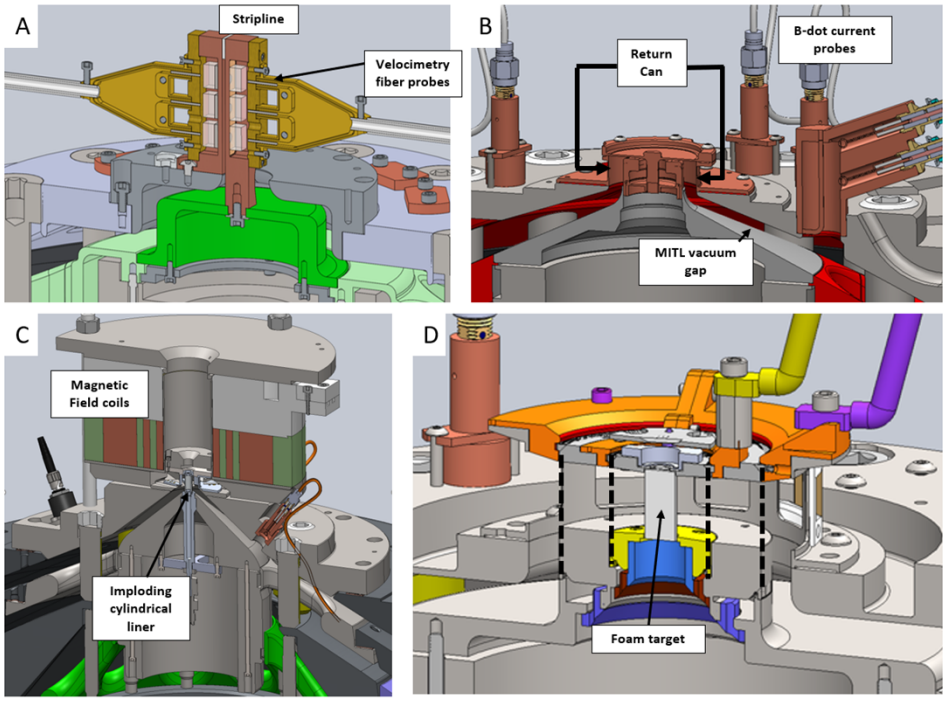

Figure 1. CAD models of A) a DMP, B) Power Flow, C) MagLIF (MIF), and D) Dynamic Hohlraum (RS) loads. In the last case, the radial posiions of the tungsten wires are shown as dashed lines.

Most of Z diagnostics can be grouped in several categories that are used in various combinations among the load types just mentioned:

- Velocimetry
- X-ray imaging
- X-ray power and energy (P&E)
- X-ray spectroscopy
- Soft x-ray backlighting (radiography)
- Visible spectroscopy and imaging
- Pulsed power and MITL current diagnostics
- Nuclear detectors

In this paper, we will group most diagnostics in these categories with a few exceptions. While the majority of the systems discussed are considered “mature,” several developmental systems will be included especially those which have, or are expected to, significantly expand capabilities. In addition, we will summarize in their own sections the main x-ray imaging technologies that span diagnostics and even categories of diagnostics.

Conditions that diagnostics must operate in at Z are particularly challenging and intense but do have features common to many other pulsed power facilities. Owing to the current densities at the load which exceed 2×10^8 A/cm^2 for a generic 5 mm diameter imploding liner, the load is always destroyed along with a significant portion of the inner MITL. The resulting debris environment is only a portion of the "threats" that diagnostics and other hardware are subject to before, during, and after a Z shot. We define a *threat* in the context of this paper as:

> a transient or steady-state property of the environment to which a diagnostic is exposed that produces a background or noise which significantly interferes with the primary signal, causes the system to "miss" the desired signal in space or time, or has the potential to destroy components to the extent that data cannot be processed sufficiently for the current shot or later intended use.

Whether or not a condition of the Z environment affects a given diagnostic depends very much on the associated context, intended use, and type of system. For instance, a fast radiation detector located far away from the load may not be strongly affected by shot debris on a single shot, and, even if it were, the needed signal is recorded before the debris could even reach the position. Types of threats include—but are not limited to—the following general types:

- Debris which can be subdivided into:
  - "Bullets": mm or larger scale fragments traveling at high velocity
  - Molten material
  - "Soot": dust-like material
- Electric-magnetic interference or pulse (EMI or EMP—one way to differentiate the two is whether the noise power or frequency is quasi-steady state or occurs on the approximate time scale of the desired measurement—both have been observed at Z)
- Hard x-rays (100's of keV to few MeV)
- Soft x-rays (< 50 keV)
- Ionizing particle beams (usually electrons or neutrons)
- Shock
- Physical displacement
- Vacuum conditions pre or post shot

In this paper we will exclude from further discussion as a threat radiological, chemical, or physical hazards to personnel or equipment associated with fielding, retrieving, or refurbishing diagnostics or supporting systems though users and designers must be familiar with these conditions and plan and operate accordingly. Many hazards of these types are more-or-less continually present at certain locations given the gradual accumulation of material or are produced on the Z shot and is later cleaned or disposed. One example is beryllium contamination which is assumed to exist—until proven otherwise—on any component fielded in, or connected to, the Z vacuum chamber. Numerous administrative and engineering controls exist to protect personnel, equipment, and the environment from these hazards. Some users may seek removal or reuse of equipment or material after a Z shot for which above protocols and requirements must be considered in coordination and approval of the appropriate Z personnel.

One of the challenges in discussions of the threat environment is the varying degree of quantitative measurements of them. There are considerable differences in target geometries and experimental conditions which produce widely different noise and background sources. Also, the threats tend to be very stochastic; for instance, the debris is spread out non-uniformly and is highly sensitive to the local geometry. While there have been diagnostic development efforts over the years with the intent to provide quantitative measures of the harsh environment in some contexts[23,24], they will not be a major focus of this paper. Instead, we use the experience gained from the design, use, re-use, and redesign (as required) of the diagnostics themselves to provide lessons of what is required to achieve the associated measurement and, as available, give some indication of the type and magnitude of the environment.

The harshest area of the harsh environment is, understandably, near the load region since this is where the current is concentrated, the z-pinch occurs, and the primary x-rays are generated. Many diagnostics are fielded far from the load to avoid these dangers. Some systems cannot be moved far away because they employ a geometry that requires certain distances or are not sensitive enough, so additional techniques are employed to enable their operation.

This paper will be organized in the following way. The general layout of the Z accelerator will be described with definition of the various "regions" where diagnostics are or may be fielded. Each region contains different types or levels of threats. The current mapping of the external LOS's is described. Then begins a more detailed discussion of the diagnostics, organized in their various classes or types, with the following types of information (though the degree of coverage varies):

- Principle of operation
- Purposes
- Most common configurations
- Locations where fielded
- Some information of system parameters (e.g., applicable energy ranges, typical energy resolution, number of available channels, etc.)
- Possible threats and mitigation measures applied

Space limitations do not allow for a full description of the physical makeup of each diagnostic or complete theory of operation. We will include limited example data for some of the diagnostics. Space limitations prevent description of data processing or how the data is applied to meet shot objectives. References will be given for more information on these topics though they will only be a sampling of the considerable literature built up over the years. For up-to-date information on the Z layout or diagnostics, the interested reader may contact the corresponding author or the current Z Diagnostic Scientist (or equivalent position) for configuration information. As the Z diagnostic systems are ever advancing, it is important to note that diagnostic systems or the Z configuration will continue to evolve and change over time with some systems or measurements being displaced in favor of higher priority diagnostics.

II. Z Diagnostic Layout

The locations of diagnostics and other systems at Z can be described or specified on a spherical coordinate system. A description of the coordinate system and orientation of the axes is shown in Figure 2. The physical space can be separated into discrete regions which strongly influence the space constraints, types of diagnostics, and, of course, signal levels given the proximity to the target load. The following sections will describe the primary regions in more detail. The specification of a diagnostic

location is usually specified by a LOS, or Line-of-Sight, and then an azimuthal angle as LOS ###. An azimuth of 0° approximately corresponds to geographic North. For an external LOS, a second dimension is added as the angle from the horizontal plane in the form LOS ###-0 or LOS- ###-12 for 0° and 12°, respectively. An example of this is LOS 50-12 (azimuthal angle of 50°, oriented 12° up) which is shown in Figure 3 and Figure 5.

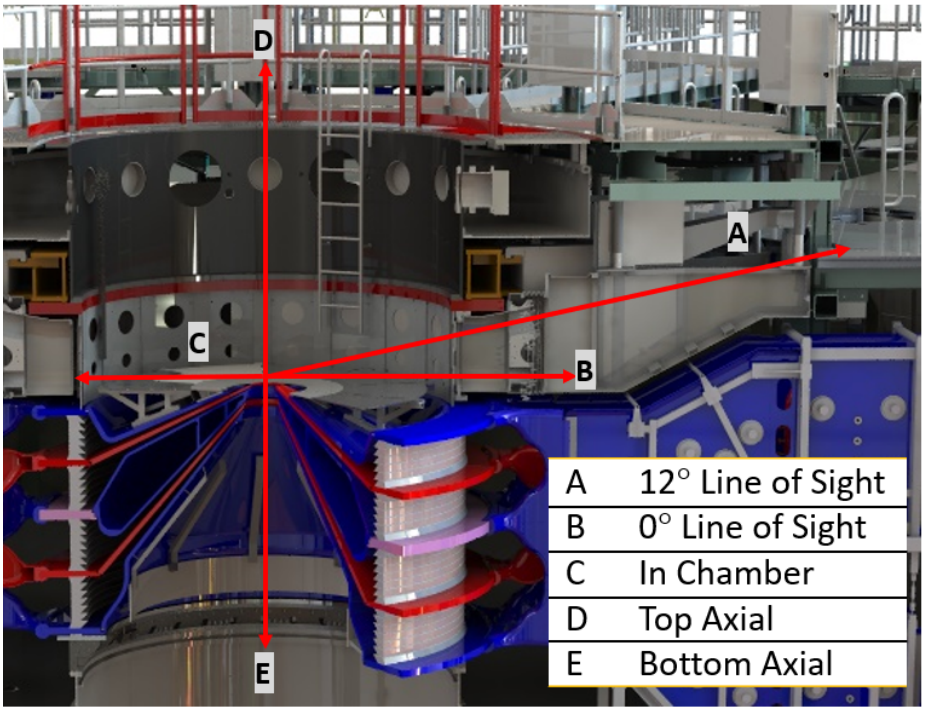

Figure 2. A model view of the coordinate system and locations at Z.

The space can be described on a simple radial scale which is useful for discussions of regions containing different parts of the hardware, diagnostic types, and varying threat types and levels. Figure 3 is a radial map showing the regions and radial distances of various boundaries and detectors which indicates the considerable broad scale of applicable areas from the load to the farthest detectors.

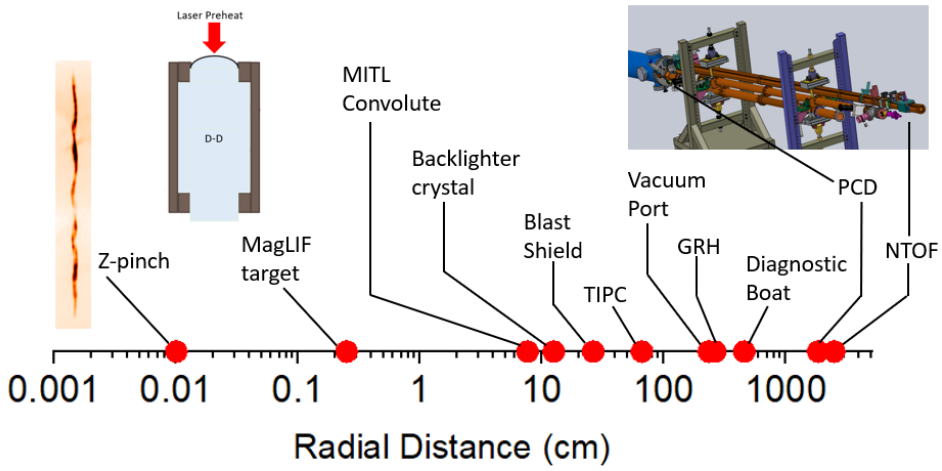

Figure 3. Radial positions of various boundaries and positions of some representative diagnostics.

There are many factors which determine the placement of specific diagnostics. First, signal levels must be matched to the specifics of the detector and system. Second, the view of the Z pinch may be limited in height or azimuthal location due to details of the target or some other obstruction. For example, a "return can" (see Figure 1B) is present for many Z target which, in general, is a direct metal connection from the cathode or liner to the outer anode; all targets have some form of return can—a possible exception is the "gas puff" where the implosion occurs in the ionized gas and the current return happens through wires stretched out above the gas nozzles. Some return cans are too thick for relevant x-ray transmission or related hardware block x-rays except through certain open or low attenuating areas. Third, a balance between signal levels and shielding must be reached which are, again, specific to the experiment and system. Lastly, some diagnostics are tied to external systems which are only available in certain locations. For each shot significant planning begins many months before shot day which accounts for, among other things, diagnostic views, signal levels, resolutions (spatial, temporal, and spectral), and systems interferences to meet primary and secondary shot objectives.

We will now briefly describe the primary regions where diagnostics (in general) are located. The specific (or general if there is flexibility) location for each diagnostic or diagnostic class will be listed in the associated section.

A. Center Section

The center section (CS) describes the cylindrical volume between the top and bottom lids and insulator stack. The Z load or target is located at the convergence of the radial magnetically insulated transmission lines (MITLs) at the center of CS. Most operational activities occur on the "MITL" deck which is a platform mounted above the top MITL anode. The MITL deck also is the support for most of the diagnostics in the chamber outside of the blast shield. The blast shield is a cylindrical structure which surrounds the Z load (see Figure 4). Various types of blast shields are used with different loads and

experiments providing varying degrees of diagnostics access and debris mitigation. For instance, a relatively wide-open blast shield is used for RS shots to maximize exposure area for experiments and diagnostics and the debris is relatively low. One common feature or function of blast shields is a top plate meant to limit upward travel of debris to protect the somewhat more vulnerable top vacuum lid. Figure 4 is a view of the CS deck plate with diagnostics and a blast shield for an MIF target. For in-chamber diagnostics, placement and alignment occurs during a defined time period before, during, or after the load installation before CS is sealed for vacuum. The inner wall of CS contains doors or ports which are opened, as required, to provide views of the load for the external LOS's.

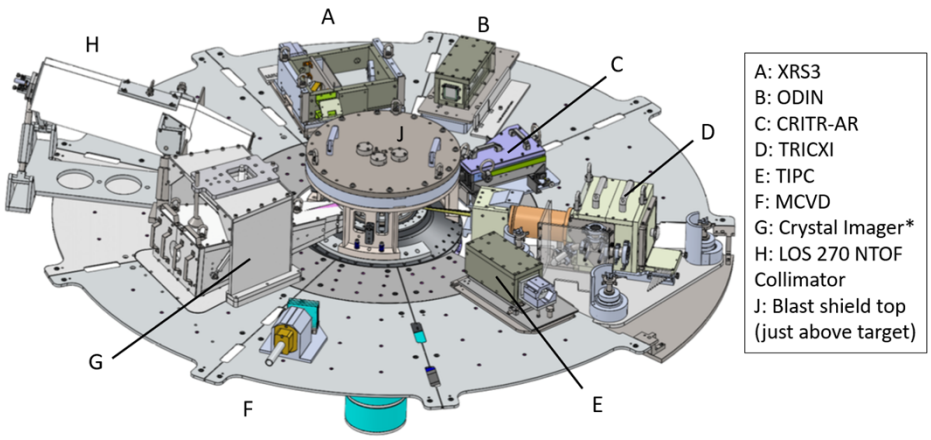

Figure 4. A "configuration summary" view of diagnostics or a MagLIF shot in the Z chamber or center section (CS) all pointing at the Z load located inside the blast shield in the center. The Crystal Imager (*) is a configurable shielded box for the detector that can be used for backlighting or self-emission imaging; the crystals are located inside the blast shield opposite the opening to the imager box.

Many diagnostics and associated support systems must be fielded in the CS because a large physical standoff is not compatible with the diagnostic operation. These include velocimetry probes which must be placed a few millimeters from the moving surface, so they must always be within the blast shield. Crystal imagers at Z only operate at distance scales of tens of centimeters, and the diffracting crystals are within the blast shield with the detector outside. Other imaging systems and spectrometers benefit significantly in signal strength when placed on the MITL deck. Still, mitigation measures must be in place to allow these systems to deal with the debris and x-ray backgrounds.

A. External LOS's

Outside of CS, diagnostic access is only available in discrete locations called Lines-of-Sight (LOS's). These may provide a direct view of the Z pinch outside of the chamber when geometry allows. The LOS's are only available through ports located in 20° increments starting at 10° with a smaller four-inch diameter port at 0° and an eight-inch diameter port at 12°. Table 1 lists the current allocation of systems and

diagnostics occupying these LOS's. In several cases, mostly in CS, there are permanent structures or vacuum connected lines tied to an external LOS which basically reserves that position (e.g., position on the MITL deck plate) for a particular diagnostic when used. Similarly, several external LOS's contain long-standing or frequently used systems which are not easily relocated, so those positions are reserved at all times. Some LOS's provide vacuum feed through ports for optical fibers or coaxial cables which are more easily converted or adapted for various purposes.

Table 1. External lines-of-sight (LOS) and present allocation to diagnostics and systems. Color coding refers to the type of connection to the chamber—gray = external to vacuum, green = vacuum extension tube beyond diagnostic boat, blue = location inside the boat, tan = cable/fiber/gas vacuum feed through in the boat. Systems in bold are not easily reconfigured for other purposes or are reserved.

LOS	0°	12°
10	**Gas Fill / Cryogenics**	
30	**VISAR / PDV**	
50	TRICXI / TiGHER	**P&E, NTOF**
70	**SVS (and other fibers)**	
90	**In-chamber cabling**	
110	**ZLV**	
130		**TIXTLs**
150	In-chamber cabling	
170	**P&E**	**MLM**
190	GRH, ACD	
210		**P&E**
230		UXI
250	In-chamber cabling	
270	NTOF collimator	**NTOF**
290	Wolter	
310	In-chamber controls or gas fill	**Be probes**
330		**TREX**
350	Gas Transfer System	

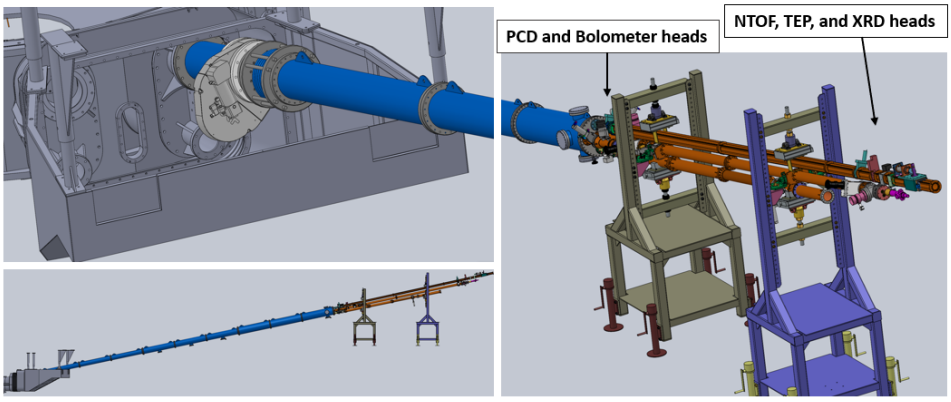

Figure 5. Upper left: model view of a diagnostic boat that provides access to the external LOS's and showing the case of the LOS 50-12 vacuum tube. Port covers of the other LOS positions are not shown. Right: downstream section of the LOS 50-12 pipe with diagnostic positions. Lower left: full view model view of boat and full LOS 50-12 vacuum pipe; the total length shown is about twenty-three meters.

B. Diagnostic boats

There are nine personnel access areas called "boats" providing admittance to most of the external LOS's though some LOS's extend beyond them. They are called boats because they are partially submerged in the Z water tank. A diagram of the boat and the interface to LOS 50-12 is shown in Figure 5. There are two sets of spools in the outer vacuum wall containing the 0° and 12° LOS's per spool. Direct view of the target at 0° is only possible in the lower part of the boat with the total radial distance at less than three meters. The 12° LOS provides a view of the target far beyond the boat. For instance, there are two vacuum pipes that extend beyond the boat at LOS 50-12 and LOS 210-12. TREX and MLM (Section IV-D) occupy permanent positions in other boats. Some diagnostics, such as the GRH (Section IV-G-4), are suspended from "I" beams at the roof of the boat (part of floor structure at the upper level).

C. Axial Package and FOAs

A view of the target above the load is available with one of three types of systems mounted on the top vacuum lid. The first system is called the "axial package"[25] which is shown in Figure 6. There are three attached vacuum lines, one at 0° and two others at ±9° on either side. Each of these are called "PODDs" for pinned optically aligned diagnostic dock. There are two sides of each PODD which can field a few types of plasma emission acquisition systems (PEAS) which was designed to provide capabilities similar to some of the systems mounted on the 12° LOS's; namely they are the CCP, ECP, and MIP. The CCP (convex crystal PEAS) are like the TIXTLs, the ECP (elliptically curved PEAS) are roughly equivalent to TREX, and the MIP (mirrored imager PEAS) are similar to the MLM (see associated sections for more details on each). Each PODD provides a location for a pair of P&E detectors (Section IV-B) detectors as well.

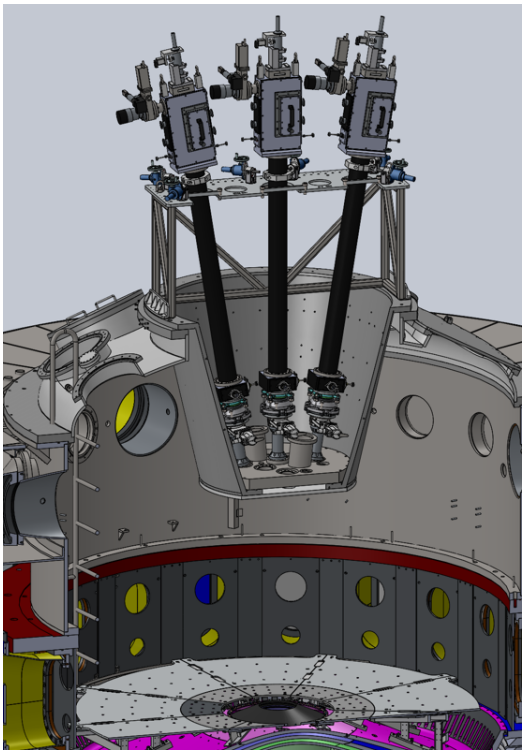

Figure 6. Model view of the Axial Package. The upper level of vacuum chamber, in particular the MITL deck, is shown but no load.

Another set of systems is used along with the Beamlet laser called FOAs (final optics assemblies) of which there are two types. One, called the "vacuum FOA," contains the final focusing element for the Beamlet laser[26] used for MagLIF preheat[27] and x-ray diffraction and is shown in Figure 7. The other is used for laser x-ray backlighting (Section IV-D-5) and is shown in Figure 7. The vacuum FOA contains five ports available for pinhole cameras, P&E detectors, and other similar diagnostics. It is common to field UXI cameras with pinhole cameras there along or silicon diodes to diagnose the pre-heat plasma conditions on MagLIF.

Alignment to the Z target may be made under vacuum in the case of the Axial Package or backlighter FOA but must be done prior to vacuum in the case of the vacuum FOA. Threats to diagnostic systems in these locations are generally relatively low except for small "bullets" that sometimes destroy crystals and breach thin filters. The FOAs employ glass windows to protect the interior from debris. Hard x-ray backgrounds may occasionally be a concern for time-integrated detectors in the Axial Package.

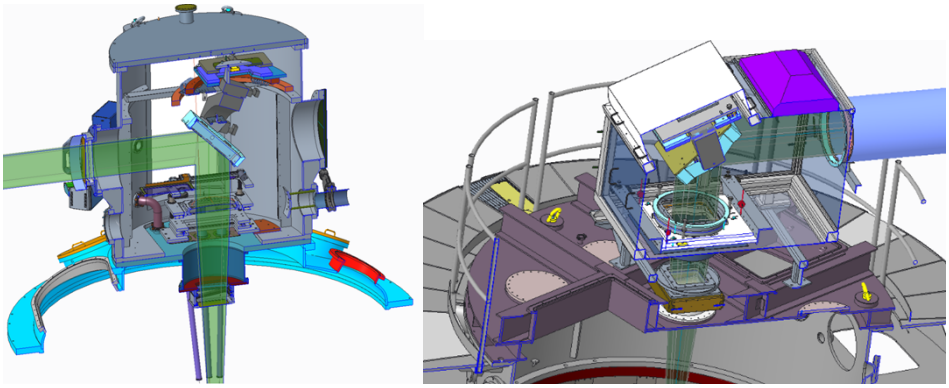

Figure 7. Left: vacuum final optics assembly (FOA) cut away view with the laser beam path shown in green; the input laser beam pipe is not shown. Right: backlighter FOA.

D. Bottom Side

The primary measurement made from below the load is the bottom NTOF (Section IV-G-2) or neutron activation samples. There is capability to field optical fibers for (point) VISAR and PDV (Section IV-F), and about a dozen electrical signals can be recorded going through the bottom lid connected to faraday cups, B-dots, Rogowski coils, and similar signals that cannot be sent via coaxial line to the topside of Z. A Time-Transit Isolator (TTI), shown in Figure 8, allows direct cable connection to the inner MITL cathode with minimal current loss (<1% of total load current) through inductive isolation. The TTI consists of a group of cables and gas lines fed together through a large, looped conduit forming an inductor. EMI is low through the bottom side connection and inside the screen boxes though other backgrounds are seen to exist but are not well known in terms of their source. Section IV-E-5 describes the CIDZ system which was able to mitigate a particular threat which strategy could be applied to other systems.

Figure 8. Photo of the time-transit isolator (TTI) installed on the bottom vacuum lid. A braid cable bundle connected to the load cathode is shown at top.

III. The harsh Z environment for diagnostics and general mitigation techniques

There are various forms of threats that impact diagnostics and other systems which either interfere with their data or impose damage that affect their later use. Even though these conditions at various levels have existed ever since Z (and its predecessors) have operated, there is limited quantified data to report since "noise" is seldom a focus of research or peer-review but is mainly only something to minimize. Also, the types of shots and associated hardware vary considerably which complicates the collection and study of relevant data regarding the threats. The number and type of diagnostics, especially within the vacuum chamber, have grown considerably since Z has been in operation. For instance, the introduction and the regular successful operation of time resolved detectors in the vacuum chamber such as UXI (Section IV-H-4) was a process that took more than one year to develop methods to reduce electric noise that interfered with triggering and chip readout and minimizing likelihood of debris destroying the sensor. Also, a general trend is that new diagnostics have thicker and more comprehensive tungsten shielding surrounding the sensitive components than previous similar versions—one inch tungsten is not always sufficient.

General diagnostic development for a given system usually proceeds along these lines:

1. Base a design with details, such as shielding or cable routing, on a previously functioning system based on measured or calculated source output and desired or expected signal. Often, simulations are used to inform the design and expected measurement but seldom consider external noise types. It is also common to use shielding or infrastructure from systems.
2. Using a first version of a diagnostic, background measurements or preliminary data are taken, and failure rates or signal-to-noise ratios (SNRs) are observed.
3. When needed, introduce improvements based on operational experience until acceptable results are achieved.

This section describes some details of threat conditions that have been observed to exist and some general mitigation strategies according to this method. Instrument-specific methods will be mentioned later in many of associated diagnostic sections.

A. X-ray backgrounds

X-ray backgrounds can be split in categories of energy or its source. Soft x-rays in the 10's of keV or less are generated from the Z pinch. When they are not desired as part of the intended measurement, they are usually easy to shield out or are deliberately not "passed" by design of the diagnostic. However, in some diagnostics, such as with bent crystal spectroscopy where some form of focusing of a particular x-ray energy is used by design, these soft x-rays may produce an unfocused background. "Hard" x-rays which extends to the gamma ray level (hundreds of keV or more) may or may not be directly produced by the Z pinch. These often require more robust shielding methods even though the total yield of these photons may be relatively small. The magnitude and spectra of these hard x-rays vary widely. An example spectrum inferred[28] from arrays of filtered thermoluminescent dosimeters (TLDs) are shown in Figure 9 where it is presumed that the Z pinch is the source of these x-rays. In this case it was a wire array load; high energy x-rays from other targets will certainly be different in spectral shape and magnitude where they occur. Other hard x-rays have been observed that are unlikely to come from the Z target either because the load is non-imploding, or the timing of these x-rays occur before the load could implode. An example showing the timing of a hard x-ray burst along with the MITL current pulse is shown in Figure 10. The precise source of these x-rays is currently under study, but the most likely source is inner MITL current loss between the convolute and the load. The peak x-rays appear to be produced at a point in the Z current rise time where the inner MITL voltage is near its peak; therefore, bremsstrahlung radiation from electrons crossing the MITL A-K gap is a strong possibility. SIDs fielded beyond the blast shield along the MITL deck near 0° do not appear to observe this pulse, but detectors inside the blast shield and other detectors far away at 12° often do see it. This suggests a significant degree of self-shielding at "low elevation" due to the MITLs and other hardware.

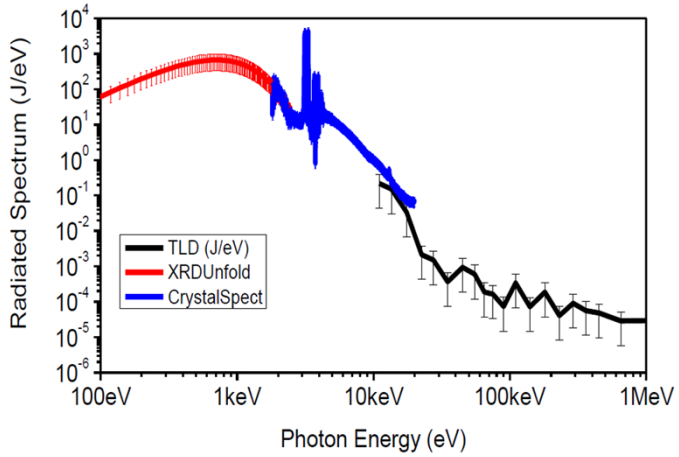

Figure 9. Combined x-ray spectrum of a wire array load. Reproduced from V. J. Harper-Slaboszewicz, *et al*., "Coarse spectral characterization of warm x-rays at the Z facility using a filtered thermoluminescent dosimeter array", Review of Scientific Instruments 88, 043501 (2017), with permission from AIP Publishing.

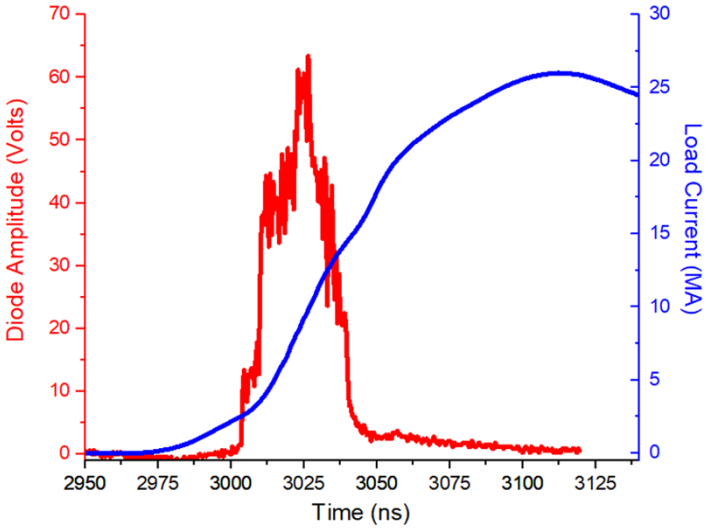

Figure 10. A heavily filtered silicon diode waveform (red) showing an example of the hard x-ray timing of a power flow load (Z3569) and the load current pulse (blue).

It has been an open question for many years just how much x-ray shielding is required for diagnostics fielded in the Z chamber. Experience has suggested the “one-inch tungsten” rule-of-thumb minimum standard for enclosures in the Z chamber containing image plates. TIPC and CRITR are examples where

this standard seems to be sufficient to produce backgrounds on the image plates near the noise level of the detector. X-ray shielding takes the form of a general "box" holding the detector such as an image plate and other components such as a crystal or pin hole pack; this is where the "one-inch tungsten" rule is commonly applied. Additional shielding is often spaced out in the form of baffles (see Figure 33 for an example used in TIPC or SOPI, Figure 35) in the direction of the target to limit the fluence of x-ray entering the shielded box. Often, more attenuation than one inch of tungsten is included in the forward direction. For instance, a >25% decrease in background levels has been observed when adding an additional one inch of tungsten inside the XRS3 (Section IV-C) box, but this was only a limited test case. Nevertheless, many diagnostics designed over the last few years such as MONSSTR and SOPI have deliberately included effectively > 1" of tungsten in the direction of the load.

In recent years, time gating has been applied vary effectively to remove x-ray backgrounds that occur at a different time than the desired signal. For instance, UXI cameras fielded in the Axial Package coupled to CCP spectrometers (Section IV-C) have improved the SNR for Opacity measurements[29]. Similarly, time gating may be applied to backlighting measurements (Section IV-D-5) to remove the self-emission of the Z target. In most cases, the UXI or MCP detectors still must survive other threats such as debris or EMI to return data.

B. Hardware debris

For many Z targets, much of the hardware within the convolute is destroyed on the shot. Figure 11shows example load hardware before and after the shot. For many targets, the anode hardware is ballistically launched from the convolute, which requires >4000 g's of force[30]. Accelerometer measurements have determined that the vertical force exceeds 17,000 g's, which is similar to the launch force of large-caliber artillery shells. Besides large pieces of hardware that disassemble from the rest of the inner MITLs, various other debris are produced which can be classed as hot plasma, vaporized material, melted metal, and mm-scale high speed "bullets" which have been observed to penetrate 0.25 inches of steel or millimeters of tungsten. Other objects not directly attached to the load but placed near or above the load can become debris sources themselves of potentially greater impact to external systems. Figure 12 shows the impact of a large piece of debris onto a diagnostic at 36.2 cm which is just outside of the blast shield; from the direction of the impact, it appears to have originated from a new diagnostic fielded above the Z target whereas on other shots there were few, if any, similar issues of this scale. In this particular case, the impacted diagnostic was a calorimeter (Section IV-B-2-f). Because the calorimeter is a "slow" measurement given thermal diffusions times on the order of a few milliseconds, the measurement could not outrun the debris. This is one lesson that inclusion of new hardware may introduce new threats beyond the level previously experienced.

Figure 11. Left: A DMP load hardware set photo before the shot. Right: large pieces of the remainder of the hardware post shot (some physical rearrangment of the items prior to the photo occurred).

Fortunately, shielding designed for x-rays and debris are usually mutually beneficial. Based mostly on experience over the 3700+ shots on Z thus far, hardware located within the blast shield—with a outer radius of about 30 cm--is presumed to be effectively destroyed or too heavily contaminated to be reused, but shielded containers outside of the blast shield are often reusable with varying levels of refurbishment and component replacement. The baffle systems, mentioned previously, are often very effective. TIPC is a good example which has a baffle system (shown in Figure 33) which consists of three stainless steel angled "Chevrons" with openings for the x-rays. Three 0.5 mm Kapton sheets are spaced out between these plates. The steel plates survive many shots and the Kapton sheets are replaced every time. Pin holes can be effective as debris mitigation because if debris were to impact the pin hole plate, the material effectively "plugs" the openings which often protects downstream components such as the detector as long as the debris does not penetrate the entire pin hole substrate. APE, SOPI and TRICXI use this technique.

One method that has been used at Z (mostly prior to ZR) was the use of "fast closure valves" to prevent hot gases from traveling up the LOS 50 pipe (or its earlier equivalent). Presently, no similar valves are in use at Z on any of the external LOS's. As needed or as part of planned maintenance, detector heads, baffles, pin hole plates, and similar items that "catch" debris are cleaned or have necessary components replaced.

Figure 12. A "bullet" debris impact hole onto the calorimeter housing. The direction of the hole suggests that the impacting object was not part of the primary load hardware but likely came from another "ride-along" diagnostic test suspended above the load. The calorimeter data was corrupted by this impact.

C. Electrical Noise

In many cases, the precise origin of sources of electrical noise encountered at Z is not known precisely nor is it known how it enters the signal path. In some circumstances and locations, the timing of noise can be correlated to the firing of some pulsed power components. Even cables that are tied together at the external ground or run along similar paths exhibit different noise levels and frequencies by a factor of several. It is not proven, but loose cable connections may be to blame in some cases. Cable connections inside the chamber are almost exclusively SMA. Cable connections outside the vacuum feedthroughs or on the atmosphere side may be SMA or N including QMA or QN adapters. In a few cases on an infrequent basis, SHV cables are used because signal cables were adapted from low frequency control or high voltage (biasing) cables. BNC connections are almost never used except inside the screen boxes or screen rooms, most commonly at the oscilloscopes. A large variety of cable types and lengths are used at Z including 0.5 inch diameter HELIAX, RG-214, LMR-400, LMR-240, or RG-405 (mostly in-chamber). It is common practice to wrap signal cables in additional copper or steel braid.

Experience has established a general noise floor of approximately 50 mV generally achievable outside of the Z vacuum chamber, but lower noise is possible. Inside the Z vacuum chamber, the results are more variable. The "grounded" anode above the MITL is likely not well connected to external grounds; therefore, ground loops may exist. However even cables fully isolated from the internal vacuum chamber metal (until the chamber wall vacuum cable feed through) still may see significant noise. The largest electrical noise is not necessarily located in the chamber either. The timing of the noise introduction in the signal can be correlated to signals in various components in the pulsed power system. Figure 13 shows a case where silicon diodes were placed in the chamber to measure the x-ray

backgrounds (not a focus of this discussion). The inset plot shows the voltage of a pulsed power component upstream of the chamber (see Section IV-A for the location and type of probe) from which some correlation of timing and a comparison of the frequency content (noise periods and rise-times on the order of 80 ns) can be made. However, we cannot prove at this time that the output transmission line (OTL) is the "cause" of the noise. Many other noise sources may exist in the Z facility on this order of amplitude or have higher frequency, but it is usually possible to avoid it. Digitizer noise (i.e., "bit noise") is always present at some level. A large percentage of the scopes at Z have eight bits of digital resolution though the "effective number of bits" is reduced from that, often around six bits. The black curve in Figure 13 illustrates a case where the scope settings where set to a lower sensitivity so that bit noise is more apparent. Nevertheless, we strive to optimize the scope settings given the expected signal level as much as possible.

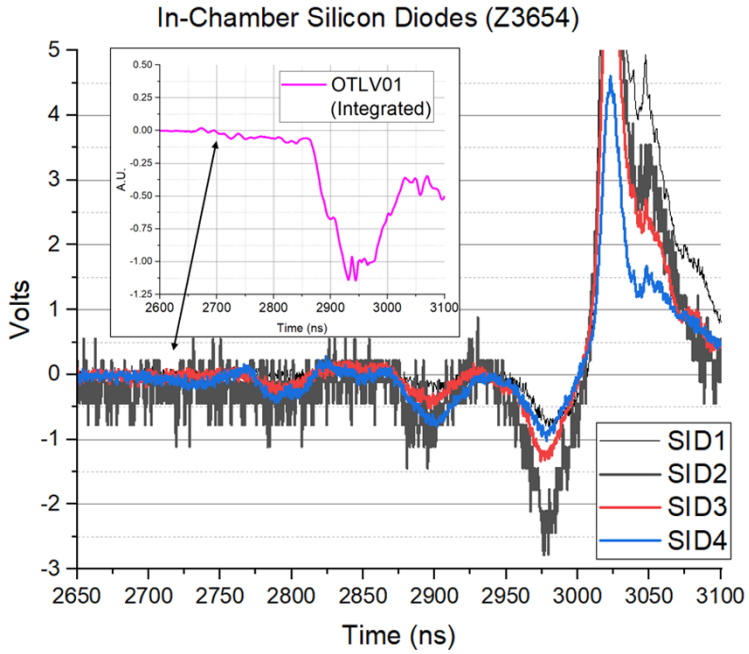

Figure 13. Example of noise correlated to a pulsed power component. The SIDs are in-chamber diodes measuring the hard x-ray background.

The following techniques have been incorporated at various locations at Z to reduce electrical noise:

- Double shielded or solid-jacketed coaxial cables (most in-chamber cables are semi-rigid RG-405 cables)
- Added metal braid around the cables.

- Multiple ground points between end termination (detector) in the form of patch panels and vacuum feed throughs which may reduce high frequency noise.
- Lower frequency noise may be reduced by a true single point ground connection only at the digitizer in a shielded screen box where the coaxial cable is electrically isolated within a rubberized metal jacket and the cable termination at the detector is electrically "floating" (including the detector). This is not commonly implemented at Z, but in the case utilized, this seemed to reduce the noise to < 10 mV.

Methods to reduce noise such as using baluns, subtracting "null" signal cables, or averaging signals with opposite detector polarity have some but limited utility at Z. The noise may have different timing and amplitude even if the frequency content is similar. MITL or load currents (as determined by B-dots as described in Section IV-A) are calculated by averaging the signals from sensors at different azimuthal locations though some degree of expert evaluation is often used to choose signals that seem to be functioning normally (bad cable connections are the most common failure mechanism which can be difficult to repair in some locations).

D. Vacuum conditions

Some diagnostics and systems may be sensitive to the atmospheric conditions in the vacuum chamber. For instance, MCPs in the MLM require operation at $< 1\times10^{-5}$ Torr for hours before the shot and must be protected from direct exposure to Z debris to be reusable; therefore, independent vacuum systems or localized pumps are used for MCPs. Motors such as used in turbomolecular pumps and or other electrical systems that are normally used in atmosphere, cannot be directly used in vacuum because heat cannot dissipate fast enough. Figure 14 is an example of the Z chamber vacuum history before and after a shot. Another example is the calorimeter (Section IV-B-2-f) which records data for many seconds after the Z shot and can be affected if the gas pressure cools the sensing element too quickly. The vacuum pressure according to the ion gauge increases to several mTorr immediately after the shot (low enough for the calorimeter).

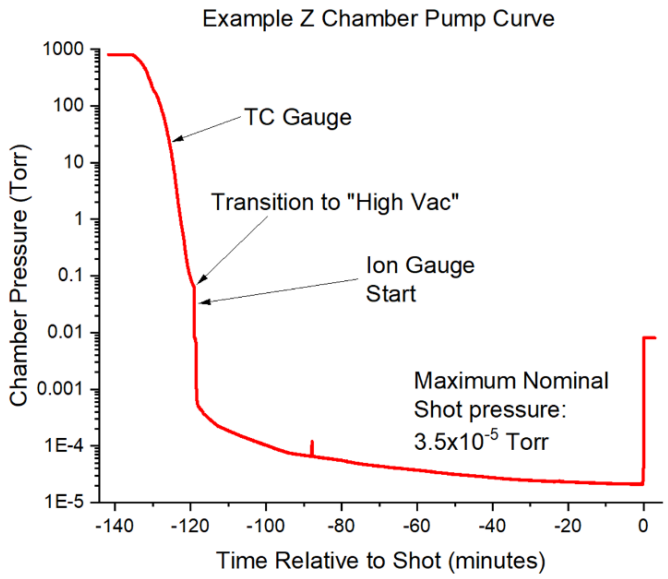

Figure 14. An example gas pressure time history of the Z vacuum chamber with time = 0 being shot time. It is common for time under "high vac" to be longer for various reasons, so this should be considered a minimum practical duration after the initiation of vacuum pumping.

IV. Z Diagnostic Systems

We will now discuss the details of the diagnostic systems at Z organized primarily according to purpose.

A. Z Pulsed Power Diagnostics

Pulsed power diagnostics are critical in understanding the performance and timing of Z's pulsed power system. There are nearly 500 deployed monitors recorded on fast-transient digitizers that will be discussed in this section.

Over 481 monitors cover various sections of the Z pulsed power system. Below is a summary of the sets of diagnostics used on a standard basis to evaluate the magnitude of current delivery from the Marxes to the load and its timing. The timing of the thirty-six modules can be monitored and compared to each other since their variance affects the final pulse shape and the absolute time of the load implosion. (As a quick aside: many time-resolved diagnostics presume a particular load timing. A high variance of shot timing or jitter introduces risk of full or partial data loss which could be termed another diagnostic risk.) A module consists of an individual Marx (containing sixty 2.6 microfarad 100 kV capacitors and SF_6 switches), an intermediate storage capacitor (IS), a 6 MV laser-triggered output switch, and pulse-forming line. A pair of modules combine at an output transmission line which connects to one of four levels on the insulator stack. These components are shown in Figure 15). It can also be helpful to note the timing of these components in case they are a source of noise on other electrical signals. Figure 16

Commented [JM1]: I think this should be capitalized Marx, Marxes.

shows portions of these signals with arbitrary scaling indicating the timing on the "Z time scale." The Z standard short pulse (± 85 kV charge on the Marxes) has peak load current around 3100 ns.

We will now briefly summarize the pulse forming process along with the primary monitors. Table 2 gives the names of these monitors. On the table, a monitor is affirmatively listed as "calibrated" if there is historical or recent data on its calibration or that it has the potential to be calibrated using analytic or cross-comparison methods even if the current values are unknown or not considered accurate. Once the Marxes are charged and connected to the downline chain, a primary trigger generator (called the LTS-100) sends high voltage pulses to nine Marx trigger generators (MTGs). This pulse is monitored by two B-dot monitors. The MTG pulses that trigger the Marxes are monitored by current viewing resistors (CVRs). The Marxes are then "erected" and the voltage is multiplied[31]; the output current of each Marx is monitored by CVRs. The IS is directly fed by a Marx, and the voltage of the IS is monitored with a capacitive voltage monitor (V-dot). The gas switches are triggered by 20 mJ, 266 nm lasers the timing of which is monitored by biased photodiode which is the primary means of checking switch timing. The breakdown of the switch is also detectable via the IS V-dots. The current and voltage of the PFLs and OTLs are also measured to verify their proper operation and timing. It should be mentioned that various self-breaking gaps and gas pressures must be set properly for effective timing. LTGS jitter is measured as a departure from the nominal arrival of energy to the PFL to the actual start-of-voltage time measured by the PFL V-dot monitor. Typical jitter is 10 ns (one-sigma) with a nominal full timing spread of less than 25 ns.

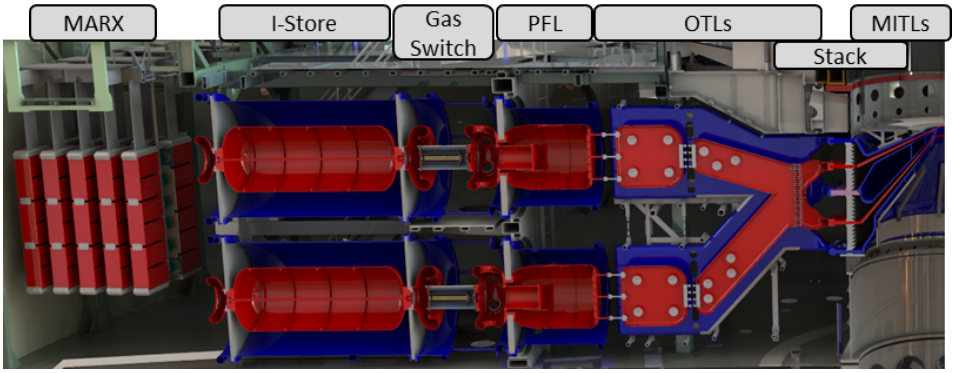

Figure 15. A model view of Z pulsed power section with main components or regions listed.

Voltages and currents are monitored at 18 azimuthal locations at the stack at each level. The timing and spread of a significant flashover event at the stack can be viewed with these monitors. The current then flows via MITLs toward the convolute. Marx current on the anodes is monitored at the top and bottom in the outer MITLs. Within the twelve post-hole convolute, currents are only monitored at the anode via B-dots, normally ~7.5 cm from the load[32]. There are several designs of B-dots at this location which have varying sensitivities and susceptibilities to noise, particle bombardment, and other effects which introduce errors in the current measurement. All standard current measurements using B-dots or Rogowski coils (also V-dot probes elsewhere) are *software integrated* or numerically post-processed to

return current waveforms rather than using hardware integrators. Section IV-E-4 describes the most recent efforts to improve these current probes using what is called IDTLs.

Table 2. Pulsed power monitors with names. "XX" is a place holder for numbers corresponding to monitor location. Calibration is a loose term indicating whether a monitor is just used for timing (i.e., "No"), or it is, or has the potential to, return absolutely-scaled data regardless of whether it is done in practice.

Location, type	Monitor name	Number of azimuthal locations	Calibrated	Total Signals
LTS-100, current, timing	LTS101, LTS102 xxxCUR (current)	2 systems	No	4
	LTS101, LTS102, PD (photodiode)			4
MTG, current	MTG00x	9	No	9
Marx, current	MRXCVRxx	36	No	36
IS, voltage	ISVDxx	36	No	36
LTGS, timing	TMPSTxx (laser photodiode)	36	N	72
	LSD_xx (switch gap photodiode)			
PFL, voltage	PFLVxx	36	N	36
OTL (1 and 2), voltage	OTL1Vxx	36	No	108
	OTL2Vxx			
	OTL2Bxx			
Vacuum insulator, voltage	VSAxxx, VSBxxx, VSCxxx, VSDxxx	18	Yes	72
Vacuum insulator, current	BSAxxx, BSBxxx,	18	Yes	72
	BSCxxx, BSDxxx			
Outer MITL, current	BMAxxx, BMDxxx	8	Yes	16
Inner MITL, current	BI(Type)(Azimuth)	Up to 16	Yes	16

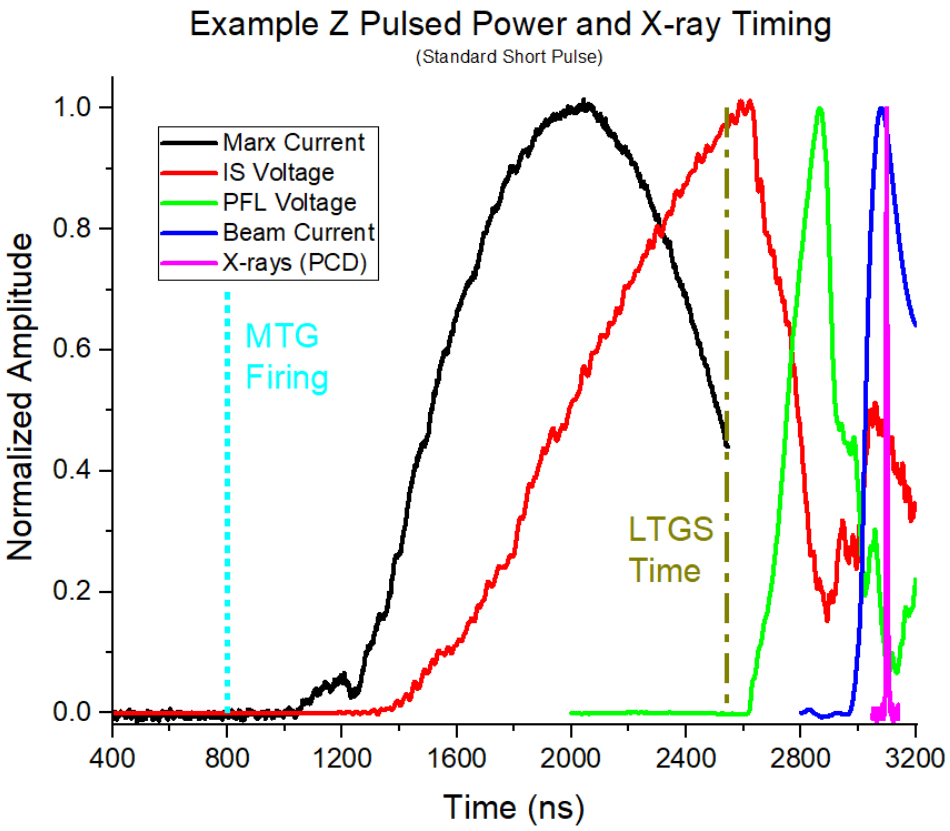

Figure 16. Example "short pulse" normalized waveform data from some of the pulsed power components and radiation pulse signals. Each waveform is recorded for much longer than shown but is truncated according to its useful portion. Only the firing times of the MTG and LTGS is shown for clarity.

B. Power and Energy Diagnostics

One of the oldest—and continuing operating diagnostics systems outside of pulsed power—are the diagnostics that measure the x-ray power and energy (P&E). We also refer to the x-ray energy as yield (we will be careful not to confuse neutron and x-ray yields in this paper). They span a very large range of sensitivities (A/W or C/J) where the Amperes or Coulombs is the measurement signal, and Watts or Joules represent the input power or energy. Figure 17 plots the response functions for the main detector technologies and the x-ray energy range over which they are applied. In selecting the detector type, the goal is to choose ones appropriate for the source intensity and spectrum. At the low end, there is a minimum signal-to-noise ratio (SNR), and at the upper end, the signal should be limited to within the linear range of the device. Best quantitative results are achieved when there is high collection efficiency of the detector for the source output spectra. As additional methods to control the signal levels and to

focus on desired parts of the x-ray spectra, x-ray filters are used and the various positions provide different fielding distances. The closest distance for a P&E detector is 30 cm or so from the load (but this is rare because of the harsh environment) and the farthest is 23 m. This is a ratio of almost 6000 times with r^{-2} scaling! Besides the detector type and distance, some detectors also allow us to control the exposed area via an aperture. The TEP (Total Energy and Power) diagnostic, described later, allows another method. Reference 33 describes more detail many of these systems as implemented at Z. There is a wide variety of x-ray filters in front of the detectors. One of the thinnest (or at least most transmissive to x-rays) is 2 µm polycarbonate. Reference 34 describes a set of five x-ray filters used to unfold an x-ray spectrum below about 3 keV using XRDs. The thickest filters may be several cm of tungsten.

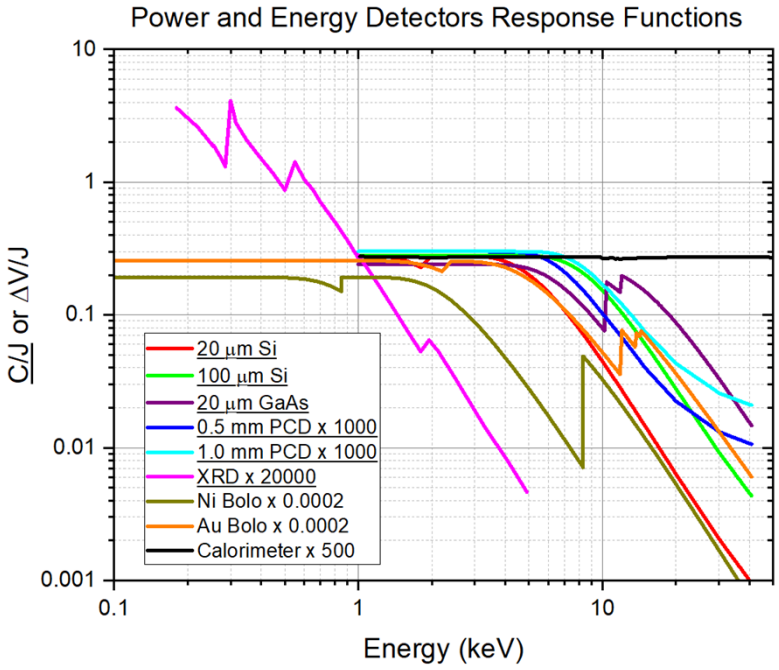

Figure 17. P&E response functions scaled to fit on the same graph. Note the different units: C/J for power detector and ΔV/J for energy detectors.

1. Locations and fielding limitations

Table 3 describes the current locations and types of "heads" where P&E detectors are fielded at Z. A head consists of a piece of hardware containing the detectors, x-ray filters, limiting apertures, and vacuum coaxial cable feedthrough ports. Most heads include permanent magnets between the detectors and filters which are designed to deflect fast electrons from the Z load or secondary particles from the filters. A photo of an XRD head is shown in Figure 18. In general, a diode detector or PCD is

technically interchangeable in terms of mounting because each use an SMA connector; in addition, either of these can be fielded in an XRD location, but not vice-versa, since an XRD uses an N-type connector. Table 3 also notes where the available infrastructure allows for bolometer fielding. The distances from the source are also given.

Table 3. P&E fielding locations showing types of detectors and distances.

Location	Number of channels	Detector Types	Distance (cm)	Note
PCD 50	6	PCDs, SIDs	1817	These are sub-locations on LOS 50-12
Bolo 50	3	Bolos	1880	
XRD 50	5	XRDs, PCDs, SIDs	2319	
TEP	2	SIDs, PCDs	2414	
LOS 170-12	6	SIDs, PCDs	249	Most common
	3	PCD or SIDs (2), Bolo (1)		Can convert Bolo to PCD/SID
LOS 210-12	5	XRDs/SIDs/PCDs (4-5), Bolo (1)	729	Can convert Bolo to PCD/SID
Axial Package	2-6	XRDs, PCDs, SIDs	421.6	Two per PODD

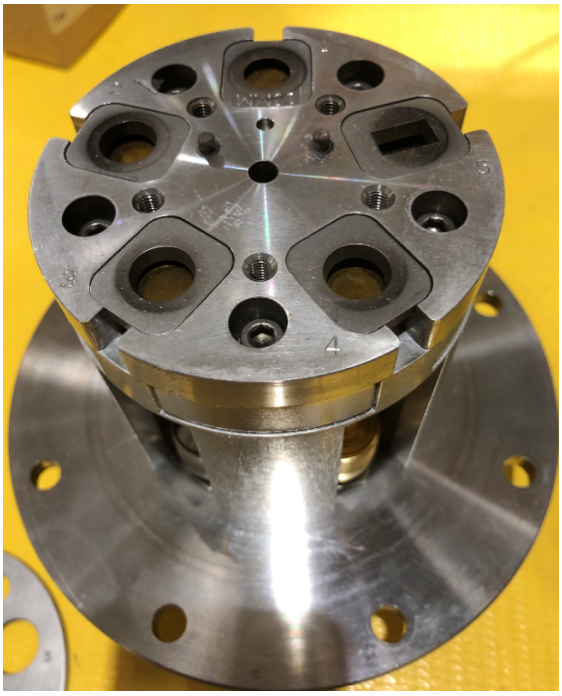

Figure 18. A photo of five-channel XRD head. On the top there are limiting apertures below which there are x-ray filters just above the detectors. In this case, PCDs or semiconductor diodes are used in place of the XRDs. There is a retainer plate on top of the detector head that is not shown with openings for the x-rays just larger than the apertures shown. One position (with the slit) holds a bolometer exclusively.

In CS, P&E systems can be fielded as well. The most common is the X-ray Calorimeter or, more simply, the "Calorimeter" which due to relative lower sensitivity must be fielded in the chamber. It is less common to field diodes in the chamber. A few specific diagnostics have been designed to field silicon diodes in chamber in highly shielded arrangements that are called DAHX[35] and WALLE. An example of a custom diode fielding arrangement with reasonable success is two or three diodes inside TIPC (section IV-D-2) in place of the pin holes and image plates. The total number of detectors (not including the Calorimeter) in CS is usually limited to twelve given the coaxial feedthrough port, cable runs, and digitizers which has been made available for this purpose.

2. P&E Detector Types and Systems

We will now briefly describe the various P&E detector types, fielding locations, typical load types, and relative advantages and disadvantages. Figure 19 gives pictures of the detectors themselves.

Figure 19. P&E detectors: A) diamond PCD, B) silicon diode C) XRD, and D) nickel bolometer.

a. PCDs

Diamond is used as a photo conducting detector (PCD) as a relatively low sensitivity but fast x-ray detector. PCDs (Figure 19d) essentially work as resistors where the bulk conductivity of the material is changed by incident radiation. Most, if not all, Z PCDs are CVD, not natural material. Reference 36 is an excellent review article describing the theory and application of diamond radiation detectors. The sensitivity (A/W) of a PCD is given by:

$$S = \frac{q \cdot \mu \cdot \tau \cdot V}{g \cdot w^2} \quad (1)$$

where q is the electron charge, μ is the electron mobility, τ is the mean carrier lifetime, V is the applied bias (typically 100 V for PCDs at Z), g is the energy required to generate an electron hole pair (EHP) in diamond, and w is the width of the diamond between the ohmic contacts (1 mm for Z PCDs). In particular, the low carrier lifetime (on the order of hundreds of picoseconds) is what gives the PCD its fast time response. Some of these parameters vary from sample to sample, so each device must be individually characterized or calibrated. Some Z PCDs have been calibrated over ten years ago using a gas puff source at Saturn[37] using bolometers as a reference, but that capability is no longer available. We are currently researching other methods and sources. Some recent efforts have attempted to use higher energy pulsed power bremsstrahlung sources (1-3 MeV) and then relating the absorbed dose to TLDs. The long-term stability of a PCD calibration and conditions required to maintain it are current subjects of

study. It should be noted that PCDs behave somewhat non-linearly (native signal is not necessarily proportional to the input power) because they are effectively resistors as part of a larger circuit and, as can be seen from Eq. 1, the sensitivity is bias dependent, and thus the signal affects the bias. However, this can be corrected for in a straightforward manner[38,39].

Conversion of a corrected PCD signal to x-ray power can be done via the following formula:

$$P = \frac{I}{A \cdot s} 4 \cdot \pi \cdot d^2 \quad (2)$$

where I is the measured current (measured voltage divided by 50 Ω scope impedance), A is the exposed detector area, s is the sensitivity (remember this is energy-dependent), and d is the fielding distance. This equation assumes the source is Lambertian and does not self-attenuate the spectrum. This formula also applies to the analysis of semiconductor diode (next section) signals.

PCDs are robust against minor debris (dust) and shock. They can be cleaned with an ultrasonic cleaner. PCDs are not often in the vacuum chamber since they are one of the more expensive (per device) detectors especially considering the difficulty of calibration. Another version of a PCD is fielded in the chamber and is known as the MCVD (shown in Figure 4). It employs more significant debris shielding and filtering and measures hard x-rays from the target.

b. Semiconductor Diodes

Silicon and gallium-arsenide (GaAs) PIN diodes are frequently used at Z as a high sensitivity x-ray power detector. As well-studied semiconductor materials, silicon and GaAs have well-known values for the energy required to produce an EHP, 3.62 eV and 4.2 eV, respectively. As long as the diode junction which spans the intrinsic region of the diode is fully depleted, the signal is proportional to the absorbed x-ray power and is considered intrinsically calibrated to first order though other effects such as the junction capacitance and carrier drift time affect its time response. Observations have indicated that this linear range extends up to, and sometimes beyond, approximately 10% of the bias level applied to the diode. Beyond that the time response may appear to slow down, but the time-integrated signal is observed to be proportional to the x-ray yield[40] over a much larger range.

One source of uncertainty with some diodes is that the active area and depth may not be precisely known. An example is the AXUVHS11 silicon diode[41] which has a quoted active area diameter of 0.6 mm. Local measurements have detected an area which may be sensitive to x-rays up to 0.81 mm in diameter. In addition, charge diffusion from the depth of the material may contribute other charge at different time scales. Questions like these and the desire to have greater collection efficiency at 10-20 keV have spurred Sandia to develop their own GaAs diodes[42] with precisely known geometries. In addition, we are currently designing new silicon diodes with a variety of areas and structure such as using classic epi wafer or SOI (silicon on insulator) wafers where such properties as the relative speed, how well defined the active volume is, and give a variety of sensitivity ranges applicable to different levels of x-ray flux. For instance, two diodes with the same absolute collection efficiency but different device areas could be used at different distances from the Z target and would return the same x-ray yield when appropriately scaled.

Diodes are more susceptible to damage and even minor debris which can produce a nonremovable film on the device surface. In the case of GaAs diodes, this film appears to introduce a parallel current leakage path which may be too large to bias the diode. The wire bonds can also be destroyed from shock, larger debris, or general handing. Per device cost is low, so these diodes can be used almost anywhere at Z.

c. TEP

The Total Energy and Power (TEP) diagnostic[43] is not a detector type but a system configuration that can use either semiconductor diodes or PCDs. It is designed to return an unfiltered pulse shape of a cold x-ray source. The TEP reduces the x-ray flux by using an array of pin holes to produce a large set of overlapping images at the detector location. The pin holes are 10 µm diameter laser drilled into 50 µm tantalum in a 38 x 38 array with a 361 µm pitch. The TEP has a pair of detector/pin hole sets. As configured as shown in Figure 20, the flux is reduced by about a factor of 1800. To produce an absolute power measurement, analysis involves time-integrating the TEP signal and scaling it according to an unfiltered bolometer.

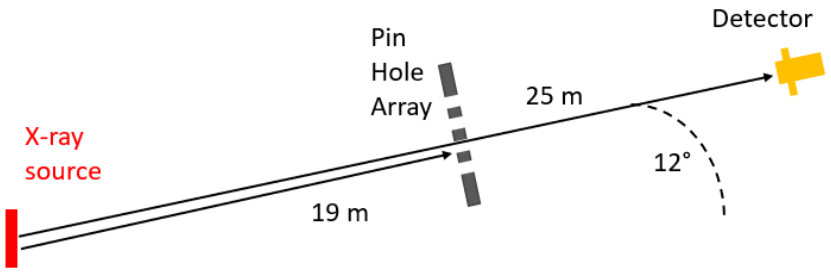

Figure 20. Operational principle of the total energy and power (TEP) diagnostic.

Because of the fielding distance, the TEP is robust to debris though the pin holes need to be inspected and cleaned regularly, even after a few shots when used. The TEP used to utilize a fast closure valve upstream of the pin hole plates, but this has since been discontinued since almost no larger-scale debris has been found to travel up the 12° LOS. Alignment may be affected over time and may require periodic checks. EMI is occasionally an issue since signals are often below 1 V.

d. X-Ray Diodes (XRDs)

Figure 19b shows an XRD[44] which has been used at Z for several decades to measure soft x-rays below around 3 keV. The signal is generated by electrons emitted by the carbon photocathode by incident x-rays passing through a nickel wire mesh that acts as the anode. XRDs also require individual calibrations due to small variations in surface conditions. Most of the electron spectrum exiting the photocathode are not primary photoelectrons generated by the photoelectric effect but secondaries or down-scattered electrons with the result that the majority of the measured electrons are below a few 10's of eV. The XRD sensitivity is thus not "flat" (see example profile in Figure 17) and must be individually characterized since there is a strong sensitivity of the photocathode condition and contaminants, principally hydrocarbons. These contaminants on a carbon photocathode are expected to have less of an effect than a similar amount on gold which would have a higher intrinsic (not affected by contaminants)

quantum efficiency. However, it has been observed that the Z XRDs can be used on multiple shots and are even found to be stable over several years but not necessarily consistently (shot history and method of fielding matter for individual devices). XRD calibrations are performed at the SSRL beamline 16-2[45] from 40 eV to 2.5 keV. The XRD are biased up to 1000 V to maximize the dynamic range, but the signal is not voltage dependent well below the space-charge limit. An aperture limits the beam to 5 mm diameter. The space-charge limited current including effects of the mesh is about 4 A, so the goal is to limit the signal to well below that level. Unlike PCDs and semiconductor diodes which can be operated in normal atmosphere or vacuum, XRDs must be operated in vacuum because of the low mean free path length for the photoelectrons, even in gases.

e. Fast Resistive Bolometers

For yield measurements of "cold" x-rays (< 10 keV), thin foil bolometers[46] of either nickel or gold are used. The yield is inferred from a measurement of the time-dependent resistivity of a 1 µm thick metal foil that is heated by the absorbed x-ray flux. The foil has been coated onto a glass substrate[46]. A few microseconds-wide current pulse of about 40 Amperes is passed through the bolometer, and a change in voltage is measured. Like the calorimeter described next, the bolometer natively *integrates* the x-ray power which is why the sensitivity data in Figure 17 is expressed in $\Delta V/J$. *X*-ray power can be inferred by differentiating this signal which can then be compared to other power diagnostics though this process magnifies noise significantly. Conversely, the time-integral of the other power diagnostics can be scaled to the bolometer yield. The measured signal, in ΔV, is proportional to the ambient resistance which is one reason the foil is thin (overall resistance around 0.5 Ω). The limit of the temperature rise is within a few degrees to avoid nonlinear effects.

The bolometers are operated in vacuum, but this has more to do with avoiding soft x-ray attenuation than operational impacts of the bolometer itself. The bolometers are typically not fielded in the chamber to avoid damage to the foil. There is a very limited number of operational bolometers at Z. The current supply of bolometers was built using the methods and equipment described in reference 46. That capability is no longer extant; therefore, we are currently in the process of evaluating other sources and processes to replenish the inventory.

f. In-chamber Calorimeter

The "warm" and "cold" x-ray yields are measured using basic calorimetry techniques applied with a 1.1 cm diameter, 500 µm tantalum disk in a configuration which is simply referred to as the "calorimeter" since it is the only calorimeter now used at Z. Type E thermocouples (about 61 µV/°C) are used to measure the temperature of the tantalum. A diagram of the calorimeter is shown in Figure 21. The calorimeter is considered a time-integrated measurement even though the thermocouple voltage is measured with an oscilloscope. Thermal equilibration in the tantalum element is on the order of 10 milliseconds. Thermal decay is slow post-shot even when the Z chamber vacuum is on the order of a mTorr, so the temperature is recorded for several seconds after the shot which allows us to verify that the calorimeter operated normally. Bullets (Figure 12) hitting the tantalum or the thermocouple wire at any point effectively destroy the measurement. Gas Puff targets produce higher amounts of hot gas which could enter the calorimeter producing extra heating. Where view of the target allows, two calorimeters are fielded with two different filter thicknesses. The variable filters allow different views or emphasis of the x-ray spectrum to test or verify the analysis method. The fielding distance within the chamber is chosen according to the expected yield and varies between 36 cm to 110 cm though the closest positions suffer the greatest risk from debris.

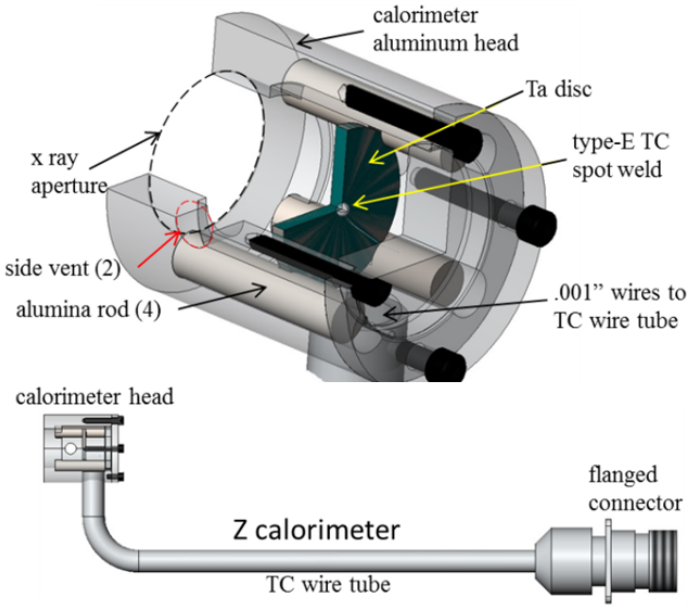

Figure 21. Z calorimeter internal and external construction.

C. X-ray spectroscopy

Wavelength dispersive x-ray diagnostics use Bragg diffraction using crystals such as quartz, Ge, and others to disperse the various x-ray energy components across an imaging detector in one direction. One-dimensional imaging using slits is applied with these systems in the transverse direction to the energy dispersion. Figure 22 shows the general principle of operation of the Z spectrometers with the primary components. All Z spectrometers utilize bent (as opposed to flat) crystals of different types in various defined geometries to provide varies ranges of the dispersed x-rays. The energy resolution ($E/\Delta E$) also varies according to the instrument. Depending on the specific diagnostic, the imaging detectors consist of x-ray film (section IV-H-2), image plates (section IV-H-1), or can be time gated via MCPs (Section IV-H-4) or UXI (Section IV-H-3). There are four general crystal diffraction geometries used in the Z spectrometers illustrated in Figure 23. Along the plane of the page is the energy dispersion direction. One dimensional imaging occurs in the other direction. The first type is referred to as the "convex" crystal geometry such as used on the TIXTL (Figure 22) where the crystal is bent along a cylindrically curved surface (one inch to nine inch in bend radii), and the crystal planes are parallel to the surface. Another version is the elliptical geometry where the crystal is bent along a portion of the inside surface of an ellipse. This spectrometer is set up so that the x-ray source (z pinch) is at one focus of the ellipse with the result that the x-rays are focused on the other focus. A collimator or filter is often placed at the latter focus before the rays diverge towards the detector. The TREX[47] instrument uses this configuration. The third crystal spectrometer type uses the "Cauchois" geometry[48] where the crystal is

bent in a circular shape, but the x-rays instead pass through the crystal while being diffracted. Here, the crystal planes are normal to the surface. This is also known as Lau diffraction. The CRITR[49] uses this geometry. The energy dispersion (energy versus space) has a simple analytic form[48] unlike some of other spectrometers with which one uses ray tracing, calibrations, or fitting to known x-ray lines to map the dispersion. A fourth spectrometer type uses a concave *spherical* geometry which spatially focuses in the sagittal direction and disperses the energies in the meridional plane as shown in Figure 24[50]. The x-ray scattering spherical spectrometer (XRS3) and multi-optic novel spherical crystal spectrometer (MONSSTR) instruments uses this fourth type. It should be noted that all other spectrometer geometries use slits for imaging. Most spectrometers can be rotated so that the imaging direction of the target is either in the radial direction or axial direction (RR or AR for "radially resolving" or "axially resolving", respectively).

Figure 25 through Figure 29 and Table 4 show the spectrometer instruments and give key operational characteristics. Figure 30 gives an example CRITR-AR spectrum. The "AR" refers to a "axially resolving" CRITR configuration; there is a "RR" ("radially resolving") configuration where CRITR is flipped 90° with a different support base.

The external LOS spectrometers, TIXTLs, TREX, and those in the Axial Package, generally fare well in the Z environment in that debris is usually low risk, and x-ray backgrounds are minimal. The main trade-off is in signal strength given the distances from the source. For instance, the TIXTL detectir is 4.5 meters away and the CCP crystal is 4.1 meters away. Conversely, in-chamber spectrometers like CRITR are much closer at either 0.45 meters or 0.72 meters (axially resolving configuration). The shielded boxes still reduce x-ray backgrounds so that, overall, SNR is much higher for spectrometer located in the CS. Note that all spectrometers are still part of the Z vacuum envelope, in part to avoid x-ray attenuation in normal atmospheric pressure.

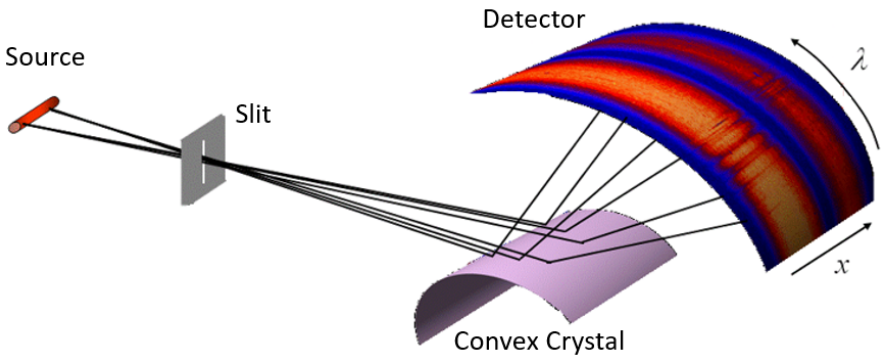

Figure 22. Principle of operation of the imaging spectrometers using slits where *x* is the imaging direction along the detector and *λ* is the wavelength-dispersion direction. The TIXTL and CCP use the convex crystal geometry as shown.

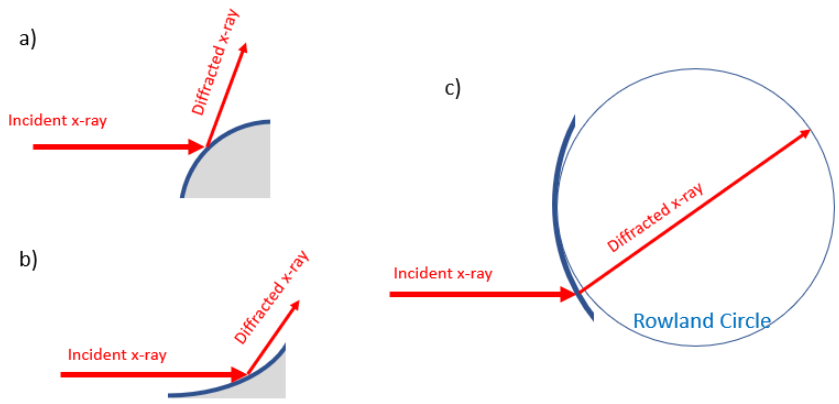

Figure 23. Crystal diffraction geometries used on the Z x-ray spectrometers. A) Convex. B) Elliptical. C) Cauchois.

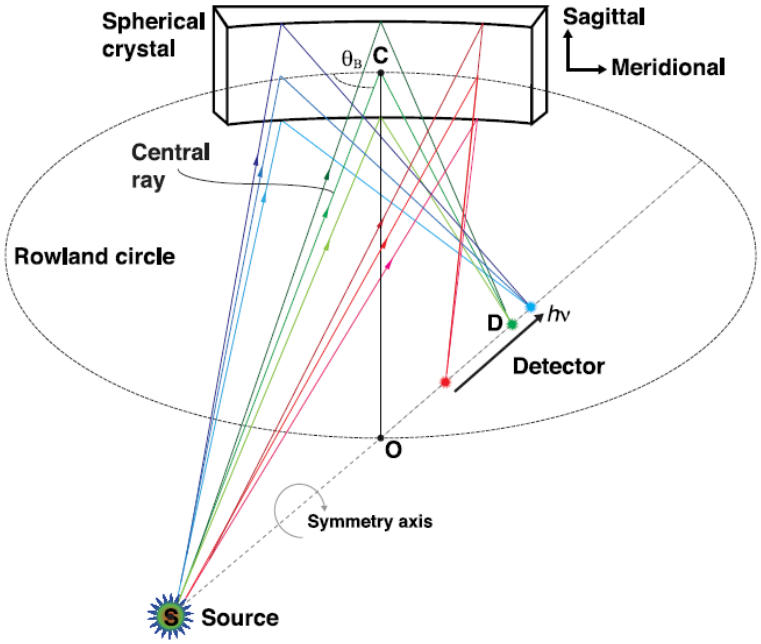

Figure 24. Focusing spectrometer geometry used by the XRS3 and MONSSTR diagnostic. Wavelength dispersion occurs along the meridional direction and 1D imaging occurs along the sagittal direction. Reproduced from E. C. Harding, *et al.*, "Analysis

and implementation of a space resolving spherical crystal spectrometer for x-ray Thomson scattering experiments", Review of Scientific Instruments 86, 043504 (2015), with permission from AIP Publishing.

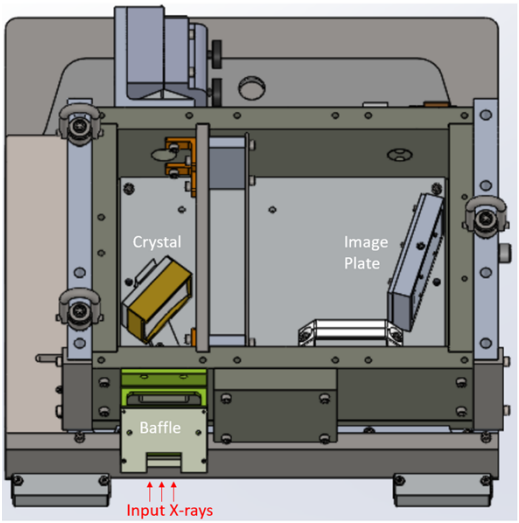

Figure 25. XRS3 internal construction.

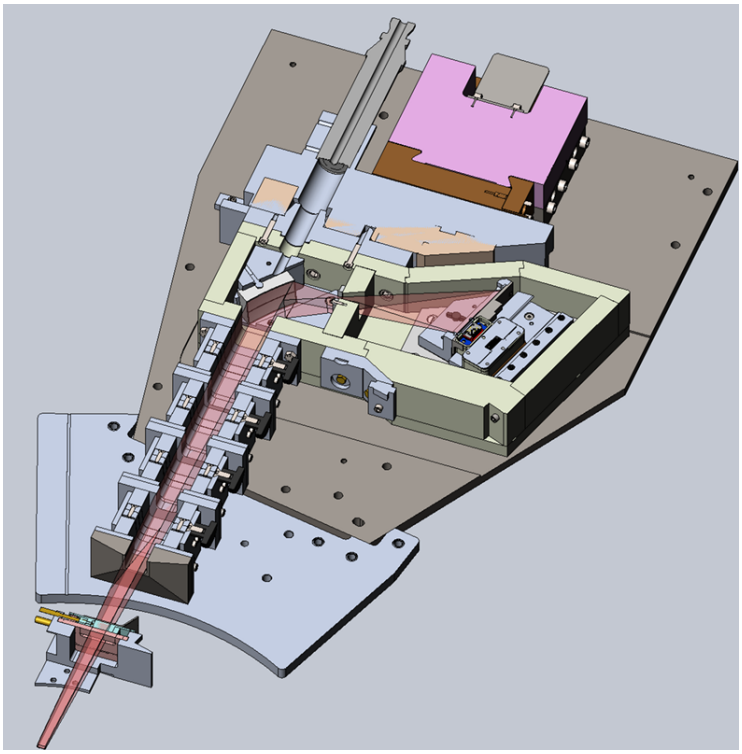

Figure 26. MONSSTR diagnostic which is basically a time-resolved version of XRS3. The beam path is shown in pink. This device can be flipped to provide radial imaging rather than axial. The external parts of the UXI housings are visible as the teal boxes.

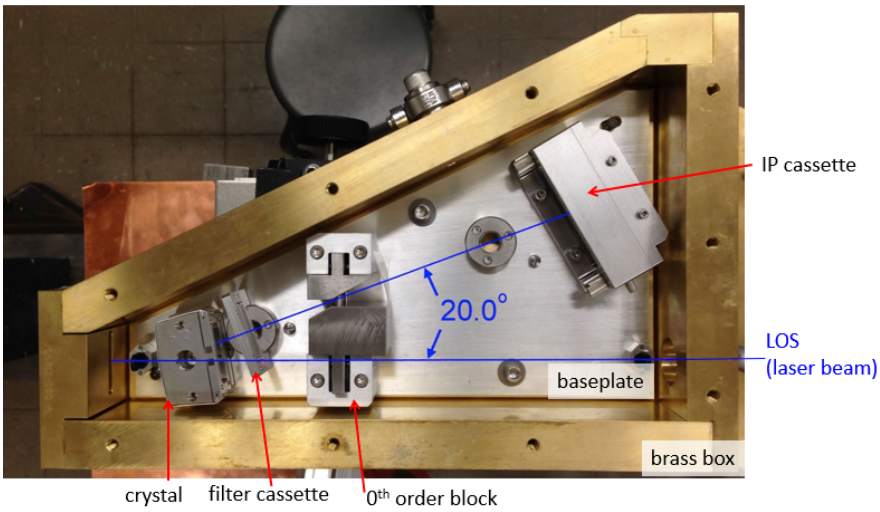

Figure 27. CRITR(X) internal components. The older (standard) version of CRITR fits in the same shielded box and has the same overall geometry but there are different versions of the crystal mount and detector cassette. The filter cassette and zero-order block are optional components.

Table 4. List of Z x-ray spectrometers and main parameters. There are different crystal types available for most spectrometers where range is more narrow than listed.

Name:	TIXTL	CRITR	TREX	CCP	XRS3	MONSSTR	TiGHER[51]
Energy range (keV):	< 1 keV – 20 keV	8-20, 17-60, 30-100	4 keV window from 1-13 keV	< 1 keV – 20 keV	3 keV window from 1-15 keV	3 keV window from 1-15 keV	8-20
Crystal configuration:	Convex	Cauchois	Elliptical	Convex	Spherical	Spherical	Cauchois
Location:	LOS 130-12	Chamber	LOS 330-12	Axial Package	Chamber	Chamber	Chamber
Spatial imaging direction (Axial / Radial / Either)	Either	Either	Either	N/A	Either	Either	Axial
Maximum Number of systems	2	2	2	6	1	1	1
Magnification:	1	0.5 or 1	0.3	1	0.3	0.3	0.5
Detectors:	IP or Film	IP	MCP, IP, or Film	UXI, IP, or Film	IP	UXI	MCP

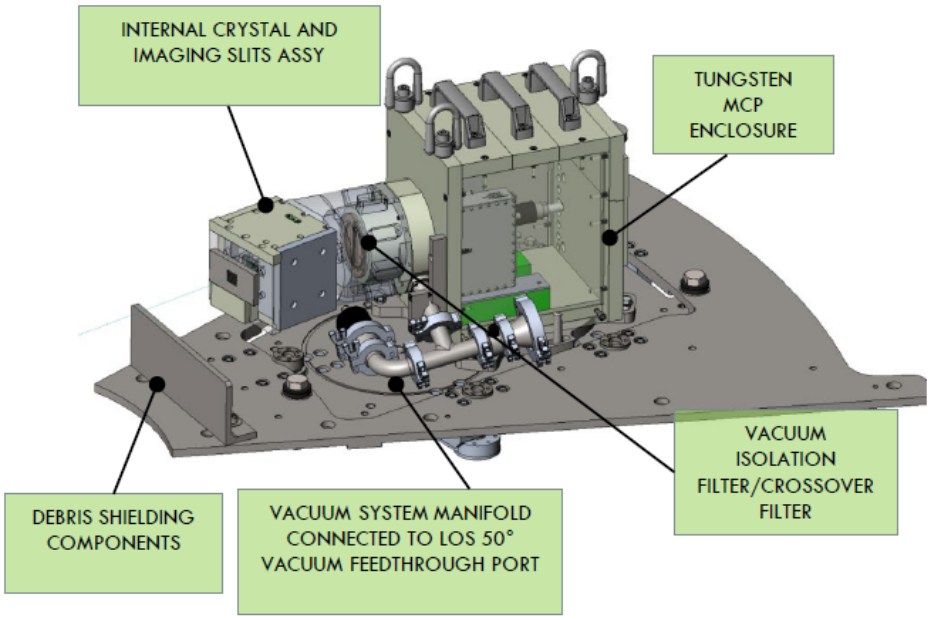

Figure 28. TiGHER spectrometer shown installed on a MITL deck plate.

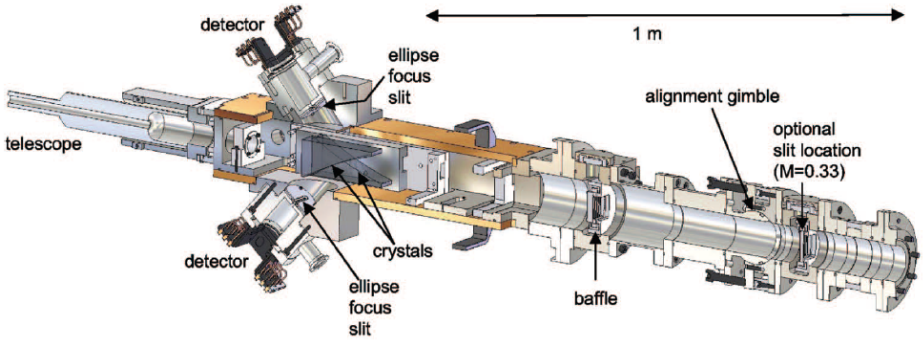

Figure 29. TREX internal components. The x-rays are incident from the right.

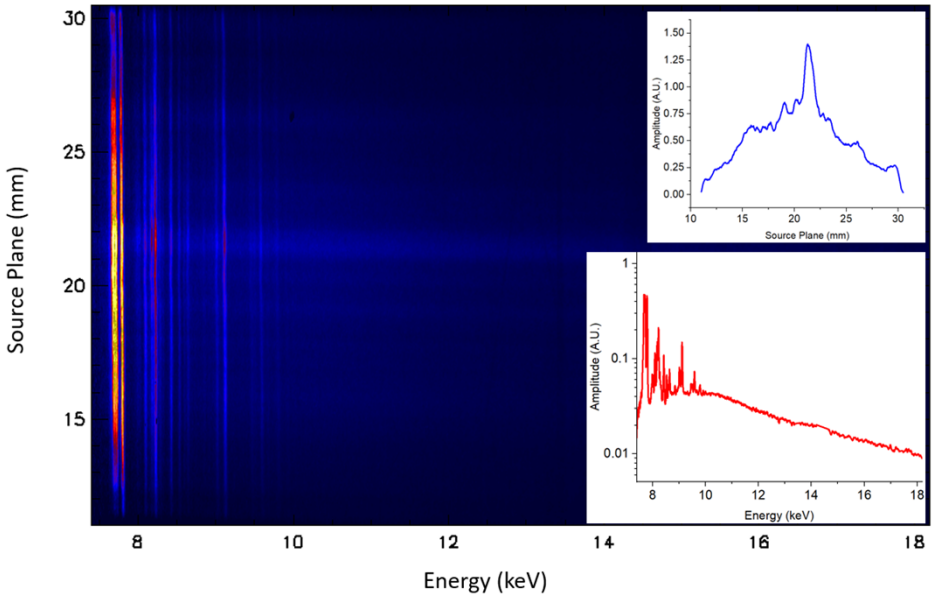

Figure 30. Example CRITR data of a Z stainless steel wire array shot. The inset plots are a lineout across the imaging direction (top) and energy resolving direction (bottom).

D. X-ray Imaging

A wide range of imaging diagnostics view the Z target with various options for sensitivity, resolution, and spectral sensitivity. It is one of the most requested types of diagnostics for MIF and RS targets (x-ray spectroscopy is comparable). There two general classes of two-dimensional x-ray imaging of the Z pinch source, pin hole imaging and crystal imaging. In the latter case, crystal imaging can be split into a few sub-categories, one of which is "backlighting", and another is "self-emission" imaging. Both of these use bent crystals to diffract a single x-ray energy but vary in whether these x-rays originate in the Z target or an external source (in this case, a laser-driven plasma source). A Wolter-type imager[52] is also available at Z which can also be classed as a type of crystal imager. We will discuss these techniques and the main systems separately.

Pinhole imaging applies the classic method[53] using a set of small apertures in a thick substrate where x-rays from the target project through the pin holes onto the detector in a tight enclosure often with some x-ray filter somewhere in the path. The advantages of pinhole imaging are its relative simplicity and large operating space in terms of design options. Systems are fielded inside or outside of the chamber—though always in vacuum—with a wide variety of magnifications and pin hole sizes. It is straightforward to couple detectors of various types including time resolved. Pinhole cameras are

robust to debris since the pin holes may absorb the incident material if necessary. In terms of energy acceptance, pinhole imaging is generally broadband though the x-ray passband can be limited using filters or using multilayer mirrors[54] (see MLM in Section IV-D-1) to pass only a single energy. Table 5 lists the Z pinhole imagers and their key parameters.

As a general capability, crystal imaging uses bent crystal x-ray diffraction to produce images working like that of a spherical mirror. Using Bragg diffraction, only a single wavelength of x-rays is reflected which is very desirable in many applications. Crystal imagers, in general, have a much higher spatial resolution than pinhole imaging for the same detector throughput (effective solid angle) because the crystal also focuses the x-rays. The detector is removed from a direct view of the target and other load debris, so the main "consumable" may be (and often is) the crystal. The primary risk is x-ray backgrounds finding its way into the detector box. At Z, crystal imagers are only fielded in the chamber since precise focusing conditions must be met tied to the Rowland circle[55] which is on the order of tens of centimeters in diameter. We apply crystal imaging in backlighting and self-emission imaging as described in later sections.

Table 5. List of pinhole imagers at Z.

	MLM	MIP	TIPC	TRICXI	APE / SOPI	FOA PHC
Location	LOS 170-12 boat	Axial Package	CS	CS	CS	Vacuum FOA
Magnification(s)	0.5	1	0.38	3, 1.0	10	1
Sensor	MCP	MCP	IP	MCP	IP	UXI
Pin hole type	MLM*	MLM	MLM or 250 µm	MLM	10 µm	300 µm
Approximate FOV (mm x mm)	> 20 x 20	8 x 8	> 20 x 20	1 x 12, 3 x 12		10 x 10
Other details	3 total channels with 2 mirrored (277 eV or 528 eV)	2 mirrored channels (277 eV or 528 eV)	five filtered channels	Mag 1 has three pin holes per MCP frame	Typically use pin hole arrays to increase alignment margin; may include filter sets	7.5° from normal

1. MLM

The Multilayer Mirror (MLM) camera[56,57] is a time-resolved pinhole camera system with three channels. Each channel uses an array of eight pin holes coupled to each frame of a Gen I MCP (see Section IV-H-4)

which allows them to be independently timed. There is a “right” and “left” channel which uses a flat multilayer mirror to reflect only either 277 eV or 528 eV source x-rays. The “center” channel is broad band. The MLM is located at LOS170-12 residing mostly in the boat (MCP cameras slightly beyond it). A diagram of the MLM is shown in Figure 31. The imaging magnification is 0.5. Before the shot during the alignment process, the entire MLM instrument is tilted in two directions with the target in view from the back of the instrument (upstream of the MCPs) with the pin holes retracted. Before the shot, the MLM is opened to the Z vacuum chamber. Some small-scale debris (soot) travels up the instrument but are generally stopped at baffles upstream and downstream of the pin holes. There are also thin metal filters located near the MCPs which protect the detectors. The gating options will be described in Section IV-H-4 with the MCPs. The MLM has an independent vacuum system because the MCPs require extended pump out prior to use (at least several hours).

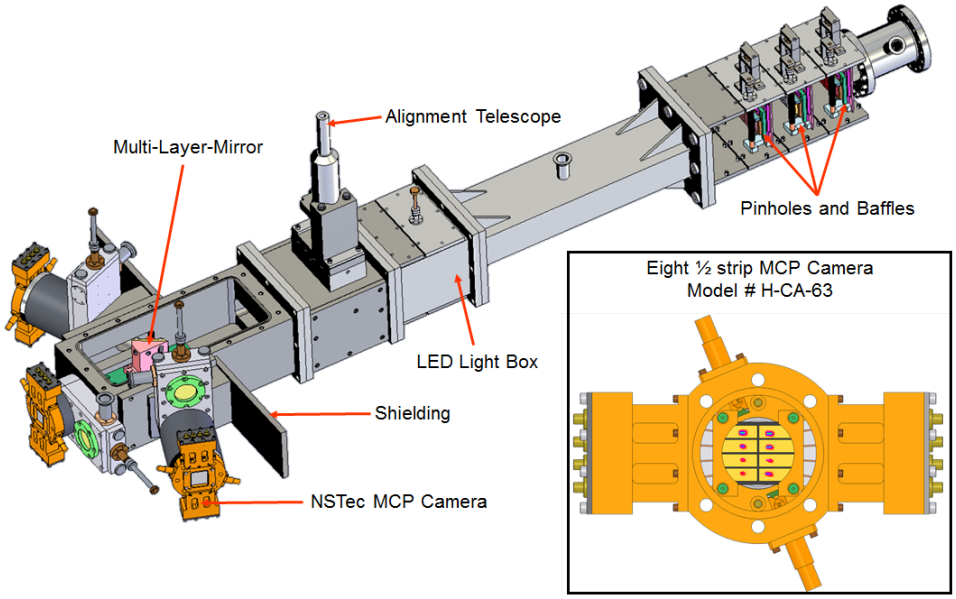

Figure 31. The MLM system and an MCP camera.

At this time, we will describe the geometry of the pin holes used in MLM which are also used on some other pinhole cameras such as TIPC and TRICXI. Various aperture sizes are available with a constant outer diameter. Figure 32 gives the geometry and sizes. The substrate is thin and may be partially transmissive to certain x-rays of interest.

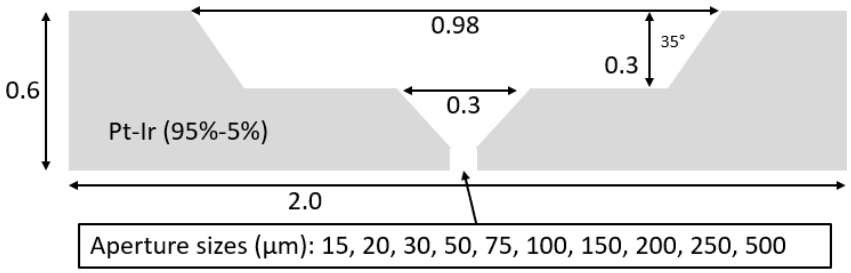

Figure 32. Diagram of "MLM" style pin holes. Dimensions are in mm. These are installed in thick (often tungsten) metal substrates of various geometries. The openings of these substrates are usually about 1 mm diameter.

2. TIPC

The Time-integrated pinhole Camera (TIPC)[58] is a general survey camera located in the Z vacuum chamber. The pin holes and image plate detectors are contained in a single tungsten-walled box. The walls of the box are one inch thick (the default value for in-chamber shielded enclosures). There are five pin holes (for five total images) located at 26 inches from the Z load, and the camera magnification is 0.385. There are three styles of pin holes: MLM-style using any of the available sizes, a set of 250 µm straight-cut pin holes in a single 1.0 cm block, and a similar thick pin hole set where the pin holes are tapered. The thick pin hole styles are more appropriate when viewing higher x-ray energy sources at the expense of much lower resolution. Each pin hole can be individually filtered; one application of doing so is to design Ross-pair filter sets on pairs of images from which approximately monochromatic images can be produced. TIPC is typically very robust to x-ray backgrounds and debris. There is a series of chevron-shaped baffles in front of the box along with a typical 1.5 mm of polyimide to block debris, and the pin holes and filters view the load through a narrow aperture.

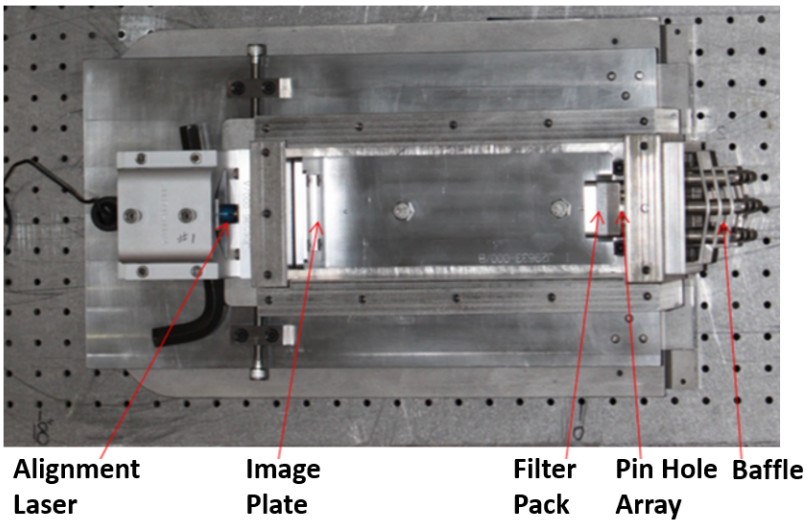

Figure 33. TIPC photo (clean, before any shots) and primary components. For use at Z, there is a top lid and 0.5 mm Kapton sheets are installed in the baffles.

3. TRICXI

The Time-Resolved In-chamber x-ray imager (TRICXI)[59] is a pinhole camera designed for higher resolutions and greater sensitivity than the MLM camera. It uses a single Gen II MCP. It was designed specifically to view MagLIF targets but has a few configurations to allow for different FOVs and resolutions. Magnifications of 1.0 and 3.0 are available which are determined by moving the pin hole position while keeping the detector location fixed at 88 cm. MLM-style pin holes are used. Mag 1.0 allows for three pin holes (and sizes) per frame. Because the MCP camera is in the chamber and requires lower vacuum pressures ($<1x10^{-5}$ Torr) for longer time frame than the Z chamber is typically pumped and to prevent shot debris from impacting the MCP, there is an independent vacuum system applied to the portions of TRICXI. The turbomolecular pump is located in the LOS 50 boat. It took several iterations of shielding designs to produce effective time-resolved imaging of the source. Hard x-ray backgrounds, which appear to originate from extended sources near the Z pinch, produced time-integrated images stronger than the targeted time-resolved soft x-ray images. One major change to the magnification = 3 configuration was using a 0.5-inch-thick tungsten plate holding the pin holes. Attention was paid to maximize the pump conductance near the MCP chamber so that the vacuum pressure near the MCP was no worse than a factor of two higher than the nearest monitored position at a vacuum gauge mounted to the side of the TRICXI box. Other threats include hard debris which damages the snout and bullets which may strike the vacuum line that results in rapid venting of the MCP.

4. APE and SOPI

Two other pinhole imaging systems are available at Z. These operate at a magnification of 10 and utilize an array of pin holes which can be customized according to the experiment. One system called APE (Axial Pinhole Imager, Figure 34) sits above the target, and the other, SOPI (Side-On Pinhole Imager, Figure 35) sits on the MITL deck. An object plane resolution of approximately 10 µm is predicted using

pin holes of the same size (high magnification pin hole imager resolutions are usually about the same size as the pin hole). High resolution allows microstructure and non-uniform hot plasmas to be measured on MIF sources at the expense of reduced FOV and more difficulty in alignment. The optional multiple pin hole capability mitigates the later weakness so that it is more likely to record one or more pin hole images per image plate. APE has three data paths onto image plates which can include custom x-ray filters; SOPI has two data paths. SOPI is easier to align than APE with a chain driven "elevator" and pivoting system. SOPI also has an extensive baffle system for debris and x-ray shielding. APE is more difficult to align since it relies on more manual placement and is more susceptible to bullets traveling axially.

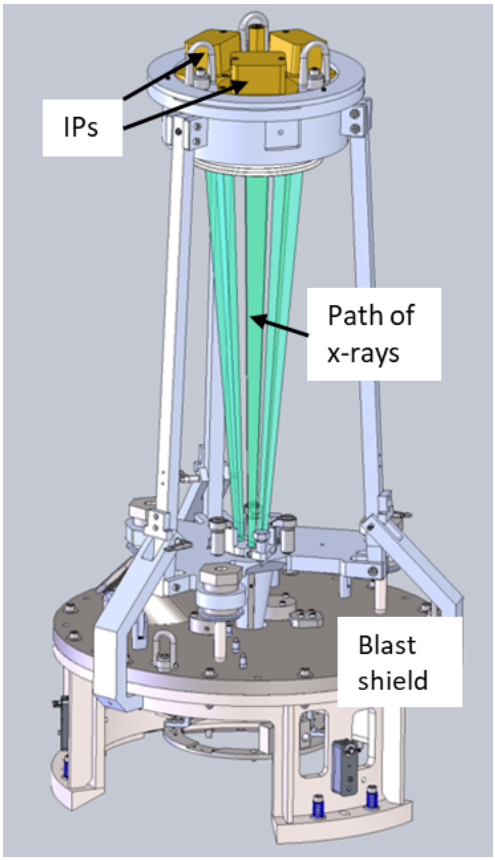

Figure 34. APE model shown on top of a blast shield. The green cones on the APE show the optical path that converge in the direction of the Z target. There are three separate data paths corresponding to a pin hole array and detector pack which can be independently filtered.

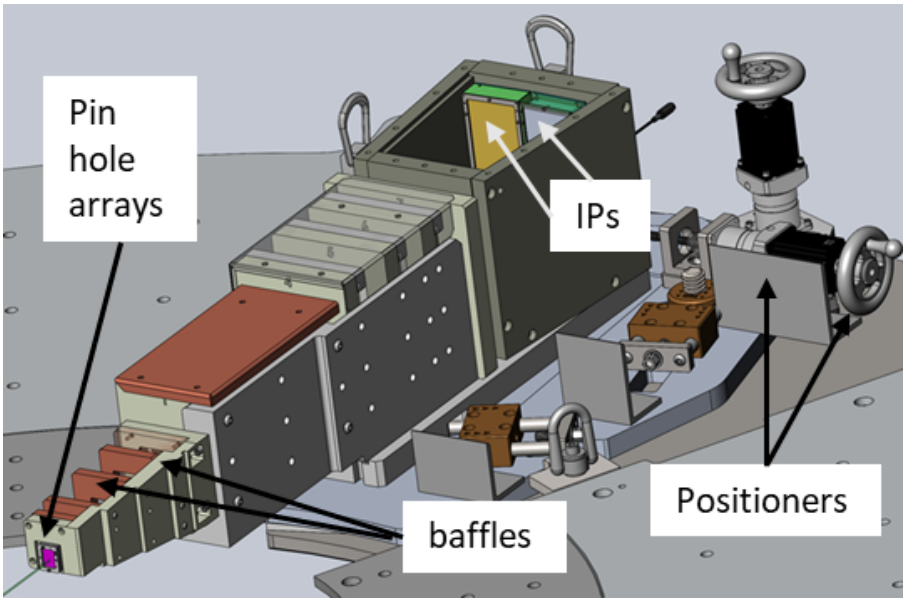

Figure 35. SOPI as installed in the CS MITL deck. There is a top lid to the back of SOPI not shown in order to show the two image plate cassettes. There are additional baffles not shown farther upstream. The front baffles fit within an opening the blast shield (not shown).

5. Radiography using X-ray backlighting

Point projection radiography was pursued early-on at Z[60], but better results[61,62] have been achieved using monochromatic imaging techniques paired with a thermal x-ray source generated with the Beamlet laser[63]. This laser system (an early NIF laser prototype) allows two semi-independently timed (up to 20ns separation) laser pulses onto two separate foils which generates He_α x-rays. Two angularly off set beams are used to produce two separate images with a small (6°) offset in the view. The choice of target material determines the energy of x-rays produced. To date, targets made of Si (1.86keV), Mn (6.151keV) and Co (7.2 keV) have been used at Z. These x-ray sources are located near the Rowland circle of spherically bent crystals. The Z target is then backlit by these x-ray sources with the resulting image obeying the thin lens equation:

$$\frac{1}{p}+\frac{1}{q}=\frac{1}{f}=\frac{2}{R\sin\theta} \quad (3)$$

with p and q being the conjugate distances, and R is the bending radius of the crystal. The geometry is illustrated in Figure 36. The size of the crystal is chosen to provide a field-of-view of the Z target of 10 mm wide and 4 mm tall. The magnification is six. The Bragg angle and crystal type and orientation are

chosen to diffract the specific He-alpha line of the source. The two crystals are offset 3° above and below the midplane vertically respectively.

The standard laser pulse used to produce x-rays for backlighting is a 1 ns FWHM Gaussian with ~1kJ of energy preceded by a small (<100 J) pre-pulse which boosts x-ray conversion efficiency of the main pulse[64]. The two angularly offset beams are created by splitting a portion of a single beam and delaying it relative to the other portion along with its angular offset. The 2nd beam can be delayed up to 20 ns from the primary beam.

Because Z is a significant producer of x-rays, the detector needs to be shielded from direct exposure to the load. This means a thick Tungsten housing for the detector as well an aperture at the focal point of the imaged x-rays. The Bragg reflecting crystal only reflects a small spectral band of x-rays preventing most of the x-rays produced by Z from impinging on the detector. The large tungsten housing results in the backlighter diagnostic taking up a fair bit of space near the load, limiting space for other such diagnostics. Backlighter images have historically most often been taken of wire arrays and imploding cylindrical loads[65,66].

Despite all the efforts to minimize the x-rays produced by the Z experiment that arrive at the detector, many experiments still produce significant background, either as a semi-uniform haze on the detector or as an intense burst near the center of the load. These background emissions are often separated in time from the laser produced x-rays, so time gated UXI based detectors have been used to improve signal to noise. These detectors have been successfully fielded on a number of shots over the last few years but have their own limitations. The size of the UXI sensor (1" x 0.5") is significantly smaller than the Image plate usually used (2.531" x 1.375"), making it poorly matched to the experimental dimensions for most experiments. In addition, the Z environment is harsh for electronics, but mitigations as described in Section IV-H-3 have been put in place.

An alternate configuration of the backlighter diagnostic allows imaging of x-ray self-emission from the target instead of the laser produced x-rays. This configuration utilizes the same type of bent crystals and detector as the backlighter configuration, but a different x-ray source.

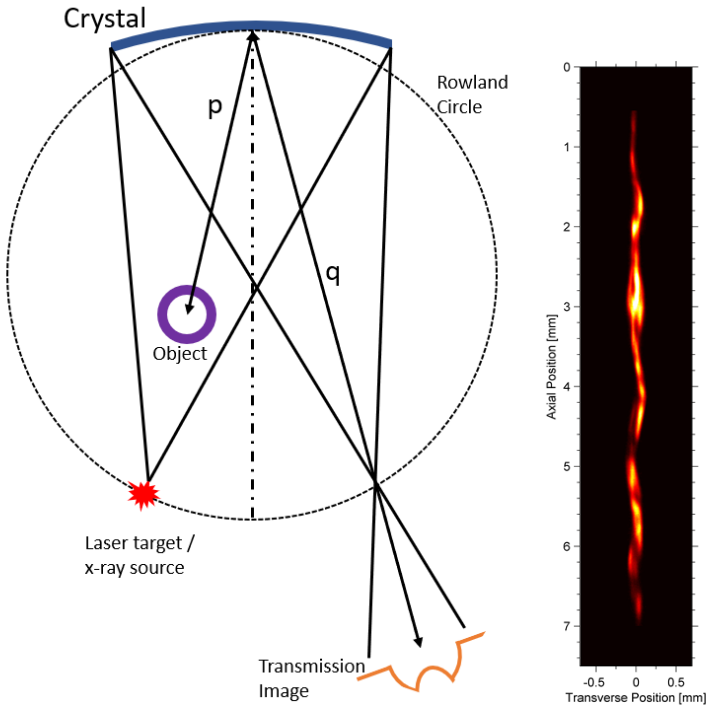

Figure 36. Left: x-ray backlighting geometry if the source is located on the Rowland circle. It is possible to move the source off (usually inside) the Rowland circle which moves the focus position. Self-emission imaging works similarly only that the spherical focusing occurs at the "object" in the meridional (in the plane of the page) and sagittal (not shown) directions and there is no laser-target. An example of self-emission imaging of a MagLIF target is shown at the right.

6. Dynamic x-ray diffraction measurements

The ZBL backlighter may be applied for the x-ray diffraction experiments on DMP loads[67]. The crystal structure of compressed material changes over time including elastic changes of the lattice plane spacing, phase transitions, and the density of crystal defects. The geometry is similar to that of Figure 36 except the Z load and x-ray diffraction sample is located on the Rowland circle but the ZBL source is located outside of the circle. A specially designed shielded box for the image plate is known as SCDI (spherical crystal diffraction imager) to shield from the high energy x-ray environment that is known to exist even on DMP loads. A narrow slit located at the Rowland circle allows the x-ray diffraction rays to pass into the SCDI box.

7. Z pinch self-emission imaging

X-ray backlighting methods at Z have been adapted to provide monochromatic imaging of the Z pinch[68,69]. For standard backlighting, Z load self-emission was an unfocused background, but the geometry has been modified so that the focus is on the source and included features that pass only a

small band of x-rays that the source may emit. The imaging geometry and technique is very similar to that shown in Figure 36 with two important differences. First, the "object" is, in fact, the x-ray source located within the Rowland Circle. One important feature is an aperture placed at the Rowland circle along the output path of the x-rays which sets the x-ray pass band; the position along the circle is set according to the Bragg angle of the desired x-ray, and the width of the aperture determines the energy acceptance, ΔE. The highest spatial resolution occurs with the angle as close to 90° as possible, but the image must miss the Z target itself, so there is a practical maximum angle of around 80°. Table 6 lists the crystal material and plane, *2d* crystal plane spacing, x-ray energies, and expected spatial resolutions for several self-emission imagers currently deployed at Z.

Multiple crystal imagers—at least three--can fit on the MITL deck. They can be configured to look at the same x-ray energy to provide different views for partial tomographic reconstruction, or they can be set to different parts of the x-ray spectra. For instance, line and continuum radiation may have different spatial features, or it may be desired to remove (subtract) the continuum radiation component from a line emission image.

Table 6. Table of some of the self-emission imagers at Z. There are a few other versions looking at different energies with some differences in resolution.

	Ar Imager	High Resolution Continuum X-ray Imager (HRCXI)	Cobalt Imager (CHEWI)
Crystal	Ge 220		Ge 335
2d Spacing (angstroms)	4.0004		1.7255
Bragg Angle (degrees)	82.91	86.0	81.51
			82.83
Energy (keV)	3.123, 6.246, 9.370	3.107, 6.214, 9.321	7.265
			7.242
Purpose	Continuum or Ar spectral line	Highest spatial resolution available	Two crystals/images of Co He-like line and nearby continuum

8. Wolter

The Z Wolter imager produces high resolution monochromatic imaging of the Z target at energies and throughput higher than available using other self-emission imagers at Z (See Section IV-D-7). This was designed to provide much higher resolution and image intensity than equivalent work using TIPC (Section IV-D-2) using Ross Pair image subtraction. Figure 37 (top) shows the principle of operation as well as an example image measured at Z. Figure 37 (bottom) is a diagram of the Z setup including primary components. The diffracting optic is a Type-I Wolter microscope[70] consists of two grazing incidence surfaces, the first a hyperboloid and the other an ellipsoid, with the internal surface being a

multilayer mirror set for a particular x-ray energy. A five-axis axis alignment system (two rotational, three translational) is used before and after Z vacuum to align the optic to the target. Optics exist or has been designed for 17.5 keV, 22.1 keV, and 23.5 keV with a band pass width of 0.7 or 1.3 keV FWHM. The optical magnification is 3.5. The FOV is 8 mm wide. An improvement in SNR of at least 19 compared to TIPC imaging the same source has been measured.

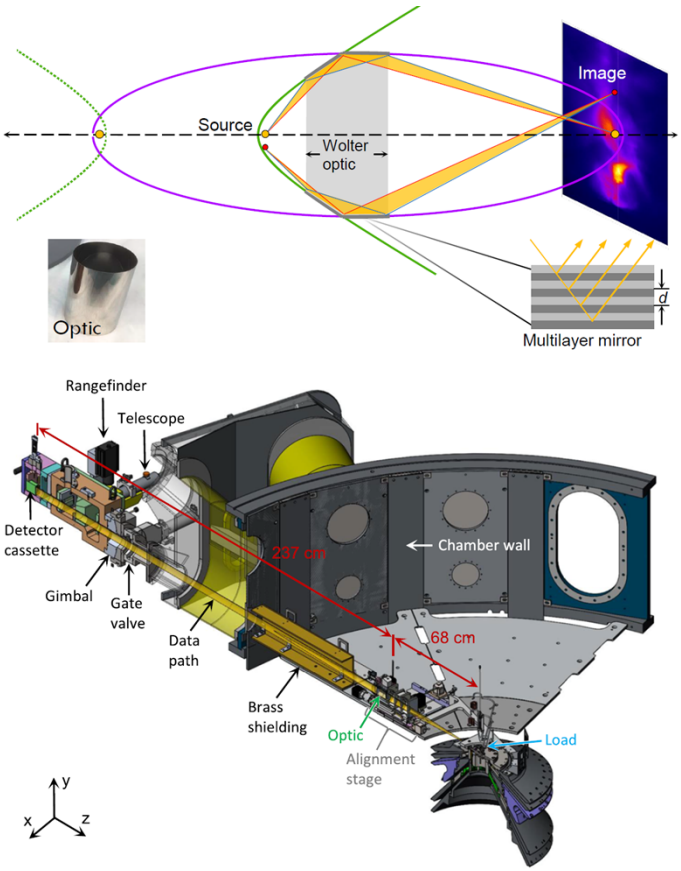

Figure 37. Top: Wolter principle of operation. Bottom: Wolter components as installed at Z.

The geometry is well advantaged for many threats compared to other imagers primary because the optic blocks direct x-rays and debris from the target, and the detector is in one of the diagnostic boats. The reflecting elements in the optic are also shielded from the source with a four-element tungsten baffle with a total thickness of 25.4 mm along with 4.5 mm of polycarbonate for x-ray and debris

shielding, and the optic itself survives the shot (as observed so far). The main challenge with the Z Wolter is tight alignment tolerance given that the depth of field is around 1 mm which means that the alignment and placement of the optic and detector to the load is tight. For full imaging processing, the optic in the equivalent imaging geometry must be characterized in terms of the flatfield profile and a non-stationary point-spread function. The object plane FWHM point-spread function varies with radius from around 75 µm near the center to 300 µm (maximum width of an approximately elliptical PSF) at the outside of the FOV. Currently the instrument is time integrated using image plates, but the design has included the potential to incorporate UXI cameras in the future though best results should be obtained when the hCMOS sensors incorporate GaAs for greater collection efficiency at the Wolter image energies.

E. Power Flow diagnostics

We will now discuss the general category of "power flow" (PF) diagnostics[71] which consists of a wide suite of systems to measure various mechanisms of current delivery or loss at or within the MITL convolute[72] up to the load. Current loss is due to particles or plasmas crossing the MITL A-K gap and may consist of electrons and positive or negative ions of varying charge types or neutral or quasi-neutral plasmas. We will discuss some long-standing systems such as SVS and standard techniques applied to Z for current measurement including some recent improvements. For the past five years, there have been specific Z shots, categorized as "Power Flow", where the load type (see Figure 1B) and diagnostic space and access dedicated for PF with little to no emphasis on the load producing x-rays or for DMP purposes. Various load types are employed that produce different levels of field stress and inductances, some of which are quite "lossy" in order to better measure those losses, or additional inductance is added as a consequence of diagnostic access. However, many other shots contain PF diagnostics as ride-alongs or as one of the shot objectives though not as many as dedicated shots. Figure 38 shows a top view of a dedicated PF shot with several the PF systems indicated. The following sections describe these systems in more detail.

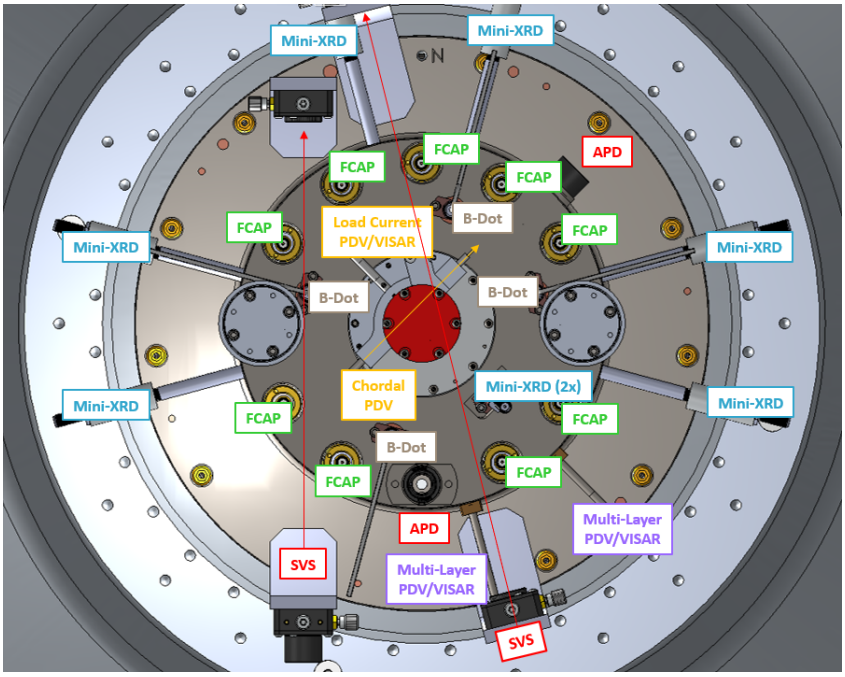

Figure 38. Top-down view of Z3185 power flow diagnostics around the Z load.

1. SVS

Streaked visible spectroscopy (SVS) consists of a series of spectrometers coupled to streak cameras. The light is transmitted to a lab adjacent to the Z high bay via about 80-meter-long fiber optics. There are currently four SVS systems in operation. In recent years, gated spectroscopy has been added. In streaked spectroscopy, the visible spectrum collected light of a single fiber is dispersed and then swept over time so that the final image is wavelength versus time. With gated imaging, multiple fibers can be dispersed in wavelength and then time gated. There is a single-frame gated camera, and an eight-frame camera is being brought online. Example streaked and gated images are shown in Figure 39 and Figure 40.

There are presently four active SVS systems on Z. All four systems use the same 1-m McPherson spectrometers, but two systems have NSTec L-CA-24 streak camera detectors[73] that output onto Kodak T-Max 400 film, while the other two systems use a Sydor streak camera output onto an SI-800 CCD[74], one of which is shown in Figure 41. We are currently in the process of upgrading the L-CA-24 cameras to Spectral Instruments SI-800 CCD[75] outputs. Two different ruled gratings are used for the Z power flow measurements, a 150g/mm grating, which covers a wavelength range of ~220nm, with a resolution of 10 Angstroms, and a 600g/mm grating, which covers a useful range of ~55nm with a resolution of 2.5 Angstroms. The Sydor streak cameras use a Photonis P510 series streak tube with up to 5 picosecond temporal and 10 lp/mm spatial resolution. The 35mm photocathode is S20 on a sapphire window, with a P22N phosphor output. The photocathode sensitivity peaks at 45mA/W at 500nm. The dynamic range

has ~100x gain. The output is recorded on a 2048 x 2048 pixel Spectral Instruments SI-800 CCD camera, with 13.5 microns pixel size and 90,000 electrons full well. The collection and calibration of the data is all done electronically in real-time, eliminating the need for film development and calibration. The detector used for the gated spectra is a Princeton Instruments PI-Max ICCD camera[76]. This camera uses a Generation III filmless GaAsP photocathode bonded to a 25mm diameter image intensifier with a P43 phosphor screen. The phosphor output tapers down to a 1340x1300 pixel, front-illuminated CCD, with 20 µm pixel sizes. This camera is typically gated at 10ns and has a peak quantum efficiency in the visible of >50%.

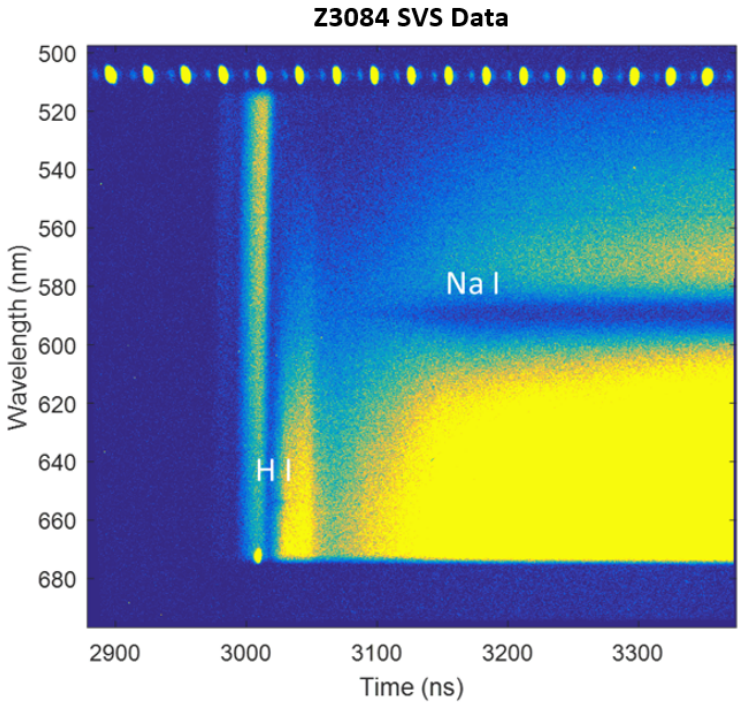

Figure 39. Example SVS spectra. Some absorption lines are noted.

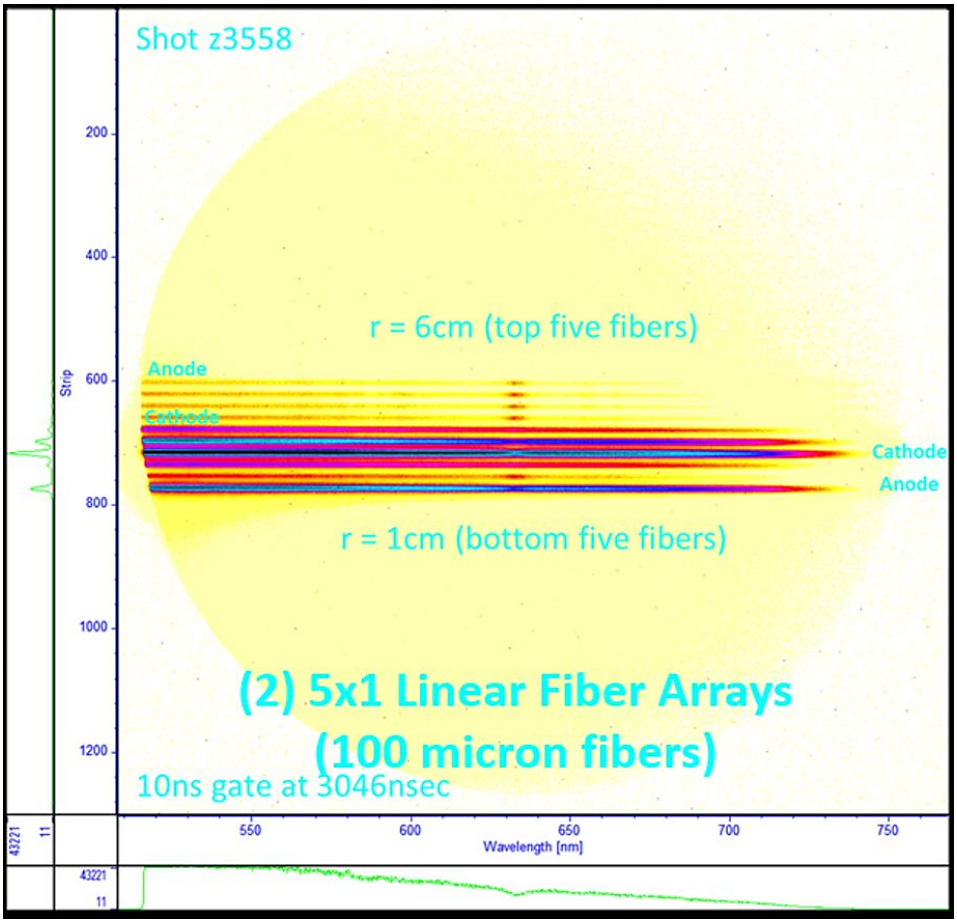

Figure 40. Example gated spectra using fiber arrays.

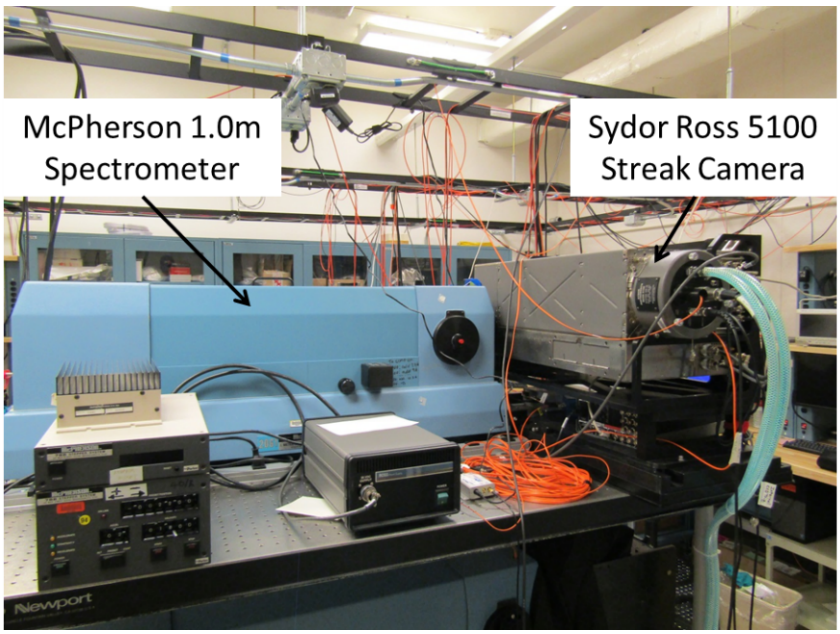

Figure 41. An SVS system showing the spectrometer and streak camera.

2. APDs

Avalanche-photo diodes (APDs) are used to measure visible plasma-generated light as well as electrode surface blackbody emission in the MITL gaps in time and space. The MSTS Model H-EO-53 APDs[77] are built around the Hamamatsu Model S5343 Silicon Photodiode. These detectors have a responsivity of 0.33-20kV/W, with a 5% linearity, and a 1-50x gain factor[78]. They have a quantum efficiency of 80% at 620nm and a photosensitivity of 0.42A/W at 620nm. These detectors are very useful for studying plasma expansion and uniformity of lower density plasmas ($<10^{16}$ cm^{-3}) which propagate ahead of the denser electrode plasmas ($>10^{17}$ cm^{-3}).

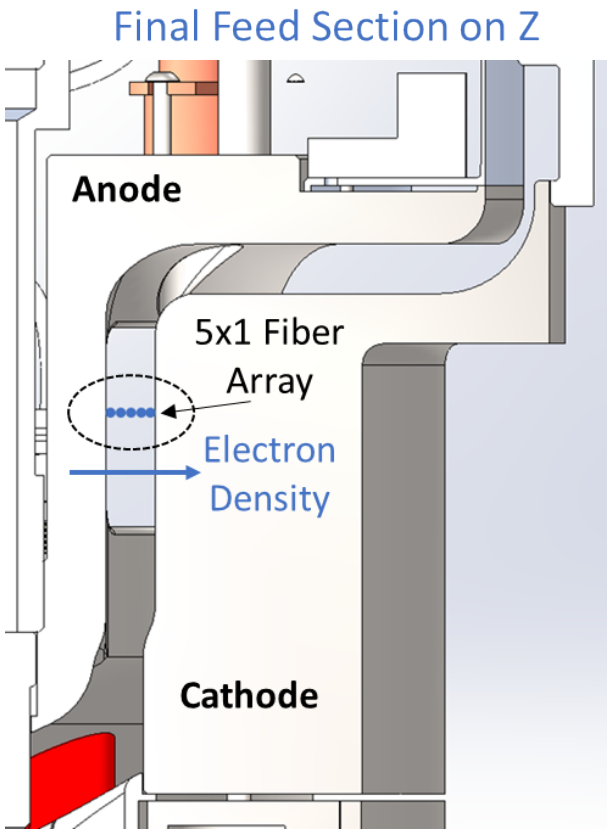

Figure 42. Example fiber array focus position on a PF shot. Some PF shots have a raised extension with slots so that the fibers do not see an opposing metal surface which would produce reflections.

Figure 42 shows an example of the collection regime (1 mm diameter) of an array of fibers in a portion of the inner MITL on a PF shot. These fibers can be used for APDs, gated spectra, or single fibers sent to an SVS system in any desired arrangement. Light is collected from the Z MITLs using a using a 6.35mm, 15mm focal length, glass achromat (Thorlabs Part #AC064-015-A-ML). This optic is positioned 140mm back from the A-K gap on the hardware looking through slots cut into the anode surface to allow for unobstructed lines of sight. The fiber array was positioned so that it imaged light from a focus at the center of the diode. The fiber arrays consist of either 100 or 200 µm diameter Polymico FVP, high –OH, silica, step-index fibers[79]. These fibers have a numerical aperture of 0.22, giving a 25.4° acceptance cone. There is a demagnification of 10x from the imaged plasma light to the collection fiber, resulting in a total collection area of 1mm in diameter through the plasma volume. Example APD data is shown in Figure 43.

X-ray backgrounds and particle bombardment from uninsulated electrons are the main threats to the APD data since they produce an early-time signal at a similar time and amplitude to the plasma light though the absolute and relative magnitude varies depending on the fielding location. A “top-down” view appears to be the worst. A side-on view (Figure 42) is more benign with relatively low backgrounds as seen in Figure 43. There is a “null” channel often fielded where the input fiber is “blacked” out where it is hoped that the x-ray background can be subtracted from the other channels, but from the existing attempts thus far, it appears that the background is not always consistent among the fibers based on the orientation of the individual fibers in the arrays to the hardware.

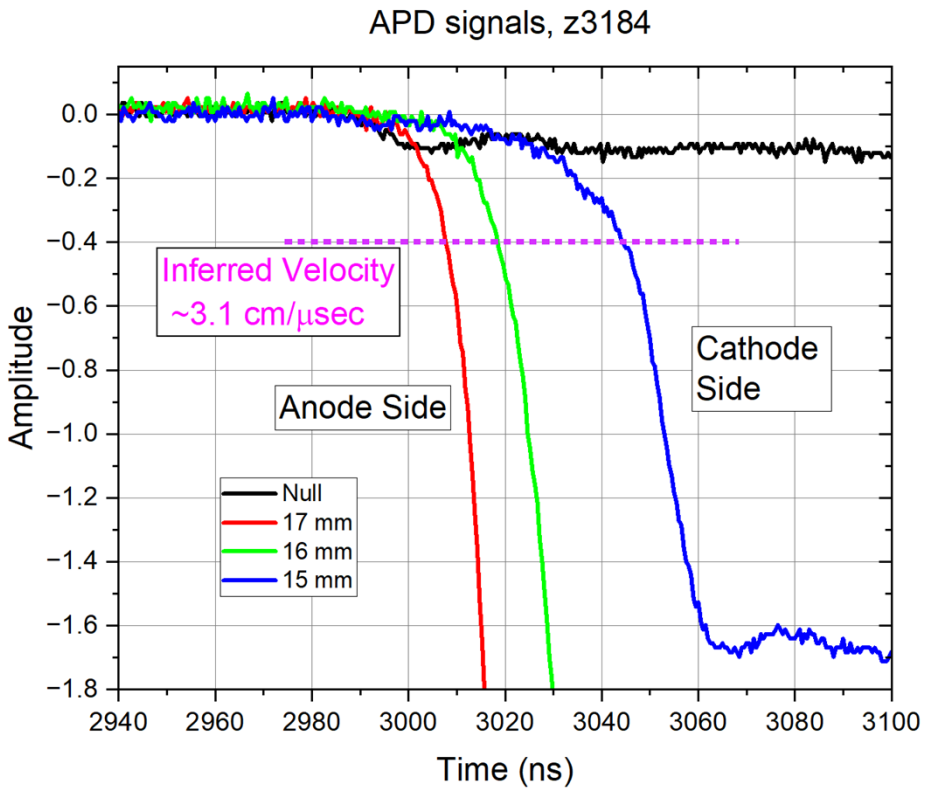

Figure 43. Example APD data from an array (similar to Figure 42) where an approximate plasma velocity is inferred when the signal passes a low threshold. The signal names reference different positions within the gap but not necessarily as measured from either the cathode or anode. The “null” channel is sensitive to x-ray backgrounds but not visible plasma light. The dashed line indicates the choice of threshold for velocity determination.

3. FCAPS and MiniXRDs

A set of PF monitors have been integrated into the anode looking[80] at various mechanisms or source of current loss. One is known as Faraday-Cup Anode Posts (FCAPs) which are modified versions of the standard convolute posts where the center is hollowed-out to admit cylindrical copper or tungsten electrodes connected to the center conductor of an SMA connector at the top of the post as shown in Figure 44 (left). Each of the twelve convolute post positions can include FCAPs. The goal is to measure electron and negative ion currents hitting the convolute posts. Various apertures with different orientations can view the directionality of the incident beams. Thin copper filters are incorporated to eliminate ions and neutrals. Example FCAP data is shown in Figure 45.

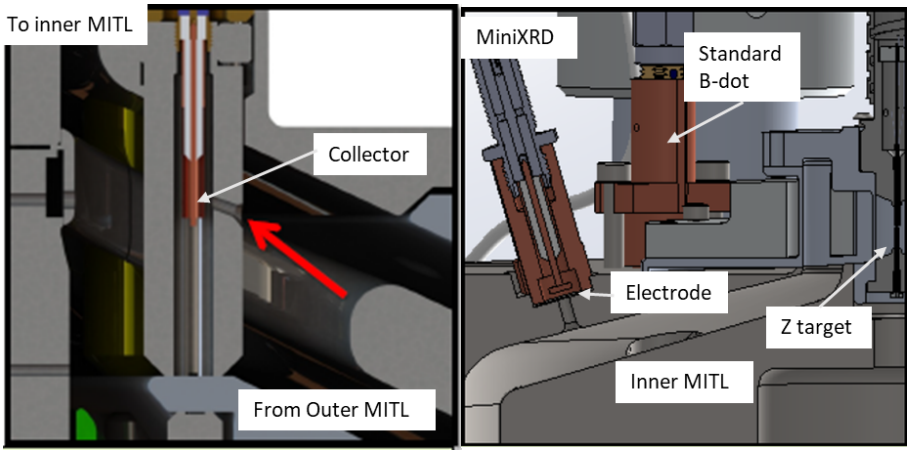

Figure 44. An FCAP (left) and a MiniXRD (right). The opening of the FCAPs can face different directions and angles. The red arrow indicates the direction of incident particles into the FCAP aperture. MiniXRDs can be fielded at different locations, and ones having a longer stand-off than shown reduces backgrounds from negative particles striking the electrode.

Similar in appearance but with a different purpose, MiniXRDs are negatively biased electrodes meant to respond to the UV photons emitted from the MITL cathode surface which is rapidly heated to > 1 eV blackbody temperatures by bound current resistive heating or positive ion impacts. Example MiniXRD configurations are shown in Figure 44 (right). Since the electrode response to UV light is predictable, the effective blackbody temperature can be estimated versus time. Since no filters can be allowed for this measurement, MiniXRDs are susceptible to negative particles which can confuse interpretation, but increasing stand-offs reduce this background.

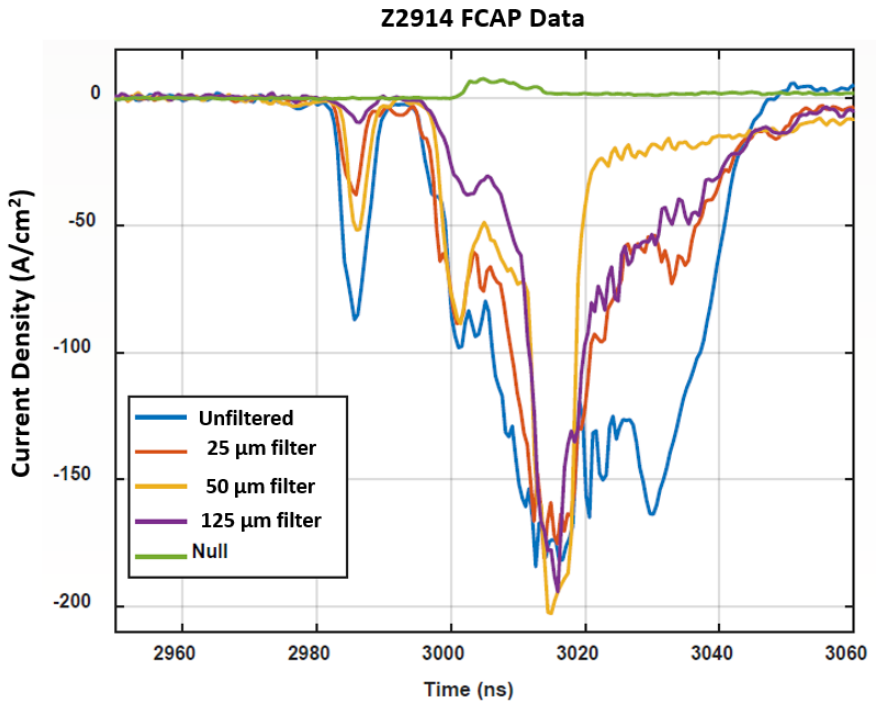

Figure 45. Example FCAP data showing five FCAPs on the same Z shot (different MITL convolute posts) with different thicknesses of copper filters. The "null" measurement has no opening for particles, and therefore any signal would likely be generated from the cable. The copper filters are only relevant for electrons since these thicknesses will block any ion with energies likely generated in the Z MITL.

4. IDTLs

Inductively driven transmission lines (IDTLs) were originally designed to "siphon" off a portion of the Z current close to the load in order to drive external x-ray sources for backlighting purposes[81]. However, their primary purpose is now to be an alternative to the standard B-dots (of which there are a few types) to measure current delivery to the load[82]. The standard B-dots seem to be reliable only up to a certain point rise, but sometimes appear to deviate from the MITL current approaching and beyond peak current as judged based on circuit models and velocimetry unfolds. A significant intent of fielding IDTLs (which has become much more evident as experience with them as grown) is to measure the MITL current more accurately for longer times irrespective of the load type. As shown in Figure 46, IDTLs consists of a single large area (relative to standard B-dots) loop that is exposed to the magnetic field of the Z current in the inner MITL. Currents on the order of 100-200 kA may be driven through this loop depending on the exact design. The loop can be shorted back into the anode or terminate in an x-ray producing load. This secondary target can be intended to produce x-rays for point-projection imaging such as an X-pinch[83,84]. Efforts to develop and test an X-pinch has progress and preliminary data has been taken at Z. However, the primary application of IDTLs has used the shorted version as a current

diagnostic. In either configuration, current through the IDTL is measured via B-dots of similar construction as the standard Z B-dots. Single or multiple B-dots or even Rogowski coils have been tested as IDTL internal probes. It is believed that IDTLs behave better than standard B-dots for two main reasons. First, standard B-dots directly view the MITL power flow region and may be subjected to plasma impacts and particle flows. The IDTL internal probes are hidden from the inner MITL. Second, IDTLs can increase signal-to-noise ratio compared to standard B-dots. One source of noise is "cable drive" (a generic term indicating current driven in the cable by whatever means such fringe magnetic fields from the MITLs). Variable sensitivities to the MITL current are readily achieved well beyond that of the standard B-dots, thereby increasing the signal over the noise (assuming relatively constant compared to the standard B-dot). Rogowski coils offer the best means of tailoring the signal level. Figure 47 shows example current probe data, IDTL and others, on a Z shot indicating the lower noise of IDTLs compared to the standard B-dots.

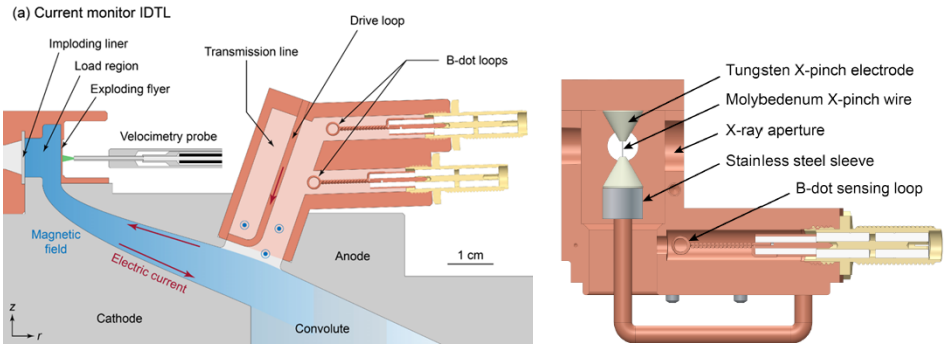

Figure 46. Left: an IDTL used for inner MITL current measurements at Z. Right: an IDTL used to drive a hybrid x-pinch.

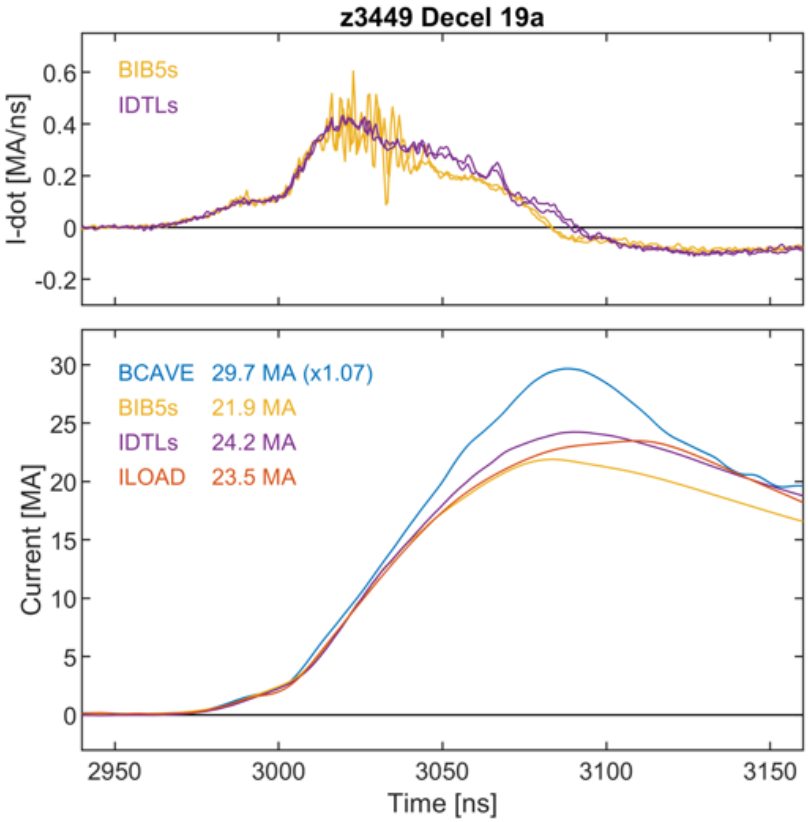

Figure 47. Top: example IDTL waveforms at Z with comparison to a standard style of B-dot. Bottom: comparison of inner MITL current measurements. ILOAD is inferred from velocimetry and BCAVE is from upstream B-dot probes time-translated to the load.

5. CIDZ

Faraday cups, such as the FCAPs mentioned earlier, have been fielded at several locations in the inner MITL to varying levels of success. They are designed to measure charged particle currents consisting primarily of protons or negatively charged hydrogen ions striking the anode or cathode surfaces of the MITL. The Cathode Ion Detector at Z (CIDZ) is one example where Faraday cups reside opposite the convolute posts as a complementary measurement to the FCAPS. Space has limited the number of faraday cups to four, but in earlier iterations of CIDZ radiochromic film (RCF) has been fielded in cavities buried in the cathode metal. Figure 48 shows a side-on view of one the CIDZ design and a color scan of one of the RCFs in one of the first shots. Later shots had more significant debris which usually destroyed the RCF which is only protected by about 8 µm of Kapton (to allow protons of approximately >500 keV energy to penetrate), so the RCF component of CIDZ is not often included anymore.

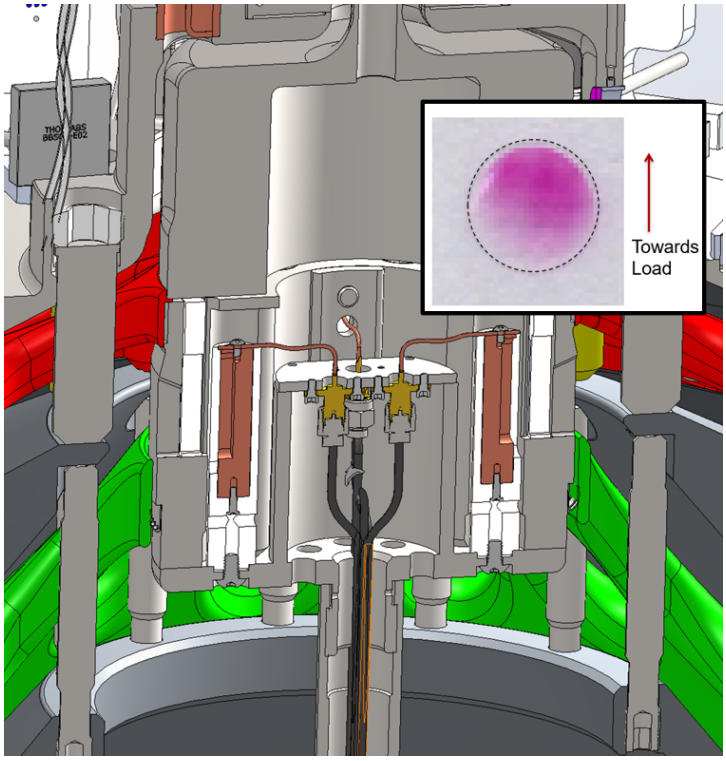

Figure 48. One version of CIDZ with a cut-away showing the faraday cups. The inset imaging is a scan of an RCF located at a similar position as the faraday cups but on a separate shot.

A particular lesson during CIDZ development is relevant to other diagnostics that may be located below the load, particularly ones that need connection of cables or fibers. Since the faraday cups of CIDZ are integrated in the cathode, a specially designed device is used to provide inductive voltage isolation of the cathode to the grounded bottom lid. This is called the Time-Transit Isolator (TTI) mounted on the bottom vacuum lid that incorporates a large inductor through which the CIDZ cables are routed. There are a few meters of free space between CIDZ and the TTI. The first versions of CIDZ tied the RG-405 cables together inside stainless steel braid. On the first Z shot, the CIDZ signals picked up a large negative signal whereas a positive signal was expected. One possibility was that electrons may stream out of power flow gaps in the MITL before the convolute and strike the cable. Another possibility is electron emission from the cable/braid which may be retrapped. Regardless, this signal was a background which must be eliminated for the desired measurement. The next version of CIDZ incorporated a solid steel pipe which removed the negative going signal and a positive signal was detected indicating proton detection in the faraday cups. Comparison of two signals before and after

the steel pipe was introduced is shown in Figure 49. Development of CIDZ continues in methods to obtain a well quantified proton signal that does not include co-moving electrons or saturation effects (often excessively large signals are observed which may break down cable connectors). Other diagnostics fielded in a similar location may need to incorporate similar shielding strategies as CIDZ. One benefit of electrical measurements "bottom-side", with or without the TTI, is relatively low EMI.

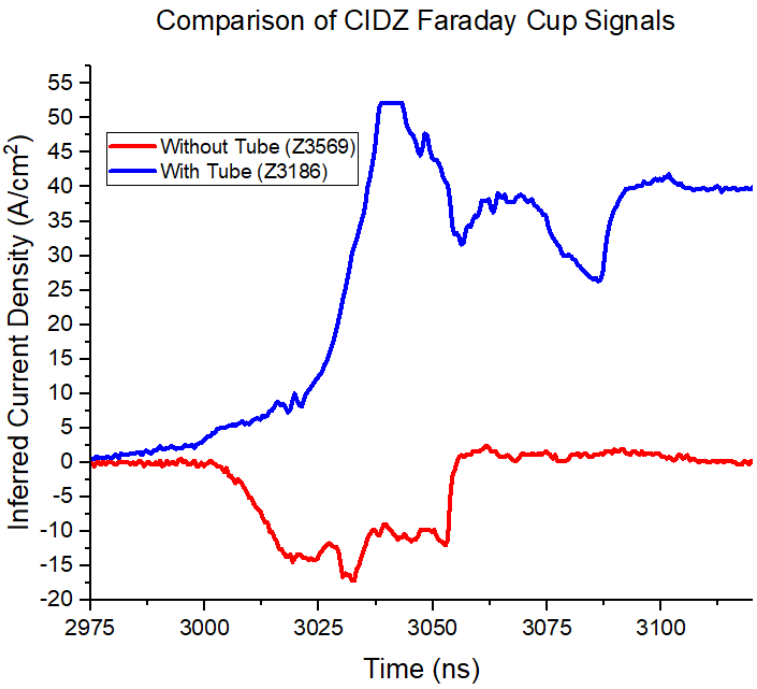

Figure 49. CIDZ signals before and after introduction of shielded cable tube.

6. SEGOI

A relatively new diagnostic called SEGOI (Self-Emission Gated Optical Imager) was developed to image visible self-emission that typically arises due to low density plasmas that form on and near Z targets. In particular, plasmas form in the anode-cathode gaps that deliver the electrical power to the Z target and may be responsible for driving several megaamperes of current loss. SEGOI uses an in-chamber lens and periscope to create images of Z targets or power flow gaps from a side-on configuration that couple to the existing Z Line VISAR (Section IV-F-3) infrastructure. The image is relayed over ~50 m to eight gated optical imagers (>100 ps gate, 540-650 nm) and two streak cameras (62 and 94 ns streak duration). For this diagnostic, commercial off-the-shelf optics were identified to reduce the overall cost and lead-times compared to Z Line VISAR experiments. The system is configured to image targets along LOS110, although off-axis configurations have been implemented to image targets near the z-axis of the Z Machine using mirrors that redirect the imaging field of view (see Figure 50). To date, SEGOI has been

used to image a variety of self-emitting phenomenon, including low density plasmas in power flow plasmas (see Figure 51), plasma formation on the twisted return posts of a dynamic screw pinch[85], and self-emission of a target designed to study the magneto Rayleigh-Taylor instability, similar to that studied in reference 86.

The field of view and resolution of SEGOI were characterized using an in-chamber USAF1951 resolution target. Using a 3 inch diameter, 400 mm focal length, MgF_2, achromatic doublet lens from Edmund Optics[87], the resolution on the GOIs varies from 10 lp/mm (50 µm wide bar) to 7 lp/mm (70 µm wide bars). The alignment camera resolution using this system is 20 lp/mm (25 µm bars) and comparable to the resolution on the streak cameras. The GOI resolution is most likely degraded from the intensifiers, although the beam-splitting configuration is responsible for degradation across the GOIs themselves. For typical SEGOI configurations, the field of view is approximately 8 mm.

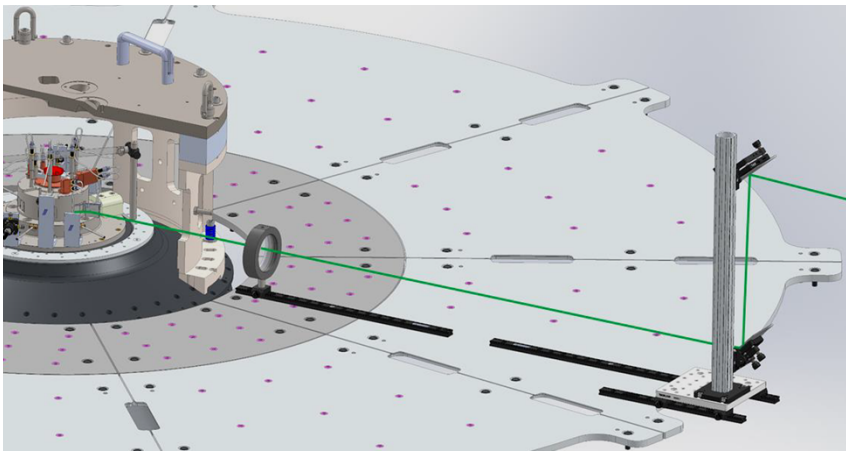

Figure 50. Rendering of SEGOI periscope and lens assembly in Z vacuum chamber. The periscope directs the optical axis (green) towards the Z target along LOS 110.

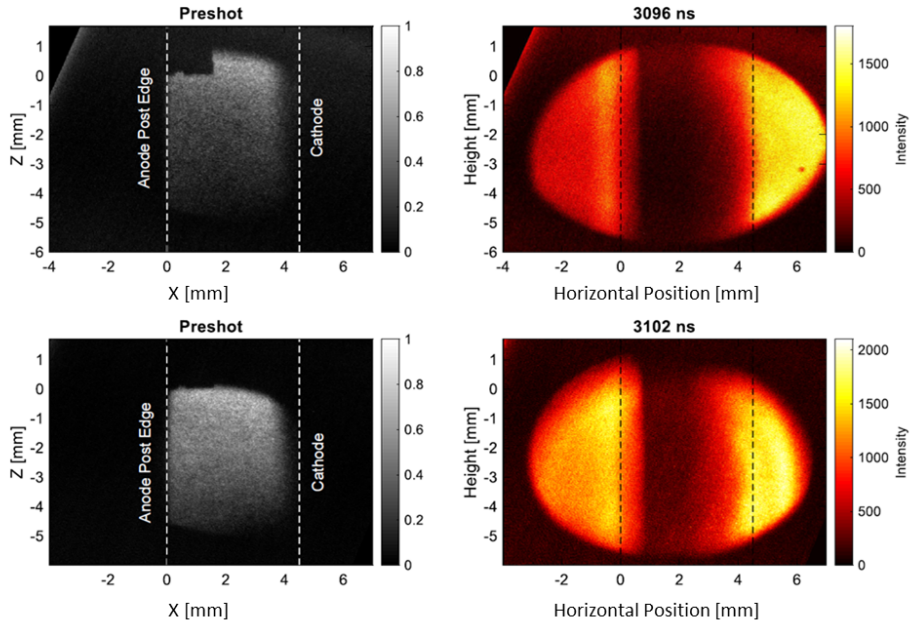

Figure 51. Preshot and self-emission data of plasmas forming on anode and cathode transmission lines leading up to the Z target on two shots (top and bottom of the figure). A pre-shot image is taken with illumination to show the vacuum gap in the MITL. The nanosecond time indicated is near peak current. Plasma on the cathode is dynamic and non-uniform. For reference, the dashed lines mark the initial position of the anode and cathode.

F. Velocimetry

Optical velocimetry is used to measure continuous motion at Z. These techniques are based on the relativistic Doppler shift from the lab frame to the moving frame of a target and back to the lab frame. That double transformation shifts the original wavelength λ to the observed wavelength:

$$\frac{\lambda}{\lambda_0} = \frac{c - v}{c + v} \approx 1 - \frac{c}{2v} \quad (4)$$

where v is the target velocity and c is the speed of light. The approximation holds for velocities much slower than the speed of light, with the convention that wavelength increases with motion towards the observer.

In practice, Doppler-shifted wavelengths differ only slightly from the original wavelength. For example, 1 km/s of motion changes wavelength by less than 7 ppm, which is 3—4 pm at 532 nm. Such changes

are too subtle for dispersive spectroscopy, so interferometry techniques are typically used. Figure 52 shows two interferometry configurations for measuring Doppler shift.

1. Photonic Doppler Velocimetry (PDV)[88,89] mixes light reflected from a target with a reference optical signal. The measurement involves a mixture of shifted and unshifted light.
2. Velocity Interferometer System from Any Reflector (VISAR)[90,91] separates reflected light into a reference and delay path. The measurement involves only Doppler-shifted light.

Velocimetry or its infrastructure is applied in several ways at Z. These include:

- Equation of State (EOS) of material compressed on DMP load targets (Figure 52).
- The local Z current is inferred by "flyers" of aluminum or copper which can be placed near the load driven by the magnetic pressure. These materials are used because the EOS[92] are well known, and the Z current is determined by inverse calculations and simulations[93,94] .
- Plasma densities can be determined[95] by the index of refraction changes along the path of the laser light which is detected as a positive velocity because the free electrons decrease the real index below unity.
- Prompt radiation detection has been demonstrated at Z using velocimetry[96].

Details of (point) PDV, VISAR, and photonic displacement interferometry (PDI) will be given in the following sections. Multiple interferometer systems provide experimenters significant flexibility in designing a broad range of experiments including complex experimental configurations involving multiple velocimeters and an increased amount of data recorded on each shot. We will conclude the velocimetry section with a summary of the Line VISAR system recently commissioned at Z.

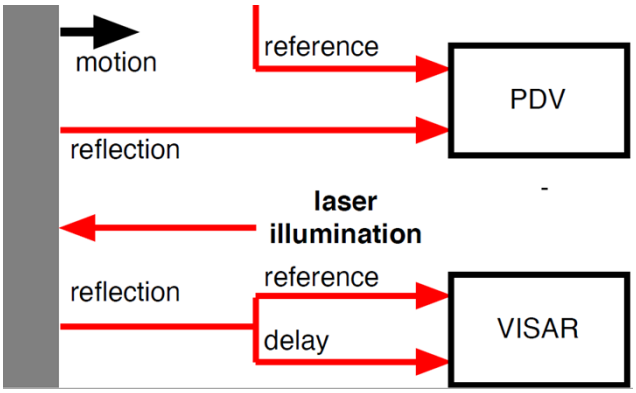

Figure 52. Interferometry configurations for PDV and VISAR.

1. PDV

PDV is based on the mixture of two optical signals. The resulting beat frequency:

$$B = \left| \frac{c}{\lambda_0} - \frac{c}{\lambda_R} + \frac{2v}{\lambda_0} \right| \quad (5)$$

depends on the illumination wavelength λ_0 and the reference wavelength, λ_R, as well as the target velocity, v. The simplest implementations of PDV use a single laser ($\lambda_0 = \lambda_R$), resulting in a direction-blind measurement. Two laser systems offer greater flexibility: beat frequency can increase or decrease with velocity, depending on how the lasers are tuned.

PDV is a relatively new diagnostic at Z. To understand why, consider a single laser measurement at 532 nm. The resulting beat frequency is about 3.76 GHz per km/s. One interference fringe occurs each time a sample moves half a wavelength, so the ability for tracking velocity scales directly with measurement bandwidth. Until the turn of the century, measurements of this type were limited to a few hundred meters per second[97]. Other developments in the telecommunications industry make PDV practicable for use at Z including the use of stable and tunable near-infrared lasers, improvements in low-loss single mode optical fibers, three-port optical circulators, and fast InGaAs receivers and > 10 GHz digitizers. All of these have allowed PDV at Z to measure velocities below 1 km/s to above 10 km/s.

2. Point velocimetry systems at Z

Most VISAR and many PDV measurements are performed with bare fiber probes. Laser illumination travels down one fiber, reflects from the sample, and is collected by 2--3 receive fibers. The standard configuration combines both diagnostics into a "Romulan" probe, where three single-mode and four multi-mode fibers are closely packed with each other. Numerous variations of the unidirectional approach are fielded: sometimes a spare multimode fiber is used with streaked visible spectroscopy, and the multimode fibers may be low-OH silica for infrared pyrometry instead of VISAR. Imaging probes, which focus the ~0.01 mm core of a single-mode fiber onto the sample, are generally used in PDI measurements and some PDV measurements. The bidirectional approach---light sent and collected on the same fiber---is almost always more efficient than the bare fiber approach but is not currently supported by VISAR. PDV is considerably more flexible in this regard: probes can be bare fiber, imaging, or even collimating. The latter is particularly convenient for rough surfaces, retroreflectors, and plasma detection.

Velocimetry system choice, at least at Z, is principally driven by velocity range:

- VISAR is poorly suited to velocities below 10 m/s. PDI is optimal in this range, and PDV can operate with careful system configuration, probe design, and data analysis.
- VISAR works well for velocities above ~100 m/s to over 100 km/s.
- PDI is limited to velocities below around 1 km/s.
- PDV does not directly support velocities larger ~20km/s, although leapfrog[98] measurements can track Doppler shifts exceeding the ~25GHz receiver/digitizer bandwidth. Time-stretch techniques[99] can be used to ~100km/s, though this capability is still being developed.

There is a portable/hybrid PDI/PDV system available at Z that is also used (transported) to other facilities such as the NIF[100]. Capabilities of the portable PDI/PDV system overlap with the permanent PDV and fiberoptic VISAR systems, the pragmatic differences being the velocity ranges for which each architecture has been optimized, and additional recording capacity. Because the PDI system has a

comparatively low pre-shot noise floor of ~0.02 m/s (rms) it is most often used to measure velocity fluctuations of ~0.1-100 m/s in amplitude over periods ≥ 1 ns. The system is primarily used to interrogate velocity field structure resulting from shock in heterogenous materials (e.g., granular, porous, or additively manufactured materials), ejecta, phase transitions, low-density plasmas, structural and impulsive loads, pressure and energy time-of-arrival, and for thermoelastic calorimetry (e.g., to corroborate x-ray yields). The recording system currently allows up to 17 channels of PDI for velocities up to 775 m/s and 32 channels of PDV (24 channels for velocities up to 4,650 m/s and 8 channels for velocities up to 620 m/s). The PDI and PDV modules can also be combined for a total of 43 recording channels. An example of measuring material motion using PDI is shown in Figure 53 for sapphire-backed iron samples subjected to surface heating from a ~3.3 keV x-ray pulse using an argon gas puff load[101]. After the initial offset from irradiation of the optical fibers, small differences in the net sample motion arising from momentum transfer and ensuing shock reflections can be identified between the two sample exposures.

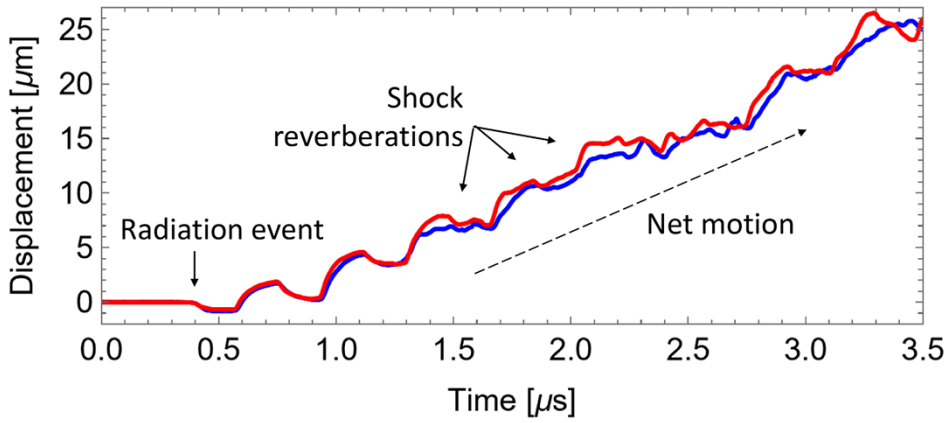

Figure 53. PDI data from a material sample shocked by Z radiation burst.

The main threat to point velocimetry at Z is fiber darkening and fiber refractive index changes. Radiation produced by the Z machine, either by intent or unexpected current loss, may prevent light from reaching the target and/or returning to the diagnostic. Almost any radiation producing shot can affect unshielded fibers. Even with shielding, velocity artifacts are often encountered on many loads other than long-pulse coaxial loads. Strip-line shots and standard pulse experiments, particularly wire arrays and gas puffs, produce radiation that penetrates any flexible metal jacketing. Features associated with current loss, presumably Bremsstrahlung, as well as load radiation (as in MagLIF experiments) are often detected which can appear as a velocity artifact. Catastrophic failure seems to be most common with VISAR, even while PDV measurements continue to function in the same environment. PDI has a long history of operating in radiation-producing experiments, with adequate shielding, though negative-velocity artifacts are still observed. The current understanding is that radiation-induced color centers

directly attenuate visible wavelengths while only modulating the refractive index of infrared wavelengths. Mitigation measures include adding flexible shielding around the fibers and the use of rad-hard fibers as well as experience on exactly where and how to place and mount fibers to the Z hardware.

3. Line VISAR

Recently included in the suite of velocimetry diagnostics for Z is an imaging line VISAR system (ZLV) developed in collaboration with Lawrence Livermore National Laboratory[102]. As compared to "point" VISAR or PDV which are based on fiber optics, line VISAR is an open beam system that spatially resolves velocities along a line as recorded by a streak camera. Z Line VISAR generates a 2D streaked velocity map in time and space. The primary objective of the ZLV diagnostic is to quantify the spatial profile of the current delivery, which includes identifying the location and timing of any current loss that might be shunted near the load[103].

Figure 54 shows a CAD model of the commissioning load hardware with the ZLV final optics assembly positioned above it. A custom f/2 objective lens collects 532 nm laser light reflected from the load. The fast f/2 lens collects a wide angular range of reflected light, maximizing the allowable tilt the sample can undergo while in motion during an experiment. The spatial resolution of optical system is ~3 µm at the target while the effective spatial resolution of the velocity map is limited by the fringe density and contrast on the streak camera which for the commissioning experiment was ~60 µm. The lens assembly is part of the consumable inventory associated with each experiment. Figure 54 shows an image of the final optics assembly setup before the commissioning shot and the position above the Z load. The optics assembly above the target is destroyed along with the rest of the target. The instrumentation for the ZLV diagnostic is located 50 m away and is linked to the target via a relay imaged beam transport system. The key performance characteristics of the ZLV instrumentation are:

- Max spatial resolution of 10-20 µm
- Max temporal resolution of 20 ps
- Anamorphic lens pairs create 1, 2 and 4 mm fields of view at the target
- A fast lens (f/2) to accommodate tilting of the shock front
- Two independent interferometer legs to help resolve fringe jump ambiguities

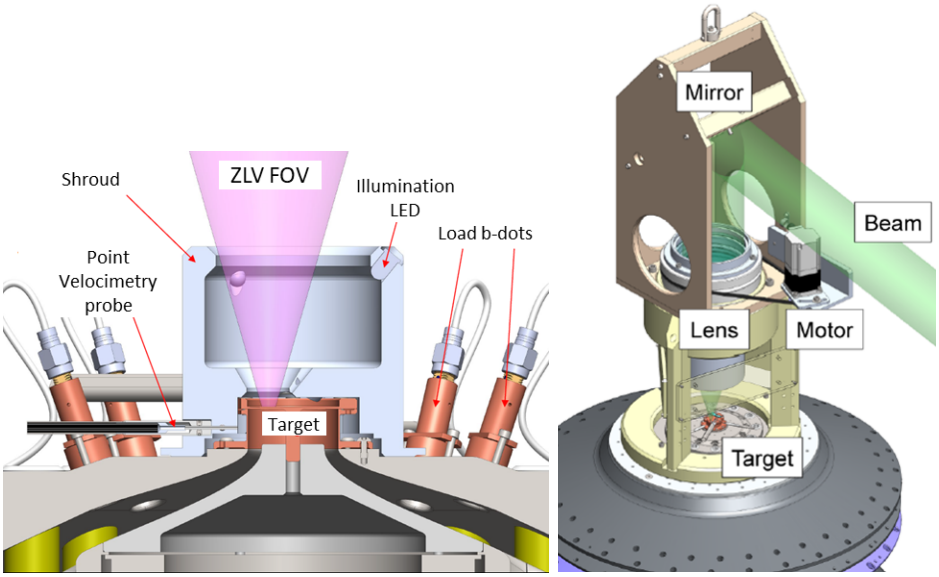

Figure 54. Target geometry for the commissioning shot Z3337 and diagram of the final optics above the load.

Figure 55 shows the data and resulting velocities from a commisioning shot. Data is collected across two "legs" onto two steak cameras that can have different sweep speeds. The curved discontinuity shown in Figure 55a in the middle of the sweep corresponds to the magnetically driven shock breaking out of the surface. For this shot, the effective spatial resolution at the target is ~70 µm with effective temporal resolutions of 0.2 for the data shown here. Comparisons of the velocity data (Figure 55b) with 2D forward calculations are shown in Figure 55c. Note that the color scale in Figure 55d, which is a difference map between the data and simulation, spans just ±10% of the color scale of Figure 55b and Figure 55c . In panel (d), the post-shock region is outlined in magenta where the mean and standard deviation of the differential velocities is 43 ±85 m/s which is within the error bar of the ZLV measurement. The 2D simulations were performed with the GORGON 2D code[103]. This shot, which was designed conservatively to avoid significant current loss, used a non-imploding load which also produces a relatively low radiation output. One threat to ZLV which has been observed on some shots is that the return signal "blanks" or disappears due to a loss of reflectivity of the optics. This effect is currently under investigation.

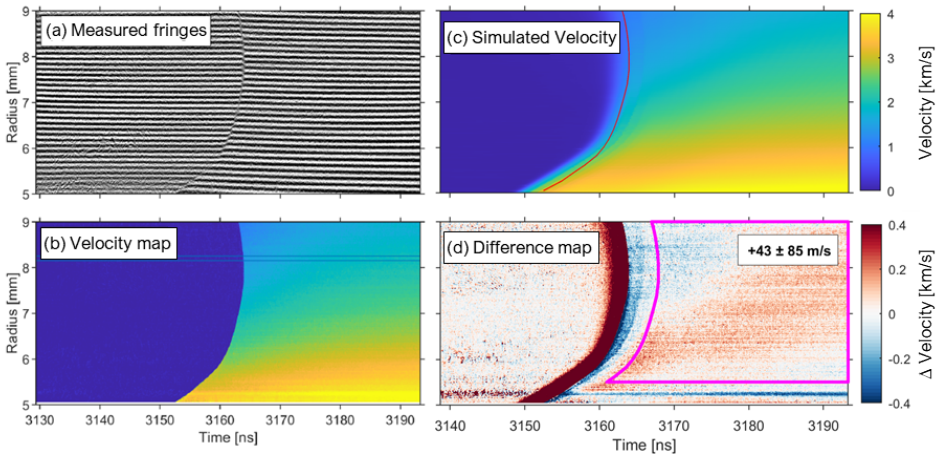

Figure 55. Line VISAR data from the commissioning shot, Z3337. Panel (a) shows the measured line VISAR fringe positions versus time. The curved discontinuity in the middle of the sweep corresponds to the magnetically driven shock breaking out of the surface. Panel (b) shows the velocity map derived from the fringe shifts. Panel (c) is a GORGON 2D simulation of the velocity of the shot configuration. Panel (d) shows the difference between the code result and the experiment.

G. Nuclear Detectors

In this section, we group diagnostics designed to respond to neutron production in a MIF target either through the D-D or D-T reactions (some D-T reactions occur from the tritium reaction product of the D-D reaction). Neutron yield (total number of neutrons produced) is usually the primary measurement which is measured through activation foils. The neutron spectrum is often the next highest priority which is measured by the NTOFs. These systems were developed earliest. It is more difficult to measure the "burn-history" or the rate of production of neutrons which occurs around the time of the z-pinch. X-ray signals have been used as a rough stand-in for the burn history though it is known that they differ in time to some extent. Developing diagnostics including the ACD, GRH, and PRT, described in this section, are efforts to measure the burn-history directly though x-ray backgrounds are a significant threat against which considerable efforts are being brought to bear. D-T reactions provide better opportunities to measure the burn history around which the GRH and ACD is designed.

1. Neutron Activation

For the MIF work at the Z-facility, the primary fuel is deuterium. For a deuterium-deuterium (DD) fuel, the thermonuclear reactions of interest are the following.

$$ {}_1^2D + {}_1^2D = \begin{bmatrix} {}_1^3T(1.01\ MeV) + p^+(3.02\ MeV) \\ {}_2^3He(0.82\ MeV) + n^0(2.45\ MeV) \end{bmatrix} $$

(6)

$$ {}_1^2D + {}_1^3T = {}_2^4He(3.5\ MeV) + n^0(14.1\ \text{MeV}) $$

(7)

The primary reaction is given in (7) and results in two product paths with nearly equal branching rates, one of which produces DD-neutrons. Tritium produced in the primary reaction also undergo fusion with deuterium producing DT-neutrons. The primary DD-neutrons are essentially 2.45 MeV while the secondary DT-neutrons are a distribution around 14.1 MeV. Neutron activation diagnostics rely on threshold reactions where only neutron energies above an understood value create activity in the diagnostic material that undergoes a decay process that is measured. Through the measure of activity, the number of neutrons produced in the fusion experiment can be inferred. Assuming neutrons are emitted isotropically, the expression for the neutron yield is given by the following.

$$ Y = \frac{4_\pi \text{No} < \text{d2} >}{mhF} $$

(8)

where:

$$ N_o = \frac{(C - B)}{e^{-\lambda}\,t1 - e^{-\lambda}\,t2} $$

(9)

In this expression, N_0 is the number of activated nuclei, C is the number of counts, B is the background counts, m is the mass of the activation sample, F is the detection system's calibration factor of the reaction of interest, h is a correction factor to the calibration factor that relates the calibration environment to that of the scattering environment in the experiment, t1 is the time from the implosion to the time where gamma counting begins, t2 is the time from the implosion to the time when gamma counting stops and $\lambda = \ln(2)/\ \tau_{1/2}$.

Activation materials and their properties are summarized in Table 7 below along with other activation materials used at the Z-Facility[104]. The threshold energy of a given reaction is an important method to discriminate between D-T neutrons and D-D neutrons. The primary yield diagnostic for D-D neutrons are the indium samples. Copper is usually used for D-T neutrons. However, due to the short half like of Cu-62, the copper samples are placed in a reentrant tube called the "rabbit tube" so that the samples are placed close to the load (about 32 cm) but also in air for quick retrieval. References 105 and 106 describe methods and processes for the activation samples at Z. Figure 56 shows the placement of the activation samples around the Z load. The location of the in-chamber diagnostics are the top, side and bottom of the blast shield. In those locations the activation samples can be either indium or zirconium. In a typical experiment three samples are placed on the top, side and bottom of the experiment. Typically, eight of the nine samples on the blast shield locations are indium and one is zirconium.

A yield diagnostic outside the chamber is the Be-probe[107]. It is located on the mezzanine of the Z-machine. Its radial location (on the horizontal plane) from the target center is 310° and has a view of the target at 12°, 6 meters from the load. The He-6 decay is measured with a scintillator and PMT.

Table 7. DD and DT reactions used in neutron activation detectors.

Neutron type	Reaction	Recorded photon energy	Half-life, $\tau_{1/2}$	Neutron Threshold energy
Y_{dd}	$^{115}In(n,n')^{115m}In$	E(γ) = 336 keV	4.49 h	0.38 MeV
Y_{dt}	$^{115}In(n,2n)^{114m}In$	E(γ) = 190 keV	49.51 d	9.04 MeV
Y_{dt}	$^{63}Cu(n,2n)^{62}Cu$	E(γ) = 511 keV	9.67 m	11 MeV
Y_{dt}	$^{90}Zr(n,2n)^{89}Zr$	E(γ) = 909 keV	78.41 h	12 MeV
Y_{dd}	$^{9}Be(n, \alpha)^{6}He$	E(e^-) =3.5 MeV	807 ms	0.67 MeV

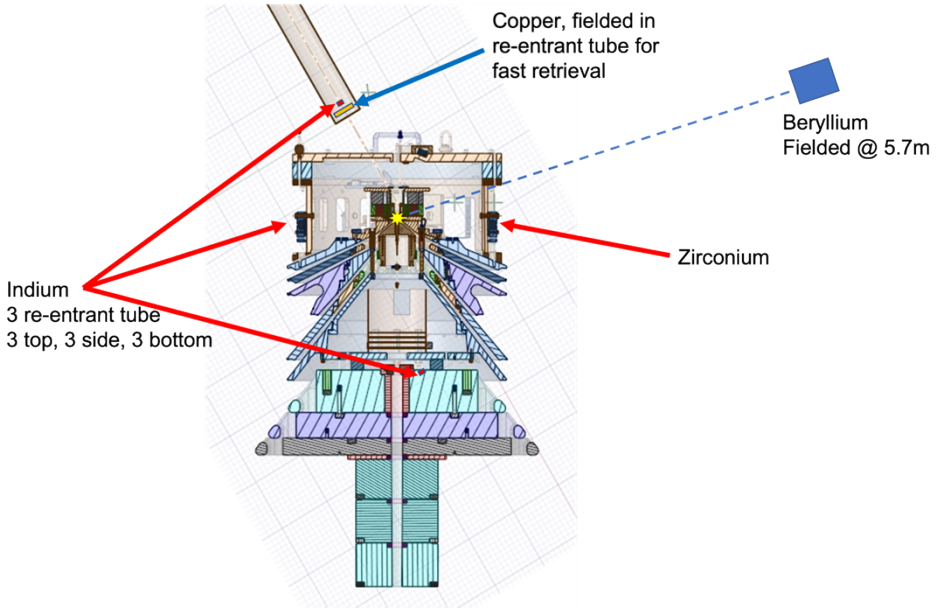

Figure 56. Position of neutron activation samples relative to an MIF target.

2. NTOF

Neutron time-of-flight (NTOF) detector systems are designed to measure the neutron energy spectrum from a fast burst of neutrons as inferred from the neutron time-of-arrival at the detector. D-D or D-T neutrons have a well-known energy spectrum (about 2.45 MeV and 14.1 MeV, respectively), but there is a spread in the spectrum that relates to temperature of the ions in the reaction. Additionally, the

relative amount of low energy neutrons associated with neutron scatter can be used to infer information about the cold material (fuel or liner) density-radius product in the target. NTOF detectors are fielded far away from the load to allow the distribution to increase in width in time for improved measurement and to separate the neutron signal from the hard photon background which arrives earlier. The FWHM (ns) of the signal relates to the ion temperature by[108]:

$$FWHM = \frac{d\sqrt{T_i}}{v_n} \quad (10)$$

where d is the distance in meters, T_i is the ion temperature in keV, and v_n corresponds to the D-T and D-D reactions (8.2 and 1.3, respectively).

The secondary D-T reactions are also measured, and the yield and spectrum give information related to the z pinch fuel magnetization[109].

The current mapping of the Z NTOF systems[110] are shown in Figure 57, and Table 8 shows the current NTOF distances and configuration. The NTOFs consist of a single EJ-228 or EJ-232 1% quenched plastic scintillator (or Bicron equivalent) coupled to one or two PMTs via Lucite light guides. The single PMT is a Hamamatsu R5946, mod 4 or 5 with an effective (combined PMT-scintillator) impulse response function (IRF) FWHM of about 3.4 - 5.5 ns or 4.1 - 5.5 ns depending on the PMT bias and the Scintillator. A dual PMT NTOF includes a Photek PMT240 that has the capability to gate out the early time hard photon pulse associated typically with the Z load stagnation; and an improved IRF of with a FWHM about 1.8 or 3.2 ns, depending on the Scintillator. An example data set at LOS 270 is given in Figure 59 which shows the x-ray flash, the D-D neutron signal and the D-T neutron signal.

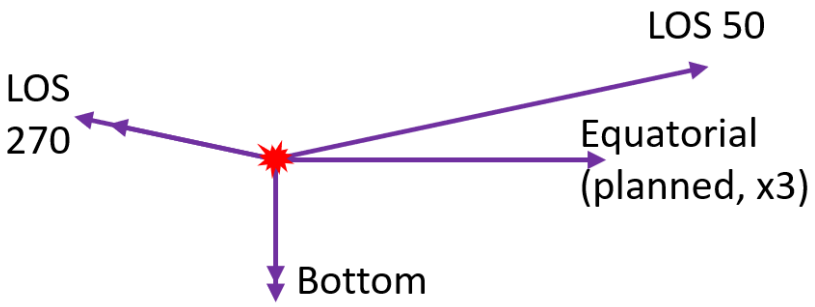

Figure 57. Directions of Z NTOFs. Relative distances are approximately to scale.

The challenges of the environment and mitigation methods include:

- The presence of the early-time hard photon signals preceding or part of the Z-pinch. The best mitigation methods are shielding, collimation, and filtration, gated detectors and maximizing the distance.

- EMI or other noise in the environment which can hide small signals.
- The dynamic range of the signals can be very large. The D-T signals, since they are usually "secondary" reactions in that they use tritium produced by earlier D-D fusion reactions, are ~100X lower than the D-D signals; therefore, it can be difficult to see both signals. The use of added tritium in the Z target improves the D-T signal significantly. For instance, at 0.3% tritium fraction, the DT peak is predicted to be anywhere from 35X to 100X the DD peak depending on the attenuation used. Z has already completed several shots with added tritium.
- Scatter in the environment can add uncertainty to the primary NTOF signals. This is best mitigated by effective collimation and shielding. One of the collimators at LOS 270 is shown in Figure 58 which is usually paired with an in-chamber collimator (not shown). These shields include steel and tungsten to block x-rays and gammas as well as plastic and wax to attenuate scattered neutrons.

Figure 58. LOS 270 NTOF photo of detector shields.

Table 8. Z NTOF configurations.

	Distance (meters)	PMT	Collimation
LOS 50	25.1	Single	No
LOS 270	9.4, 11.4	Single: 9 meters; Double: 11 meters	Yes

Bottom	6.9, 7.9	Single: 7 meters; Double: 8 meters	Yes

New NTOFs are planned in collaboration with Lawrence Livermore National Laboratory to field new detector systems similar to those used at the NIF[111] including four photodetectors viewing a scintillator and a Quartz Cherenkov detector. Three horizontal (0°) LOS's, 120° part, will be constructed in the next few years through the Z water and oil tanks to put detectors at about 18.6 meters from the load. This will allow greater collimation and shielding at those locations since the oil and water are very effective neutron shields. The three horizontal LOS's will help remove ambiguity of the ion temperature associated with plasma motion.

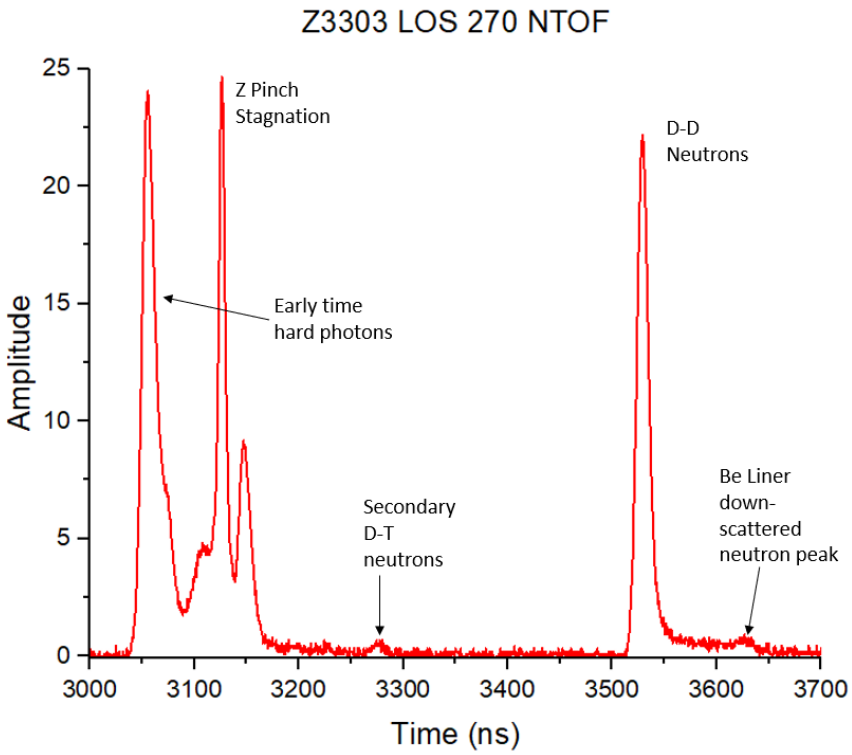

Figure 59. An example NTOF signal of a MagLIF shot with the sources of signals annotated.

3. ODIN

Neutron imaging at the Z-Facility is performed with the one-dimensional imager of neutrons (ODIN) diagnostic[112]. This imager consists of a tungsten rolled edge slit placed near the source which is imaged onto a detector housing located further away. The rolled edge slits are oriented in horizontal plane which results in the imager spatially resolving along the axial direction of the target. The slits are rolled edges with an effective radius of 500 mm. The instrument is typically fielded using a slit spacing of 250 µm, with the slits distance 220mm from the source and the detector housing distance 795mm from the slit. This results in a field-of-view of 10mm with ~500-µm resolution and a magnification of -3.8.

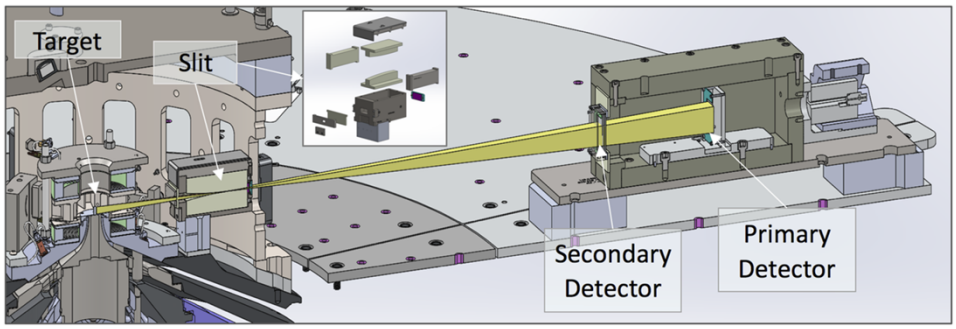

Figure 60. ODIN diagram with beam path in yellow.

Due to the harsh x-ray environment, CR-39 particle track detectors are used. CR-39 is immune to the x-rays present in in the experiment. The CR-39 detectors are passive and collect the time integrated neutron generated signal during the experiment. CR-39 detectors work by energetic charged particles creating latent track in the plastic. Incoming neutrons interact with a proton convertor – a piece of 1mm thick high-density polyethylene (HDPE) film. Neutrons colliding with protons result in ejected protons with an energy related to that of the neutron.

To reveal the tracks, post processing the detector is required. The first step is chemically etching the detector, which enlarges the particle tracks. The second step is scanning the detector, essentially collecting the position, diameter, eccentricity, and contrast of each track. These tracks form the image of the neutron source observed by the instrument.

The environment that ODIN operates not only experiences harsh x-rays, but also is impacted by flying debris and molten metal ('slag') during the experiments. Due to the close proximity of the slit box, it generally takes some level of damage on each shot ranging from metal fragment "bullets" and slag and is ripped off the aperture ring that is connected to before the shot. While the slits survive, the slit housing is a consumable item. The detector housing is further away from the target and get less

damage. There is typically some amount of slag on the front of the detector and the front spacers. Occasionally, the intermediate detector cassette and the front of the detector housing will be damaged by flying debris.

4. GRH

The recent introduction of tritium into MIF experiments on Z will allow for prompt nuclear measurements such as reaction history and gamma bang time. Two nuclear signatures from deuterium and tritium experiments are as follows:

$$D + T \rightarrow 4He + n\ (14.1\ MeV)$$

$$D + T \rightarrow 5He + \gamma\ (16.75\ MeV)$$

The Gamma Reaction History (GRH) system is designed to measure the 16.75 MeV fusion gamma-ray utilizing the Cherenkov radiation principle while the Proton Recoil Telescope (PRT) is designed to measure 14.1 MeV fusion neutrons utilizing neutron-to-proton recoil principle. The harsh environment of x-ray background produced by the Z facility may prevent diagnostic isolation of the 16.75 MeV gamma or 14.1 MeV neutrons. To quantify the impact of x-ray background on reaction history diagnostics, a 3-channel Aerogel Cherenkov Detector (ACD) is currently being fielded.

The GRH measurements are based on the 16.75 MeV γ-ray photon produced through the deuterium + tritium branching ratio with 10^{-5} gammas per DT neutron[113]. This type of diagnostic has been used to measure reaction history and gamma bang time at the OMEGA laser facility and the National Ignition Facility for many years[114,115, 116,117]. The gamma rays produced by the DT reaction in an MIF implosion are converted into relativistic electrons by an aluminum converter via Compton scattering. These electrons travel through the GRH gas cell (CO_2 gas) and create Cherenkov light. This light is then optically relayed to an ultrafast (~3.5 MHz) photomultiplier tuber (PMT)[118] which records the signal of interest. Varying the pressure of the CO_2 gas cell varies the Cherenkov energy threshold and is utilized to isolate the DT gammas.

The GRH from the OMEGA laser facility was installed on Z in September 2020 (see model in Figure 61). The diagnostic was mechanically coupled to the I-beam located along LOS190 at 2.5 meters from target chamber center. The GRH was coupled utilizing liquid actuators designed and fabricated to dampen the shock of the machine. These actuators also act as an alignment tool which allows for pointing of the GRH through in-chamber apertures utilized to reduce unwanted photons from reaching the GRH PMT. Estimated DT gamma signal levels for the GRH are 25 volts for a MagLIF experiment fielded with 50/50 D-T ratio, a square burn width of 2 ns, and a Photek 210 PMT (170 ps rise time) at maximum gain. The x-ray backgrounds at Z are the significant obstacle to overcome for these measurements. For the GRH, initial fielding attempts revealed that high-energy photons were reaching the PMT and creating unwanted signals at levels scaling to ~300-volts for maximum PMT gain. Shielding studies have been ongoing with in-chamber apertures designed and fielded along with local shielding installed to reduce the unwanted signal. To date, the signal has been reduced by an order of magnitude with several efforts still underway to reduce the signal by another order of magnitude. If this signal is significantly reduced, we will be in a good position to isolate the DT spectrum. For instance, we have calculated that a signal of approximately 25 Volts on the GRH when viewing a MagLIF target with a 50/50 D-T mixture though we should mention that facility restrictions do not allow for that fraction at present.

5. ACD

The 3-channel ACD[119,120,121] is fielded along LOS190 at ~6 meters to characterize the background x-ray spectrum produced by Bremsstrahlung radiation during an MIF implosion and neutron-induced secondary x-rays. The ACD uses the same Cherenkov method as the GRH for detecting x-rays except that is utilizes solid glass and aerogel radiators in place of CO2 gas. Glass and aerogels reaching densities as low as ~10 mg/cc are fielded providing threshold energies ranging from 0.3-6.9 MeV. By fielding the ACD on many MagLIF shots, we will attempt to determine the spectrum and endpoint energy (see Reference 121 for example of this process) in an effort to determine the necessary GRH threshold energy for isolating the DT gammas.

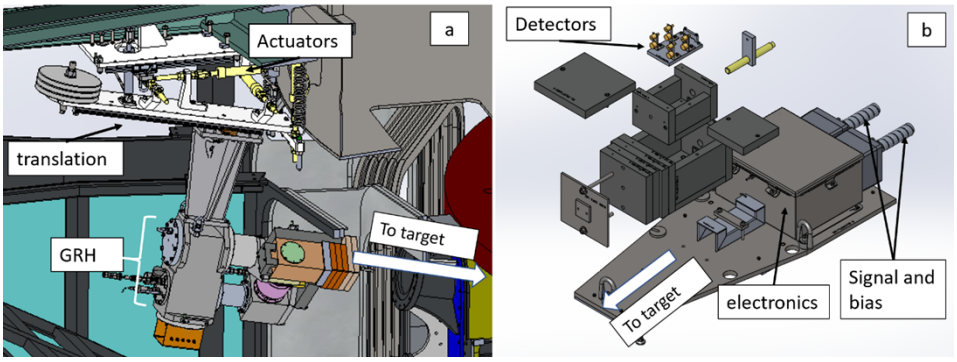

Figure 61. Model of the GRH mechanically coupled to the LOS190 beam. Actuators are utilized to dampen the shock from Z as well as for alignment. B) Model of the PRT test stand with several detectors housed in tungsten to determine background environment.

6. PRT

The proton recoil telescope (PRT) is an application of a nuclear diagnostic method to characterize neutron beams, making use of the scattering interaction of the beam with an inserted target foil. In this application, fusion neutron radiation from Z targets would be collided with a hydrogen-containing material, such as a polyethylene foil, and hydrogen proton recoils are produced in a nearly ideal elastic scattering interaction. The energy of the scattered proton can be related to the energy of the incoming precipitating neutron if the scattering angle θ is known, according to the relationship $E_p = E_n \cos^2 \theta$. If the detector is well calibrated and backgrounds are known or minimized, the PRT could in principle provide a yield measurement, as was done with the PROTEX instrument at OMEGA[122]. In addition, the arrival time of recoil protons at the detector can be related to the neutron birth time and thus the reaction history, subject to 1.) time-of-flight Doppler broadening that occurs in flight from the target to the PRT, and 2.) signal broadening that can occur from different physical geometric path lengths and scattering angles permitted in the system design for the protons to reach the detector (particle

"straggling"). If such a system can be fielded at a physically close location to TCC with minimal straggling, the time resolution that can be achieved by this diagnostic is potentially fast -- semiconductor detectors that can be used have impulse response functions as fast as ~100's of ps, for those with small area and minimal inherent RC time of the semiconductor junction.

The amplitude of the measurement background contribution from X-rays and gammas is expected to be the chief determining factor on the success of the measurement. Efforts to model the background contribution are complicated by a lack of information about the x-ray and gamma emission from Z target at energies greater than 100 keV. If background can be minimized, sensitive measurements could be obtained, diagnosing platforms with yields of 10^{12} or perhaps even lower, with the ability to design for either DD or DT neutrons. A "PRT Testbed" has been designed (Figure 61) and is aimed to be used on shots in Fall 2022. If a successful measurement can be made with ample signal to noise ratio, then the question of time resolution and straggling becomes more pressing, and it will be seen how close to the target the PRT can successfully be fielded. It is ultimately likely that this approach will ultimately not be able to achieve as fast time resolution as approaches based on DT fusion gamma detection, due to the particle straggling effects, although it may be able to achieve high sensitivity and be applicable to DD shots as well as DT.

H. Imaging Detectors

We now discuss more specifically the characteristics of the two-dimensional media used in all of Z's imaging systems and crystal spectroscopy diagnostics. There are two main types of time-integrated detectors, image plates and x-ray film, and two time-resolved ones, UXI (or sometimes referred to as hybrid CMOS or hCMOS) and MCPs. For the most part, the main characteristics of these detectors are consistent wherever they are fielded, but the threats or specific requirements to field these detectors may be location or system specific. Other two-dimensional detectors are used such as streak cameras (time on one axis and one spatial measurement on the other) and CCD cameras or its time-gated version *intensified* CCD cameras, but we leave discussions of these as applicable under the relevant main diagnostic.

1. Image Plates

Image plates (IPs) stores a latent image of the incident x-ray fluence using the principle of optically stimulated luminescence. An older nomenclature for IPs is "storage phosphor", and they have a long history in medical imaging[123]. References 124 and 125 give useful sensitivity and fading profiles of image plates though some differences may exist depending on the image plate scanner. The IPs used at Z are principally comprised of a thin layer (60 μm to 124 μm) of $BaFBr_{0.85}I_{0.15}$:Eu. A fraction (few tens of percent) of the x-ray energy is stored in metastable levels in the forbidden gap of the material. The image is read out by scanning a laser across the plate and recording the light produced by the stimulated release of visible photons produced by the de-trapping of the populated energy levels just mentioned. IPs are designed to be reusable by exposure to visible light though this is not standard practice at Z. As part of a diagnostic-specific cassette, the image plate is protected from room light—which could partially or completely erase the image--via a light-tight (but x-ray "thin") cover such as aluminized Kapton or a thin Be foil. Image plates have a high linear dynamic range (factors of 10^4 to 10^5), can be cut to various sizes, and are somewhat flexible so that they can fit curved geometries when needed. They can even take localized damage—which is not an uncommon occurrence at Z--and still be read out in nearby undamaged areas. The resulting image values-even when linearized--depends on the type of IP,

the scanner used and its settings, and the image fades over time non-linearly. Therefore, a system characterization is necessary for absolute x-ray flux measurements. References 3 and 4 gives some examples. At Z image plate data need not be put on an absolute scale if the image is linear. This allows us to use different scanners with varying settings and even scan the plate multiple times which is often needed when some data is saturated since a single scan only removes a fraction of the latent storage energy fluence. The spatial resolution also varies depending on the plate material and scanner. There have been efforts to characterize the scanners at Z such as the Super Micron IP DITABIS scanner. Figure 64 gives the nominal response curves used at Z. Figure 63 reports the contrast transfer function[126] (CTF) values for the IPs and scanners we use at Z. For consistency, TR image plates are used where the DITABIS scanner[127] has been optimized for the highest resolution. The equivalent LSF FWHM is 52 µm for the TR plate. TR image plates have no protective layer (Figure 62) and a 60 µm thick phosphor layer.

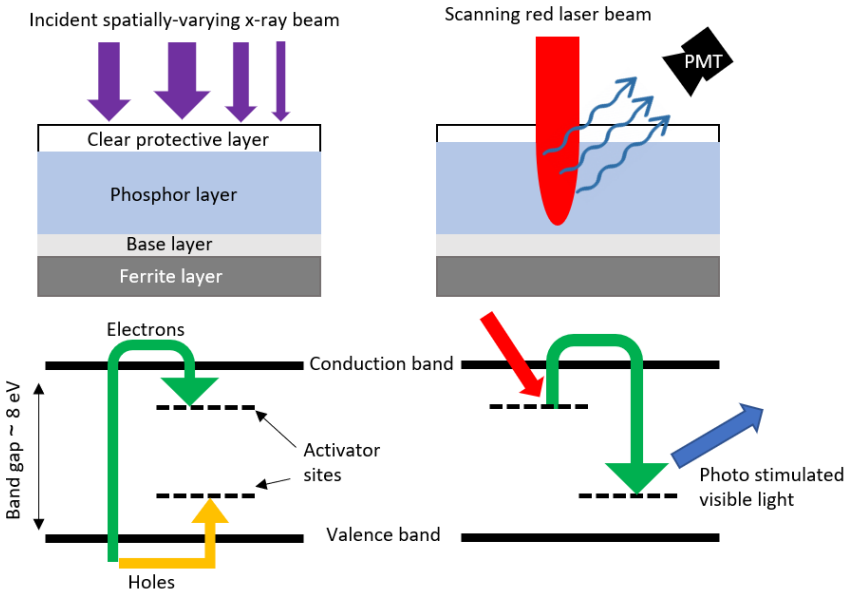

Figure 62. Basic layers of an image plate (not to scale) and method of operation. At bottom is a cartoon of the energy level diagram as excited by x-rays and read out by the scanner.

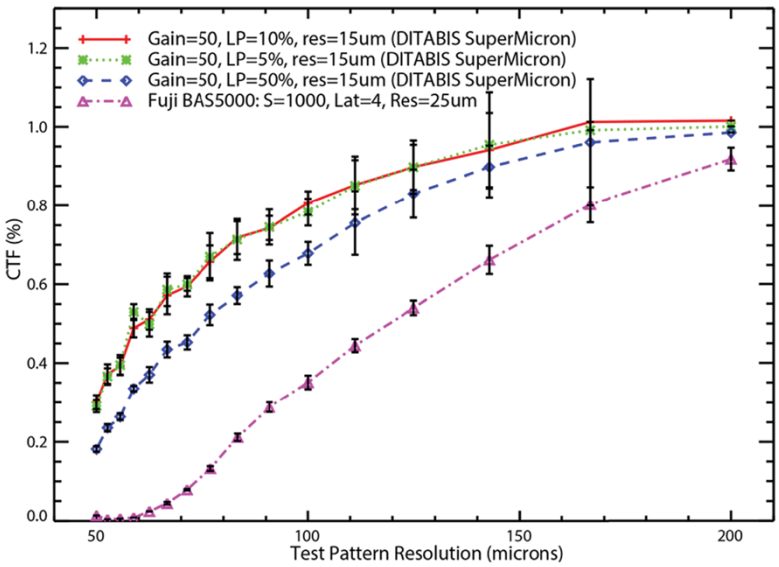

Figure 63. Contrast transfer function of TR image plates used with different scanners and settings at Z[127]. Higher values of CTF indicate higher resolving power at a given resolution which is related to spatial frequency. Reproduced from G. Dunham, *et al.*, "Cross-calibration of Fuji TR image plate and RAR 2492 x-ray film to determine the response of a DITABIS Super Micron image plate scanner", Review of Scientific Instruments 87, 11E301 (2016), with permission from AIP Publishing.

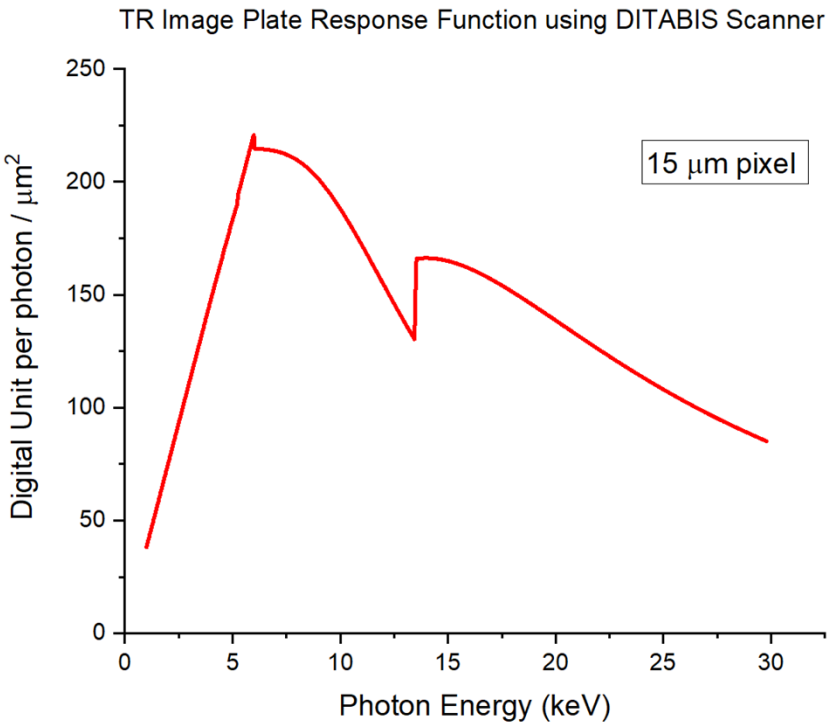

Figure 64. The response function of a TR image plate scanned using the DITABIS scanner at Z.

2. X-ray and Visible Film

We use Kodak TMAX film to record the final image produced by the MCP cameras. In addition, Kodak RAR-2492 x-ray film is used in several spectrometers fielded at Z in low x-ray energy applications (1-10 keV). The film is comprised of a thin overcoat protective layer with a heterogeneous mixture of AgBr grains embedded within the emulsion layer (gelatin). A typical volume fraction of the AgBr grains to emulsion is <20%. For low energy applications (< 10 keV) the AgBr grains are rendered developable after a single photon is absorbed. An example x-ray spectrum obtained from x-ray film deployed in the Axial Package CCP is shown in Figure 65.

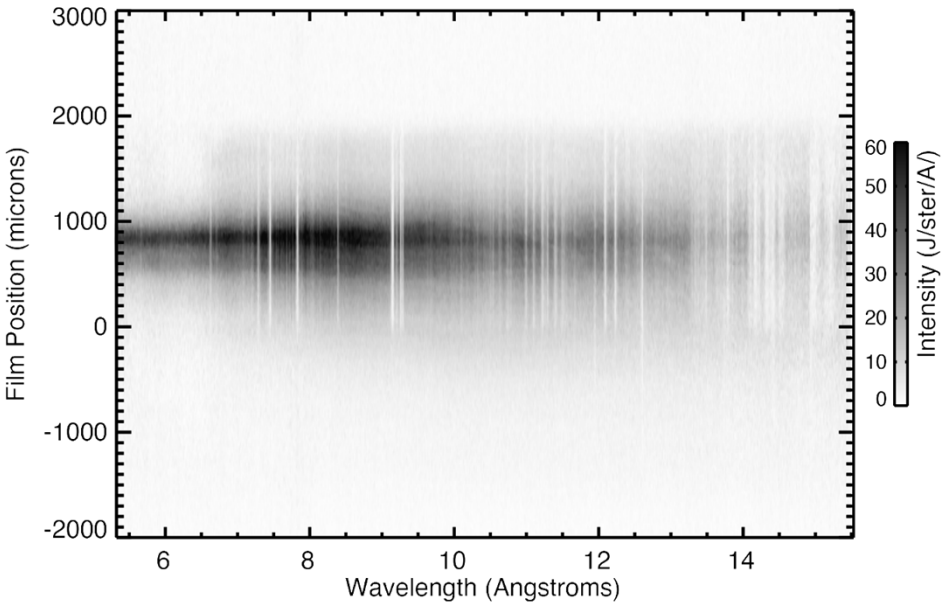

Figure 65. Example x-ray spectra using x-ray film at Z. This was shot Z3469 using a CCP in the Axial Package.

X-ray film is developed using commercial Wyng-Lynch film processors. Film data is scanned on a Perkin-Elmer Microdensitometer using a set of matched numerical optics with a pixel size of 14 μm x 14 μm for x-ray film and 22 μm x 22 μm for visible film. The microdensitometer system is calibrated to produce an image in specular density, $D=\log_{10}(1/\tau)$, where D is the density and τ is the ratio of transmitted to incident light. Digitized x-ray film data is converted from density to intensity utilizing a series of equations determined empirically to fit absolute measurements of exposure. The details of the equations are beyond the scope of this work and are presented in references 128, and 129.

X-ray film is used primarily in the convex crystal PEAs (axial), TIXTL (LOS 130 side-on), and XRS3 instruments on the ZAPP and Opacity experiment campaigns. Figure 65 shows an iron opacity spectrum. The primary advantage of film over image plate is the superior resolution of 5 μm[130]. As film is sensitive to light, all film must be protected in a light-tight film cassette or enclosure. Typically, two layers of filtering are employed to protect against light contamination from pinholes in the filters created during a Z shot. One filter resides in the instrument entrance snout, and another sits over the film. Because the opacity measurements include sub-keV spectra filters must provide high transmission even at low x-ray energies and are therefore extremely thin and fragile. Typical filters are 0.2 μm of Polyimide with a coating of 1500Å and 500Å of aluminum with the thinner Al coating facing the crystal to minimize any material that may ablate off the filter an onto the crystal. Operationally the x-ray film is loaded into each instrument in a dark room. The instruments employ a dark slide to prevent light contamination of the film during transport and experiment setup. The dark slides are opened just before the experiment

occurs and closed again immediately following the experiment prior to any potential exposure to ambient light.

Visible film is used in instruments that convert x-ray emission to visible light through the use of a photocathode and Micro Channel Plate. Kodak TMAX film is used in a variety of film speeds. Visible film is also scanned on the Microdensitometer, but a NIST calibrated step wedge is used to determine the density to exposure correction for further analysis.

The relative sensitivity between x-ray film and image plates depends on the image plate scanner and its settings. For the scan setting used at Z in the DITABIS Super Micron image plate scanner x-ray film is approximately two orders of magnitude more sensitive than image plates. The advantage of film is that it has both higher resolution and greater sensitivity, though film saturates at lower signal levels. Film is also sensitive to light contamination and accumulates background signal from cosmic radiation over time. X-ray film is no longer produced, and all stock expired in 2004 or earlier and therefore has higher than desirable film fog levels effectively reducing the dynamic range of approximate 3.0 OD by ~0.5 OD. One advantage of film over image plates is that once the film is developed it provides an essentially permanent record which can be scanned repeatedly. Image plates are less sensitive to short exposures to ambient light and do not exhibit fogging the way film does. However, the scanning process of image plates is destructive in that signal levels are reduced by ~70% with each scan. Through repeated scans extremely high signal levels can be retrieved from an image plate (each scan has a dynamic range of 10^4-10^5) though signal-to-noise levels decrease with each scan. Image plates continue to be produced and are commercially available though it is not clear how far into the future this will remain the case.

3. UXI

The Ultrafast X-ray Imager (UXI) is the latest development in time-resolved imaging at Z. The details of the construction and performance are detailed in references 131, 132, and 133 with only key details summarized here. The UXI camera consists of hybrid CMOS sensor of which there have been at least four generations with more to come. A diagram of the primary components of the sensor is shown in Figure 66. The UXI camera, an example is shown in Figure 67, also includes on board electronics for biasing, readout, and other functions. Table 9 gives the sensor parameters of the “Icarus” version of the hCMOS sensor used in the current UXI cameras at Z.

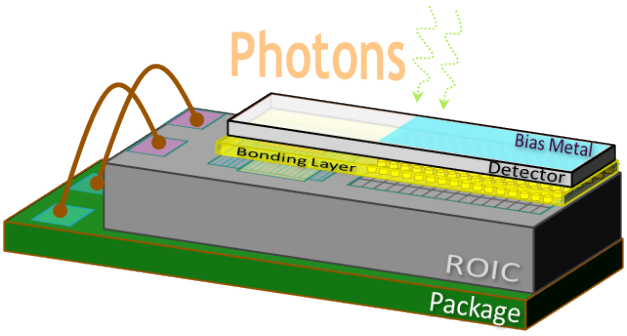

Figure 66. hCMOS sensor as incorporated in the UXI camera.

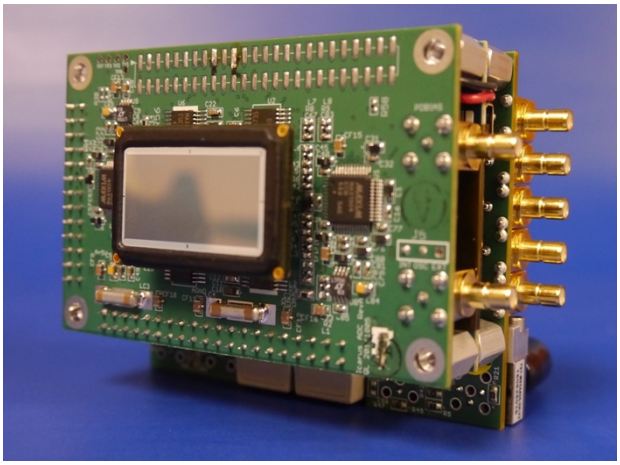

Figure 67. One packaging configuration of a UXI camera containing the sensor and supporting electronics.

Table 9. Current (Icarus) hCMOS sensor parameters of the UXI camera.

Pixel size	25	µm
Array size	1024 x 512	Pixels (two hemispheres)
Number of frames (per hemisphere)	4, 8 total	A hemisphere is 256 x 1024 pixels
Integration time	2 - 38	ns
Interframe time	4 - 40	ns

The x-ray sensitivity is determined by the thickness of the silicon pixel of which the sensor used to date on Z has 25 µm thickness which provides reasonable sensitivity up to 12 keV. Future designs for the hCMOS sensor will include GaAs of similar thickness to the GaAs diodes as used for P&E which will extend the useful sensitive range above 20 keV. Other anticipated improvements include “tiled” sensors where two sensors are abutted on the short edge which will approximately double the available spectral coverage (subject to the spectrometer spatial or spectral limits).

UXI cameras are regularly fielded in

- MONSSTR (spectroscopy, Section IV-C)
- Gated Backlighting (imaging, Section IV-D-5)
- Axial package CCPs (spectroscopy, Section IV-C)

- FOA pinhole cameras (imaging, II-D)

There are several hazards experienced by the UXI cameras in these locations, primarily debris and electromagnetic interference (EMI). Any diagnostic with a LOS to the Z target region will potentially see debris bullets. The diagnostics in the center of the machine (Backlighting and MONSSTR) have been designed to minimize direct exposure of the cameras and so we have yet to see a significant debris bullet in either application. The cameras located further from the load have less inherent debris mitigation and so each application has seen multiple debris bullets over time with baffling adjusted to try and minimize those bullets.

General EMI concerns have driven several design considerations for all applications of UXI at Z. Power is carried along twin-axial cables that have a very high impedance and a low frequency filtering effect, limiting the chance of power disruption due to the relatively high frequency EMI of Z firing. Data transmission, including triggering, is done over fiber with electrical to optical convertors present at either end of the data path. Tests with coaxial transmission of triggers showed heavy disruption of signals. All power and fiber cables are shielded with multiple layers of alternating conductive and insulating shielding, with efforts made to insulate any point where cables would touch metal surfaces of the Z machine.

EMI concerns are greater inside the chamber than outside. Initial attempts at gated radiography experienced significant EMI disruptions requiring modifications to shielding, timing, and firmware. The firmware was changed to allow for latched triggering, where once triggered the electronics would ignore additional, likely spurious, triggers. We also took advantage of the cameras timing features to trigger the camera around 100 ns before the targeted event, imaging in the 3rd frame of 4 and utilizing 40ns interframe times. This caused the camera to be triggered well before any EMI from the machine had a chance to interfere. EMI still has a significant impact on all applications, with control electronics generally beginning to fail after 2 shots in the center of the machine and 5 shots on the outside. Fortunately, the sensors themselves survive significantly more shots, with only 1 sensor so far having failed due to repeated exposure after several years of operation.

4. MCPs

At Z, microchannel-plates (MCPs) are used as x-ray detectors for fast time-gated, multi-frame imaging and spectroscopic diagnostics of high-temperature plasmas. The main elements of the detectors are lead glass MCPs manufactured by Photonis coated with conductive strip lines that carry sub-nanosecond high-voltage pulses to control the timing and the gain. The Z diagnostics use two types of MCPs, with different electrode configurations as shown in Figure 68. Generation 1 (Gen-I) MCPs with low aspect ratio half strips, are used for imaging diagnostics. An x-ray image of the plasma is formed on each strip by a separate pinhole. Generation 2 (Gen-II) MCPs (Fig. 1b), with high aspect ratio full strips, are used primarily for spectroscopic diagnostics. The spectral dispersion is along the long side and there is potential for one-dimensional slit imaging across the strip. Both MCP types have eight strips that can be enabled sequentially by controlling the timing of the bias voltage pulses. Typically, the inter-frame delays are 1 ns, 2 ns, or 3 ns, and the FWHM of the gain pulse are 150 ps, 250 ps, or 800 ps. The pulse amplitude is around -800 V and can be tuned within ±150 V to adjust the gain.

Figure 69 shows the principle of operation and primary components of the MCP cameras. The essential features of an MCP are individual channels (pores)closely packed side by side across the Pb glass plate, each of which acting as a continuous electron multiplier when a negative bias voltage (V_{MCP}) is applied across the plate. The incident x-rays produce photoelectrons that are accelerated by V_{MCP} into the channels. When impacting the channel wall with sufficient energy, they generate secondary electrons and the process repeats, resulting in electron amplification. Within the discrete dynode model[134], the maximum MCP gain can be estimated as $G \propto (V_{MCP})^{L/4d}$ in DC mode. For typical channel diameter $d \approx 10$ µm and plate thickness $L \approx 460$ µm[134, 135], $G \propto (V_{MCP})^{11.5}$ in DC, but $G \propto (V_{MCP,\,peak})^{17}$ in pulse mode[136]. The exponent decreases for higher energy photons because of the absorption cross section dependence on energy[135].

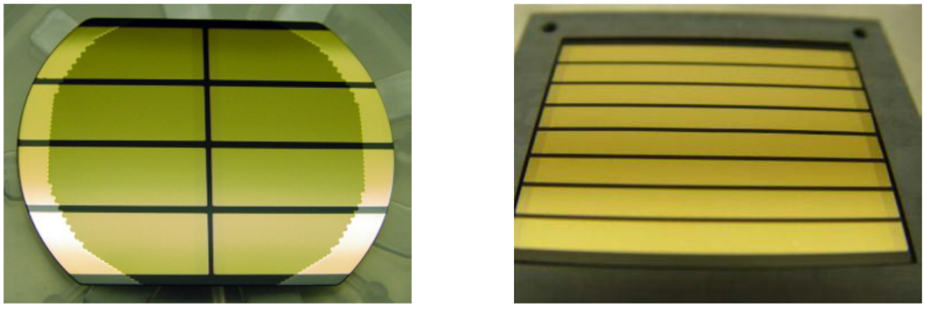

Figure 68. Left: Gen-I MCP configuration with 8 half strips, used for imaging diagnostics. Right: Gen-II MCP with 8 full strips, developed for spectroscopic diagnostics. The back side of each MCP is coated uniformly and serves as ground electrode.

After the MCP amplification, the electrons are accelerated by a positive bias voltage ($V_{ph} \sim 2500$ V) onto a phosphor that emits visible light upon impact. The phosphor is coated onto a fiber optic faceplate and the visible light is collected on film or CCD camera. The image space resolution is dominated by the electron spread during transit and is well approximated[135] by $(V_{ph})^{-1/2}$. The phosphor bias is typically applied as a high voltage pulse to avoid potential arcing after Z-shots.

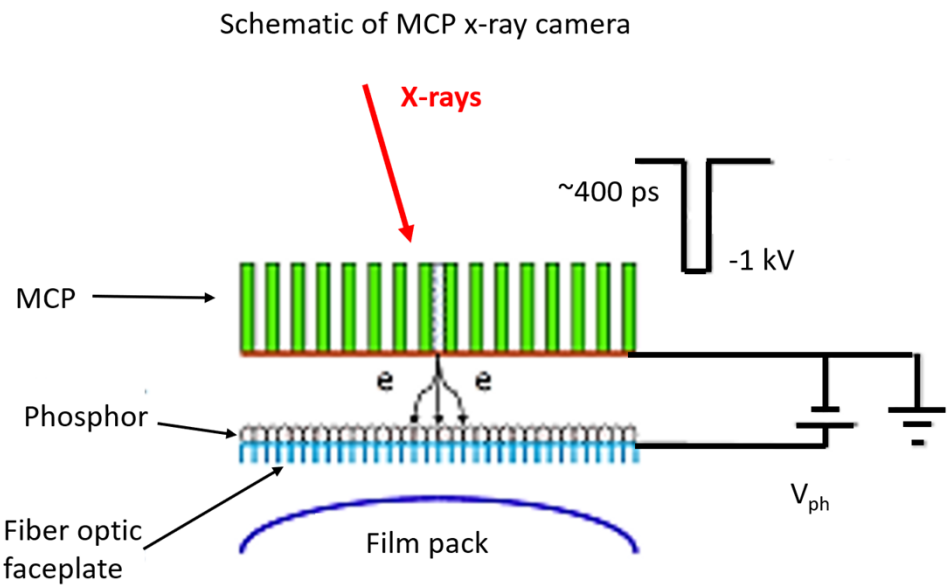

Figure 69. Schematic of high-speed time gated MCP based x-ray detector. MCP is biased by a negative voltage while the phosphor is biased by a positive voltage.

Generally, the MCP response decreases as the x-ray energy increases. For energy below 5 keV, the x-rays interact only with the walls of the first channel they encounter, and the response decreases by a factor ~50 from 250 eV to 5 keV[134]. X-ray penetration through multiple MCP pore walls is increasingly important above 5 keV[137], and the MCP response continues to decrease for increasing energy between 6 and 20 keV by a factor ~7 (reference 135). In addition, the MCP response sensitivity to the bias voltage decreases with increasing x-ray energy[136]. For example, at 15 keV, the dynamic range is about 2000 with the MCP biased at 650 VDC and is reduced to about 260 when the bias is set at 850 VDC[135].

The space resolution of the MCP detector is inversely proportional to the square root of the phosphor bias voltage and is ~45 µm at V_{ph} = 3000 V, independent of the incident x-ray energy from 6 to 20 keV and of the incident x-ray flux, from linear to saturated output[135]. However, the space resolution depends on the incidence angle and increases by ~20 µm from normal incidence to 15° at 15 keV.

Simulation studies[136] of MCPs gated with a sub-nanosecond voltage pulse showed that the optical gate profile width increases as the x-ray energy is increased above 5 keV, a consequence of increased x-ray penetration at energies >5 keV. For example, for a 150 ps flat top pulse, the FWHM of the gate profile increases from ~160 ps for E < 5 keV to ~180 ps at 25 keV, an ~12.5% increase. The effect of pulsing is exacerbated for the half strips of the Gen-I configuration: impedance mismatches cause reflections and losses along the strip lines that can have a significant impact on the position-dependent amplitude and pulse width of the gain because of the high exponent of the gain dependence[138] on V_{MCP}. Electrical probe

measurements showed that the sensitivity of the half-strip MCP in pulsed mode decreases by ~25% and the FWHM of gate profiles increases by ~30% between the end of the strip and the beginning of the strip[139]. To mitigate these effects, the Gen-II cameras use full strips and impedance-matched transmission lines.

Fielding MCP detectors on Z has specific challenges. The hard x-ray background can penetrate through all layers of the detector and form time-integrated images directly onto the film, which overlap with the intended time-gated images. The MCPs are intended for operation in high vacuum. Exposure to the Z environment, containing water, oil, and load material vapors extends the time it takes to bring MCP detectors within operational parameters pre-shot. Insufficient vacuum can lead to MCP detector damage when the pulsed high voltages are applied during the shot. The shot-related acceleration can occasionally lead to loss of electrical contacts internal to the MCP detectors.

All MCP detectors used for Z diagnostics are routinely characterized using a Manson x-ray source by comparing their response to that of calibrated Si diodes. Their main characteristics have been determined by measurements with synchrotron x-rays[134,135], short-pulse UV laser light[139], and high-impedance electrical probes[138,139], and modeling with Monte Carlo simulations[137,136,140,141] validated by these measurements.

V. Conclusion and Outlook

We conclude by summarizing the list and purposes of diagnostics commonly fielded for each type of load: dynamic material properties (DMP), magneto-inertial fusion (MIF), radiation sciences (RS), and Power Flow (PF). Table 10 is a basic listing of diagnostics associated with these load types.

Table 10. List of diagnostics commonly used on the four general load types: radiation sciences (RS), magnetized inertial fusion (MIF), dynamic material properties (DMP), and power flow (PF). "FS experiments" refer to fundamental science activities using RS type loads but are not described in detail in this report.

Load type	Diagnostic	Primary Purposes
All	Pulsed power diagnostics	Current delivery
	Load current B-dots, IDLTs	Load current
RS	Axial Package spectrometers	Opacity measurements
	P&E	Source power and energy
	X-ray spectrometers	Source spectra
		FS experiments
	PDV	FS experiments
	PDI	Thermo-mechanical shock of driven samples
MIF	P&E	Stagnation timing
	X-ray spectroscopy (TREX, CRITR)	Source spectra, mix
	X-ray imaging (TIPC, MLM)	Stagnation shape

	PDV / VISAR	Load current
	NTOF	Neutron spectra / bang time / fuel magnetization
	Activation samples	Neutron yield
	GRH / PRT	Neutron burn history
DMP	PDV / VISAR	Load current and sample EOS
	X-ray Diffraction	Sample phase transitions
PF	SVS	MITL plasma density and temperature
	SEGOI	MITL plasma velocity
	MiniXRDs	Cathode temperature
	FCAPs	Current loss to anode in convolute
	PDV/VISAR	Load current
	CIDZ	Cathode current loss (currently in convolute)
	APDs	Plasma velocity

The source terms of the harsh environment are only partially understood and quantified, but the diagnostics themselves are mini-laboratories in developing techniques on operating in face of the various backgrounds, noise, and other "threats" which affect the data or diagnostic operation negatively in some way. Diagnostics in-chamber are subject to debris of various sizes and composition depending on the load type and distances. MIF targets tend to produce the highest amount and largest sizes of debris, mainly because mass of the targets is higher, especially if magnetic field coils are used. RS targets—usually by design--produce the highest flux of x-rays from the target Z pinch but usually produce the least amount of debris. Loads with high inductances and current loss likely produce the highest flux of hard x-rays which may occur at a different time (usually earlier) than peak current or load implosion. External detectors such as the GRH and NTOFs observe these backgrounds which may affect their data. Detectors in-chamber are always inside thick-walled enclosures usually with a minimum of one-inch of tungsten, at least in the direction of the load. Outside of the blast shield, these systems are usually reusable with modest refurbishment. Electromagnetic interference (EMI) is present at varying levels throughout the facility which may be caused by pulsed power components as or after they fire or from other sources, but we can usually reduce the amplitude of EMI to < 50 mV through careful cable routing and installation.

We continue to develop and expand the Z diagnostic capability. The Ultrafast X-ray Imager (UXI) is a key component with which we are converting diagnostics which had only been previously time-integrated into time-resolved; XRS3 and MONSSTR are an example. Time resolved measurements not only provide key physics insights but allow the measurement to avoid some x-ray backgrounds that occur at a different time. We are working to incorporate x-ray streak cameras[142] into the diagnostic boats to provide time resolution down to tens of picoseconds for spectroscopy or power and energy measurements. Power flow measurements continue to increase in sensitivity and precision. Improved B-dot probes near the load provide more accurate and longer-lasting measurement of current delivery.

We plan on expanding gated and streaked visible spectroscopy to the UV range which will improve understanding of plasma conditions in the inner MITL. Additional visible and plasma imaging techniques are being developed such as laser shadowgraphy[143]. We are implementing improvements to the x-ray power and energy diagnostic suite to reliably have < 10% uncertainty. IR pyrometry[144] has been implemented on DMP experiments to measure heating of compressed samples and is being considered for measuring the time-resolved temperature of x-ray heated samples. These are just a few examples of a constant effort to expand and improve the Z diagnostic suite. In short, we must keep up with the physics demands associated with the increasing complexity of the Z experiments and applications.

Acknowledgments

Part of this work was supported by Mission Support and Test Services, LLC, under Contract No. DE-NA0003624 with the U.S. Department of Energy. DOE/NV/03624—1528. Los Alamos National Laboratory is operated by Triad National Security, LLC, for the National Nuclear Security Administration of U.S. Department of Energy under Contract No. 89233218CNA000001. Sandia National Laboratories is a multimission laboratory managed and operated by National Technology and Engineering Solutions of Sandia LLC, a wholly owned subsidiary of Honeywell International Inc. for the U.S. Department of Energy's National Nuclear Security Administration under Contract No. DE-NA0003525.

This paper reviews objective technical results and analysis. Any subjective views or opinions that might be expressed do not necessarily represent the views of the U.S. Department of Energy or the U.S. Government.

AUTHOR DECLARATIONS

Conflict of Interest

The authors have no conflicts to disclose.

Data Availability

The data that support the findings of this review are available from the corresponding authors upon reasonable request except where the data is in external references as noted.

References

[1] D. Sinars et al., Phys. Plasmas 27, 070501 (2020); https://doi.org/10.1063/5.0007476.
[2] M. E. Savage, L. F. Bennett, D. E. Bliss, W. T. Clark, R. S. Coats, J. M. Elizondo, K. R. LeChien, H. C. Harjes, J. M. Lehr, J. E. Maenchen et al., "An overview of pulsed compression and power flow in the upgraded Z pulsed power driver," in 16th IEEE International Pulsed Power Conference (2007), Vol. 2, pp. 979–984.
[3] T. J. Nash, M. S. Derzon, G. A. Chandler, D. L. Fehl, R. J. Leeper, J. L. Porter, R. B. Spielman, C. Ruiz, G. Cooper, J. McGurn, M. Hurst, D. Jobe, J. Torres, J. Seaman, K. Struve, S. Lazier, T. Gilliland, L. A. Ruggles, W. A. Simpson, R. Adams, J. A. Seaman, D. Wenger, D. Nielsen, P. Riley, R. French, B. Stygar, T. Wagoner, T. W. L. Sanford, R. Mock, J. Asay, C. Hall, M. Knudson, J. Armijo, J. McKenney, R. Hawn, D. Schroen-Carey, D. Hebron, T. Cutler, S. Dropinski, C. Deeney, P. D. LePell, C. A. Coverdale, M. Douglas, M. Cuneo, D. Hanson, J. E. Bailey, P. Lake, A. Carlson, C.

Wakefield, J. Mills, J. Slopek, and T. Dinwoodie, G. Idzorek, "Diagnostics on Z (invited)", Review of Scientific Instruments 72, 1167-1172 (2001), https://doi.org/10.1063/1.1322618.

[4] Hanson, David Lester. 2003. "Diagnostics development plan for ZR.". United States. https://doi.org/10.2172/918272. https://www.osti.gov/servlets/purl/918272.

[5] J. R. Asay, L. C. Chhabildas, R. Jeffery Lawrence, and M. A. Sweeney, Impactful Times: Memories of 60 Years of Shock Wave Research at Sandia National Laboratories (Springer, Cham, Switzerland, 2017).

[6] A. J. Porwitzky, C. T. Seagle, and B. J. Jensen, "Zero to 1,600 m/s in 40 microns: Sensitive pulse shaping for materials characterization on Z," Proc. Eng. 204, 337 (2017).

[7] G. A. Rochau, J. E. Bailey, R. E. Falcon, G. P. Loisel, T. Nagayama, R. C. Mancini, I. Hall, D. E. Winget, M. H. Montgomery, and D. A. Liedahl, "ZAPP: The Z Astrophysical Plasma Properties collaboration," Phys. Plasmas 21, 056308 (2014).

[8] Bailey, James E. 2018. "Benchmark experiments for the radiative properties of astrophysical plasmas," United States. https://www.osti.gov/servlets/purl/1592605.

[9] R. G. Kraus, S. Root, R. W. Lemke, S. T. Stewart, S. B. Jacobsen, and T. R. Mattsson, "Impact vaporization of planetesimal cores in the late stages of planet formation," Nat. Geosci. 8, 269 (2015).

[10] Laity, George Russell, Aragon, Carlos, Bennett, Nichelle Lee, Bliss, David E., Dolan, Daniel H.,, Fierro, Andrew S., Gomez, Matthew R, Hess, Mark Harry, Hutsel, Brian Thomas, Jennings, Christopher Ashley, Johnston, Mark D., Kossow, Michael Richard, Lamppa, Derek C., Martin, Matthew, Patel, Sonal, Porwitzky, Andrew James, Robinson, Allen C., Rose, David Vincent, VanDevender, Pace, Waisman, Eduardo Mario, Webb, Timothy Jay, Welch, Dale Robert, Rochau, Gregory A., Savage, Mark E., Stygar, William, White, William Michael, Sinars, Daniel, and Cuneo, Michael Edward. 2018. "Recent Diagnostic Platform Accomplishments for Studying Vacuum Power Flow Physics at the Sandia Z Accelerator." United States. https://www.osti.gov/servlets/purl/1592228.

[11] S. A. Slutz, M. C. Herrmann, R. A. Vesey, A. B. Sefkow, D. B. Sinars, D. C. Rovang, K. J. Peterson, and M. E. Cuneo, "Pulsed-power-driven cylindrical liner implosions of laser preheated fuel magnetized with an axial field," Phys. Plasmas 17, 056303 (2010).

[12] S. A. Slutz, M. R. Gomez, S. B. Hansen, E. C. Harding, B. T. Hutsel, P. F. Knapp, D. C. Lamppa, T. J. Awe, D. J. Ampleford, D. E. Bliss, G. A. Chandler, M. E. Cuneo, M. Geissel, M. E. Glinsky, A. J. Harvey-Thompson, M. H. Hess, C. A. Jennings, B. Jones, G. R. Laity, M. R. Martin, K. J. Peterson, J. L. Porter, P. K. Rambo, G. A. Rochau, C. L. Ruiz, M. E. Savage, J. Schwarz, P. F. Schmit, G. Shipley, D. B. Sinars, I. C. Smith, R. A. Vesey, and M. R. Weis , "Enhancing performance of magnetized liner inertial fusion at the Z facility", Physics of Plasmas 25, 112706 (2018) https://doi.org/10.1063/1.5054317.

[13] D.A. Yager-Elorriaga et al. "An overview of magneto-inertial fusion on the Z machine at Sandia National Laboratories," (2022) Nucl. Fusion 62 042015. https://doi.org/10.1088/1741-4326/ac2dbe.

[14] J. E. Bailey, G. A. Rochau, R. C. Mancini, C. A. Iglesias, J. J. MacFarlane, I. E. Golovkin, C. Blancard, P. Cosse, and G. Faussurier, "Experimental investigation of opacity models for stellar interior, inertial fusion, and high energy density plasmas," Phys. Plasmas 16, 058101 (2009).

[15] J. E. Bailey, T. Nagayama, G. P. Loisel, G. A. Rochau, C. Blancard, J. Colgan, P. Cosse, G. Faussurier, C. J. Fontes, F. Gilleron et al., "A higher-than-predicted measurement of iron opacity at solar interior temperatures," Nature 517, 56 (2015).

[16] A. J. Harvey-Thompson, C. A. Jennings, B. Jones, J. P. Apruzese, D. J. Ampleford, D. C. Lamppa, C. A. Coverdale, M. E. Cuneo, J. L. Giuliani, S. B. Hansen et al., "Investigating the effect of adding an on-axis jet to Ar gas puff z pinches on Z," Phys. Plasmas 23, 101203 (2016).

[17] J. L. Guiliani and R. J. Commisso, "A review of the gas-puff z-pinch as an x-ray and neutron source," IEEE Trans. Plasma Sci. 43, 2385 (2015).

[18] T. J. Nash, M. S. Derzon, G. A. Chandler, R. Leeper, D. Fehl, J. Lash, C. Ruiz, Cooper, J. F. Seaman, J. McGurn et al., "High-temperature dynamic hohlraums on the pulsed power driver Z," Phys. Plasmas 6, 2023 (1999).

[19] T. W. L. Sanford, R. E. Olson, R. L. Bowers, G. A. Chandler, M. S. Derzon, D. E. Hebron, R. J. Leeper, R. C. Mock, T. J. Nash, D. L. Peterson, L. E. Ruggles, W. W. Simpson, K. W. Struve, and R. A. Vesey, "Z-pinch-generated x-rays demonstrate potential for indirect-drive ICF experiments," Phys. Rev. Lett. 83, 5511 (1999).

[20] D.J. Ampleford et al., Physics of Plasmas 21, 056708 (2014)

[21] Ampleford, David, Hansen, Stephanie B., Jennings, Christopher Ashley, Webb, Timothy Jay, Harper-Slaboszewicz, V., Loisel, Guillaume Pascal, Flanagan, Timothy McGuire, Bell, Kate Suzanne, Jones, Brent M., McPherson, Leroy A., Rochau, Gregory A., Chittenden, Jeremy P., Sherlock, Mark, Appelbe, Brian, Giuliani, John, Ouart, Nicholas, and Seely, John. 2015. "Non-thermal x-ray emission from wire array z-pinches". United States. https://doi.org/10.2172/1227914. https://www.osti.gov/servlets/purl/1227914.

[22] C. A. Jennings, M. E. Cuneo, E. M. Waisman, D. B. Sinars, D. J. Ampleford, G. R. Bennett, W. A. Stygar, and J. P. Chittenden, "Simulations of the implosion and stagnation of compact wire arrays", Physics of Plasmas 17, 092703 (2010) https://doi.org/10.1063/1.3474947

[23] Ball, Christopher Robert, Ulmen, Benjamin A, Cap, Jerome S., Maurer, Andrew, Sullivan, Michael Alex, Spencer, Decker Charles, Johnson, Drew, & Bourdon, Christopher. Advancing Engineering Diagnostics: Measuring and Analyzing Pulsed Power Mechanical Environments. United States.

[24] Yager-Elorriaga, David, Montoya, Michael, Bliss, David, Ball, Christopher, Atencio, Phillip, Carpenter, Brian, Fuerschbach, Kyle, Fulford, Karin, Lamppa, Derek, Lowinske, Michael, Lucero, Larry, Patel, Sonal, Romero, Anthony, Tanbakuchi, Anthony, and Breznik-Young, Bonnie. 2021. "Optical Imaging on Z LDRD: Design and Development of Self-Emission and Debris Imagers.". United States. https://doi.org/10.2172/1824937. https://www.osti.gov/servlets/purl/1824937.

[25] M. R. Gomez, G. A. Rochau, J. E. Bailey, G. S. Dunham, M. D. Kernaghan, P. Gard, G. K. Robertson, A. C. Owen, J. W. Argo, D. S. Nielsen, and P. W. Lake, "Pinned, optically aligned diagnostic dock for use on the Z facility", Review of Scientific Instruments 83, 10D714 (2012) https://doi.org/10.1063/1.4732848.

[26] P. Rambo, J. Schwarz, M. Schollmeier, M. Geissel, I. Smith, M. Kimmel, C. Speas, J. Shores, D. Armstrong, J. Bellum, E. Field, D. Kletecka, and J. Porter, "Sandia's Z-backlighter laser facility," Proc. SPIE 10014, 100140Z (2016).

[27] M. R. Weis, A. J. Harvey-Thompson, and D. E. Ruiz, "Scaling laser preheat for MagLIF with the Z-Beamlet laser", Physics of Plasmas 28, 012705 (2021) https://doi.org/10.1063/5.0029850.

[28] V. J. Harper-Slaboszewicz, B. A. Ulmen, C. T. Parzyck, D. J. Ampleford, A. L. McCourt, K. S. Bell, and C. A. Coverdale, "Coarse spectral characterization of warm x-rays at the Z facility using a filtered thermoluminescent dosimeter array", Review of Scientific Instruments 88, 043501 (2017) https://doi.org/10.1063/1.4979626

[29] Colombo, Anthony P., Edens, Aaron, Looker, Quinn Michael, Stahoviak, John W., Kimmel, Mark W., Loisel, Guillaume Pascal, Bailey, James E., Dunham, Greg S, Gard, Paul D, Kellogg, Jeffrey W., and Porter, John L. 2020. "Ultrafast X-ray Imager spectrometers for time-resolved spectroscopy on Z.". United States. https://doi.org/10.2172/1834697. https://www.osti.gov/servlets/purl/1834697.

[30] H. Fransplass, M. Langseth, O.S. Hopperstad, "Tensile behaviour of threaded steel fasteners at elevated rates of strain," International Journal of Mechanical Sciences, Volume 53, Issue 11, 2011, Pages 946-957, ISSN 0020-7403, https://doi.org/10.1016/j.ijmecsci.2011.07.006.

[31] M. E. Savage et al., "An overview of pulse compression and power flow in the upgraded Z pulsed power driver," 2007 16th IEEE International Pulsed Power Conference, 2007, pp. 979-984, doi: 10.1109/PPPS.2007.4652354.

[32] T. C. Wagoner et al. "Differential-output B-dot and D-dot monitors for current and voltage measurements on a 20-MA, 3-MV pulsed-power accelerator," Phys. Rev. ST Accel. Beams 11, 100401, 22 October 2008. https://doi.org/10.1103/PhysRevSTAB.11.100401.

[33] M. C. Jones, D. J. Ampleford, M. E. Cuneo, R. Hohlfelder, C. A. Jennings, D. W. Johnson, B. Jones, M. R. Lopez, J. MacArthur, J. A. Mills, T. Preston, G. A. Rochau, M. Savage, D. Spencer, D. B. Sinars, and J. L. Porter, "X-ray power and yield measurements at the refurbished Z machine", Review of Scientific Instruments 85, 083501 (2014) https://doi.org/10.1063/1.4891316.

[34] D. L. Fehl, F. Biggs, G. A. Chandler, and W. A. Stygar, "Spectral resolution for a five-element, filtered, x-ray detector array using the method of Backus and Gilbert", Review of Scientific Instruments 71, 3072-3079 (2000) https://doi.org/10.1063/1.1304869.

[35] K. S. Bell et al., "The differential absorption hard x-ray spectrometer at the Z facility," in IEEE Transactions on Plasma Science, vol. 45, no. 8, pp. 2393-2398, Aug. 2017, doi: 10.1109/TPS.2017.2723347.

[36] R. J. Tapper. "Diamond detectors in particle physics" (2000) Rep. Prog. Phys. 63 1273.

[37] D. D. Bloomquist et al., "Saturn: A large area X-ray simulation accelerator," in Proc. 6th IEEE Pulsed Power Conf., Arlington, VA, USA, Jun. 1987, p. 310.

[38] R. B. Spielman, W. W. Hsing, and D. L. Hanson, "Photoconducting x-ray detectors for Z-pinch experiments", Review of Scientific Instruments 59, 1804-1806 (1988) https://doi.org/10.1063/1.1140118
[39] D. R. Kania, L. Pan, H. Kornblum, P. Bell, O. N. Landen, and P. Pianetta, "Soft x-ray detection with diamond photoconductive detectors", Review of Scientific Instruments 61, 2765-2767 (1990) https://doi.org/10.1063/1.1141824.
[40] Quinn Looker, Michael G. Wood, Antonino Miceli, Madan Niraula, Kazuhito Yasuda, and John L. Porter, "Synchrotron characterization of high-Z, current-mode x-ray detectors", Review of Scientific Instruments 91, 023509 (2020) https://doi.org/10.1063/1.5139403
[41] Opto Diode, 1260 Calle Suerte, Camarillo, California 93012. [Discontinued product] Datasheet: https://www.digikey.com/en/products/detail/opto-diode-corp/AXUVHS11/3782856
[42] Quinn Looker, Michael G. Wood, Patrick W. Lake, Jin K. Kim, and Darwin K. Serkland, "GaAs x-ray detectors with sub-nanosecond temporal response", Review of Scientific Instruments 90, 113505 (2019) https://doi.org/10.1063/1.5127294
[43] H. C. Ives et al. "Measurement of the energy and power radiated by a pulsed blackbody x-ray source." Phys. Rev. ST Accel. Beams 9, 110401 – Published 8 November 2006.
[44] G. A. Chandler, C. Deeney, M. Cuneo, D. L. Fehl, J. S. McGurn, R. B. Spielman, and J. A. Torres, J. L. McKenney, J. Mills, K. W. Struve. "Filtered x-ray diode diagnostics fielded on the Z accelerator for source power measurements", Review of Scientific Instruments 70, 561-565 (1999) https://doi.org/10.1063/1.1149355.
[45] Stanford Synchrotron Radiation Lightsource, Beamline 16-2, https://www-ssrl.slac.stanford.edu/content/beam-lines/by-the-number.
[46] R. B. Spielman, C. Deeney, D. L. Fehl, D. L. Hanson, N. R. Keltner, J. S. McGurn, and J. L. McKenney, "Fast resistive bolometry", Review of Scientific Instruments 70, 651-655 (1999) https://doi.org/10.1063/1.1149488
[47] P. W. Lake, J. E. Bailey, G. A. Rochau, P. Gard, D. Petmecky, M. Bump, N. R. Joseph, T. C. Moore, and L. B. Nielsen-Weber, "Twin-elliptical-crystal time- and space-resolved soft x-ray spectrometer", Review of Scientific Instruments 77, 10F315 (2006) https://doi.org/10.1063/1.2227444.
[48] E. O. Baronova, M. M. Stepanenko, N. R. Pereira, "Cauchois–Johansson x-ray spectrograph for 1.5–400 keV energy range", Review of Scientific Instruments 72, 1416-1420 (2001) https://doi.org/10.1063/1.1324754.
[49] D. B. Sinars, D. F. Wenger, S. A. Pikuz, B. Jones, M. Geissel et al. "Compact, rugged in-chamber transmission spectrometers (7–28 keV) for the Sandia Z facility" Rev. Sci. Instrum. 82, 063113 (2011); doi: 10.1063/1.3600610.
[50] E. C. Harding, T. Ao, J. E. Bailey, G. Loisel, D. B. Sinars, M. Geissel, G. A. Rochau, and I. C. Smith, "Analysis and implementation of a space resolving spherical crystal spectrometer for x-ray Thomson scattering experiments", Review of Scientific Instruments 86, 043504 (2015) https://doi.org/10.1063/1.4918619
[51] P. F. Knapp, C. Ball, K. Austin, S. B. Hansen, M. D. Kernaghan, P. W. Lake, D. J. Ampleford, L. A. McPherson, D. Sandoval, P. Gard, M. Wu, C. Bourdon, G. A. Rochau, R. D. McBride, and D. B. Sinars, "A new time and space resolved transmission spectrometer for research in inertial confinement fusion and radiation source development", Review of Scientific Instruments 88, 013504 (2017) https://doi.org/10.1063/1.4973914
[52] J. R. Fein, D. J. Ampleford, J. K. Vogel, B. Kozioziemski, C. C. Walton, M. Wu, C. R. Ball, A. Ames, J. Ayers, P. Bell, C. J. Bourdon, D. Bradley, R. Bruni, G. S. Dunham, P. D. Gard, D. Johnson, K. Kilaru, C. Kirtley, P. W. Lake, A. Maurer, L. Nielsen-Weber, L. A. Pickworth, M. J. Pivovaroff, B. Ramsey, O. J. Roberts, G. A. Rochau, S. Romaine, and M. Sullivan , "A Wolter imager on the Z machine to diagnose warm x-ray sources", Review of Scientific Instruments 89, 10G115 (2018) https://doi.org/10.1063/1.5038347.
[53] B. A. Arnold et al. "A modified pinhole camera method for investigation of x-ray tube focal spots," 1973 Phys. Med. Biol. 18 540. https://doi.org/10.1088/0031-9155/18/4/006.
[54] B. Jones, C. Deeney, A. Pirela, C. Meyer, D. Petmecky, P. Gard, R. Clark and J. Davis, "Design of a multilayer mirror monochromatic x-ray imager for the *Z* accelerator", Review of Scientific Instruments 75, 4029-4032 (2004) https://doi.org/10.1063/1.1789257
[55] Marius S. Schollmeier, Matthias Geissel, Jonathon E. Shores, Ian C. Smith, and John L. Porter, "Performance of bent-crystal x-ray microscopes for high energy density physics research," Appl. Opt. 54, 5147-5161 (2015). https://doi.org/10.1364/AO.54.005147.
[56] B. Jones, C. A. Coverdale, D. S. Nielsen, M. C. Jones, C. Deeney, J. D. Serrano, L. B. Nielsen-Weber, C. J. Meyer, J. P. Apruzese, R. W. Clark, and P. L. Coleman, "Multicolor, time-gated, soft x-ray pinhole imaging of wire array and

gas puff Z pinches on the Z and Saturn pulsed power generators", Review of Scientific Instruments 79, 10E906 (2008) https://doi.org/10.1063/1.2969280

[57] B. Jones, C. Deeney, A. Pirela, C. Meyer, D. Petmecky, P. Gard, R. Clark, J. Davis, "Design of a multilayer mirror monochromatic x-ray imager for the *Z* accelerator", Review of Scientific Instruments 75, 4029-4032 (2004) https://doi.org/10.1063/1.1789257

[58] L. Armon McPherson, David J. Ampleford, Christine A. Coverdale, Jeffrey W. Argo, Albert C. Owen, and Deanna M. Jaramillo, "High energy X-ray pinhole imaging at the Z facility", Review of Scientific Instruments 87, 063502 (2016) https://doi.org/10.1063/1.4953004

[59] Timothy J. Webb, David Ampleford, Christopher R. Ball, Matthew R. Gomez, Patrick W. Lake, Andrew Maurer, and Radu Presura, "A time-resolved, in-chamber x-ray pinhole imager for Z", Review of Scientific Instruments 92, 033512 (2021) https://doi.org/10.1063/5.0040706

[60] G. R. Bennett, O. L. Landen, R. F. Adams, J. L. Porter, L. E. Ruggles, W. W. Simpson, and C. Wakefield, "X-ray imaging techniques on Z using the Z-Beamlet laser", Review of Scientific Instruments 72, 657-662 (2001) https://doi.org/10.1063/1.1315645.

[61] Sinars, D.B., et al., Monochromatic x-ray imaging experiments on the Sandia National Laboratories Z facility (invited). Review of Scientific Instruments, 2004. 75(10): p. 3672-3677.

[62] Schollmeier, M.S., et al., A 7.2 keV spherical x-ray crystal backlighter for two-frame, two-color backlighting at Sandia's Z Pulsed Power Facility. Review of Scientific Instruments, 2017. 88(10).

[63] Rambo, P., et al. Sandia's Z-Backlighter Laser Facility. in 48th SPIE Annual Laser Damage Symposium on Optical Materials for High-Power Lasers. 2015. Boulder, CO.

[64] Sinars, D.B., et al., Enhancement of x-ray yield from the Z-Beamlet laser for monochromatic backlighting by using a prepulse. Review of Scientific Instruments, 2006. 77(10).

[65] Sinars, D.B., et al. 1- to 10-keV x-ray backlighting of annular wire arrays on the Sandia Z-machine using bent-crystal imaging techniques. in Conference on Laser-Generated and Other Laboratory X-Ray and EUV Sources, Optics, and Applications. 2003. San Diego, CA.

[66] Awe, T.J., et al., Experimental Demonstration of the Stabilizing Effect of Dielectric Coatings on Magnetically Accelerated Imploding Metallic Liners. Physical Review Letters, 2016. 116(6).

[67] T. Ao, M. Schollmeier, P. Kalita, P. D. Gard, I. C. Smith, J. E. Shores, C. S. Speas, and C. T. Seagle, "A spherical crystal diffraction imager for Sandia's Z Pulsed Power Facility", Review of Scientific Instruments 91, 043106 (2020) https://doi.org/10.1063/1.5132323.

[68] Gomez, Matthew R, Fein, Jeffrey R, Hansen, Stephanie B., Harvey-Thompson, Adam James, Dunham, Greg S, Knapp, Patrick, Slutz, Stephen Avery, Weis, Matthew Robert, Jennings, Christopher Ashley, Robertson, Grafton Kincannon, Speas, Christopher, Maurer, Andrew, Ampleford, David, Rochau, Gregory A., Doron, R., O. Nedostup, E., Stambulchik, Zarnitsky, Y., Maron, Y., Paguio, Reny, Tomlinson, Kurt, Huang, H., Smith, Gary, and Taylor, Randy. 2020. "Narrowband Self-Emission X-ray Imaging of MagLIF Targets on Z.". United States. https://doi.org/10.2172/1830902. https://www.osti.gov/servlets/purl/1830902.

[69] Harding, Eric, Schollmeier, Marius, Gomez, Matthew R, Knapp, Patrick, Hansen, Stephanie B., Robertson, Grafton Kincannon, Speas, Christopher, and Rochau, Gregory A. 2018. "Self-emission spherical crystal imaging at Z and plans for 3D imaging.". United States. https://www.osti.gov/servlets/purl/1512651.

[70] J. K. Vogel, M. J. Pivovaroff, B. Kozioziemski, C. C. Walton, J. Ayers, P. Bell, D. Bradley, M.-A. Descalle, S. Hau-Riege, L. A. Pickworth, D. J. Ampleford, C. R. Ball, C. J. Bourdon, J. R. Fein, P. D. Gard, A. Maurer, M. Wu, A. Ames, R. Bruni, S. Romaine, K. Kilaru, O. J. Roberts, and B. Ramsey , "Design and raytrace simulations of a multilayer-coated Wolter x-ray optic for the Z machine at Sandia National Laboratories", Review of Scientific Instruments 89, 10G113 (2018) https://doi.org/10.1063/1.5038811

[71] G. R. Laity, M. D. Johnston, S. Patel, and M. E. Cuneo, "Power Flow Spectroscopy Diagnostics & Platform Development at the Z Pulsed Power Facility". (2017) United States. https://doi.org/10.2172/1677519. https://www.osti.gov/servlets/purl/1677519.

[72] M.R. Gomez, R.M. Gilgenbach, M.E. Cuneo, C.A. Jennings, et al., "Experimental Study of Current Loss and Plasma Formation in the Z machine Post-hole Convolute," Physical Review Accel. & Beams, 20, 010401, 2017

[73] R.W. Olsen, "EG&G, Inc., Fast Streak Camera Operation," SPIE-High Speed Photography, Videography, and Photonics VI, 981, 71 (1988).

[74] Sydor Instruments, LLC, 291 Millstead Way Rochester, NY 14624, Phone: 585-278-1168, http://sydortechnologies.com/, info@sydorinstruments.com, ROSS 5100 Streak Camera Product Specifications Sheet.
[75] Spectral Instruments Inc. 420 N. Bonita Ave . Tucson, AZ 85745 . Ph. 520-884-8821 Fax 520-884-8803, Email info@specinst.com, web: www.specinst.com.
[76] Pi-Max/Pi-Max 2 system, ftp://ftp.princetoninstruments.com/public/Manuals/ Princeton%20Instruments/PI-MAX%20System% 20Manual.pdf.
[77] Mission Support and Test Services, LLC., New Mexico Operations, P.O. Box 809 Los Alamos, NM 87544. Technical Specifications Form, 200MHz VISAR APD Receiver.
[78] Hamamatsu Catalog Number KAPD1001E05, April 2004.
[79] Polymicro Technologies, LLC, 18019 North 25th Avenue Phoenix, Arizona 85023. Phone: (602) 375-4100, Fax (602) 375-4110. URL: http://www.polymicro.com.
[80] D. C. Lamppa, J. P. VanDevender, B. T. Hutsel, M. R. Jobe, C. Aragon, G. K. Robertson, G. R. Laity, M. R. Gomez, D. Ampleford, and M. E. Cuneo, "Diagnosing Z Machine Current Loss using Anode-Side Charged Particle Diagnostics." (2017). United States. https://www.osti.gov/servlets/purl/1465099.
[81] Myers, Clayton Edward, Gomez, Matthew R, Lamppa, Derek C., Webb, Timothy Jay, Yager-Elorriaga, David Alexander, Hutsel, Brian Thomas, Jennings, Christopher Ashley, Knapp, Patrick, Kossow, Michael Richard, Lucero, Larry Martin, Obregon, Robert J., and Steiner, Adam Michael. 2020. "Inductively driven transmission lines: Passively coupled devices for driving secondary loads on the Z Pulsed Power Facility.". United States. https://doi.org/10.2172/1835220. https://www.osti.gov/servlets/purl/1835220.
[82] Clayton E. Myers, Derek C. Lamppa, Christopher A. Jennings, Matthew R. Gomez, Patrick F. Knapp, Michael R. Kossow, Larry M. Lucero, James K. Moore, and David A. Yager-Elorriaga, "The inductively driven transmission line: A passively coupled device for diagnostic applications on the Z pulsed power facility", Review of Scientific Instruments 92, 033501 (2021) https://doi.org/10.1063/5.0043810
[83] S. M. Zakharov, G. V. Ivanenkov, A. A. Kolomenskii, S. A. Pikuz, A. I. Samokhin, and J. Ullschmeid. Wire X-pinch in a high-current diode. Sov. Tech. Phys. Lett., 8:456, 1982.
[84] T. A. Shelkovenko, S. A. Pikuz, and D. A. Hammer. A review of projection radiography of plasma and biological objects in X-pinch radiation. Plasma Phys. Reports, 42(3):226–268, 2016a. ISSN 1562-6938. doi:10.1134/S1063780X16030065.
[85] G. A. Shipley, C. A. Jennings, and P. F. Schmit, "Design of dynamic screw pinch experiments for magnetized liner inertial fusion", Physics of Plasmas 26, 102702 (2019) https://doi.org/10.1063/1.5120529
[86] D. B. Sinars, S. A. Slutz, M. C. Herrmann, R. D. McBride, M. E. Cuneo, C. A. Jennings, J. P. Chittenden, A. L. Velikovich, K. J. Peterson, R. A. Vesey, C. Nakhleh, E. M. Waisman, B. E. Blue, K. Killebrew, D. Schroen, K. Tomlinson, A. D. Edens, M. R. Lopez, I. C. Smith, J. Shores, V. Bigman, G. R. Bennett, B. W. Atherton, M. Savage, W. A. Stygar, G. T. Leifeste, and J. L. Porter , "Measurements of magneto-Rayleigh–Taylor instability growth during the implosion of initially solid metal liners", Physics of Plasmas 18, 056301 (2011) https://doi.org/10.1063/1.3560911
[87] https://www.edmundoptics.com/p/75mm-dia-x-400mm-fl-mgfsub2sub-coated-achromatic-doublet-lens/5884
[88] O.T. Strand, D.R. Goosman, C. Martinez, T.L. Whitworth, and W.W. Kuhlow. Compact system for high-speed velocimetry using heterodyne techniques. Review of Scientic Instruments, 77:83108, 2006.
[89] D.H. Dolan. Extreme measurements with Photonic Doppler Velocimetry (PDV). Review of Scientific Instruments, 91:051501, 2020.
[90] L.M. Barker and R.E. Hollenbach. Laser interferometer for measuring high velocities of any reflecting surface. Journal of Applied Physics, 43:4669-4675, 1972.
[91] D.H. Dolan. Foundations of VISAR analysis. Technical Report SAND2006-1950, Sandia National Laboratories, 2006.
[92] A. Porwitzky and J. Brown, “Uncertainties in cylindrical anode current inferences on pulsed power drivers” Phys. Plasmas 25, 063102 (2018).
[93] M. H. Hess, K. J. Peterson, D. J. Ampleford, B. T. Hutsel, C. A. Jennings, M. R. Gomez, D. H. Dolan, G. K. Robertson, S. L. Payne, W. A. Stygar, M. R. Martin, and D. B. Sinars, Phys. Plasmas 25, 042702 (2018).
[94] M. R. Gomez, S. A. Slutz, P. F. Knapp, K. D. Hahn, M. R. Weis, E. C. Harding, M. Geissel, J. R. Fein, M. E. Glinsky, S. B. Hansen, et al., IEEE Trans. Plasma Sci. 47, 2081 (2019).
[95] K. S. Bell. "PDV for Electron Density Measurements." (2019) https://www.osti.gov/servlets/purl/1644584.

[96] D. H. Dolan, S. Payne, K. Bell, B. Fox, and N. W. Moore, "Effects and mitigation of pulsed power radiation on optical fiber velocimetry", Physics of Plasmas 29, 053102 (2022) https://doi.org/10.1063/5.0088613.
[97] L.M. Barker and R.E. Hollenbach. Interferometer techniques for measuring the dynamic mechanical properties of materials. Review of Scientific Instruments, 36(11):1617, 1965.
[98] D.H. Dolan, R.W. Lemke, R.D. McBride, M.R. Martin, E. Harding, D.G. Dalton, B.E. Blue, and S.S. Walker. Tracking an imploding cylinder with photonic Doppler velocimetry. Review of Scientifc Instruments, 84:55102, 2013.
[99] J. G. Mance, B. M. La Lone, D. H. Dolan, S. L. Payne, D. L. Ramsey, and L. R. Veeser. Time-stretched photonic Doppler velocimetry. Opt. Express, 27(18):25022{25030, Sep 2019.
[100] Moore, N.W., K.S. Bell, H. Hilborn, et al., Sample test array and recovery (STAR) platform at the National Ignition Facility Review of Scientific Instruments 92, 053539 (2021); https://doi.org/10.1063/5.0043313.
[101] B. Jones et al., "A renewed argon gas puff capability on Sandia's Z machine," 2013 Abstracts IEEE International Conference on Plasma Science (ICOPS), 2013, pp. 1-1, doi: 10.1109/PLASMA.2013.6633169.
[102] P. Datte, J. Baker, D.E. Bliss, N. Butler, P. Celliers, S. Cohen, M. Crosley, J. Edwards, D. Erskine, D. Fratanduono, G. Frieders, J. Galbraith, M. Hess, D. Johnson, M. Jones, K. LeChien, J. Lusk, C. Myers, T. McCarville, R. McDonald, G. Natoni, M. Olson, K. Raman, G. Robertson, R. Shelton, J. Shores, S. Speas, D. Spencer, E. Vergel de Dios, and N. Wong, "The design of a line velocity interferometer for any reflector for inertial confinement experiments on the Z-machine," Rev. Sci. Instrum. 91, 043508 (2020).
[103] C.E. Myers et. al. "Spatially resolved measurements of load current delivery on a 14MA, 100 ns pulsed power experiment using a line-imaging velocity interferometer," submitted to Phys. Rev. Accel. Beams
[104] Hahn, K.D., et al., Fusion-neutron-yield, activation measurements at the Z accelerator: Design, analysis, and sensitivity. Review of Scientific Instruments, 2014. 85(4): p. 043507.
[105] K. D. Hahn, C. L. Ruiz, G. W. Cooper, A. J. Nelson, G. A. Chandler, R. J. Leeper, B. R. McWatters, R. M. Smelser, and J. A. Torres, "Calibration of neutron-yield diagnostics in attenuating and scattering environments", Review of Scientific Instruments 83, 10D914 (2012) https://doi.org/10.1063/1.4732067
[106] Ruiz, C.L., et al., Absolute Calibration of a Total Yield Indium Activation Detector for Dd and Dt Neutrons. Review of Scientific Instruments, 1992. 63(10): p. 4889-4891.
[107] C. L. Ruiz et al. "Novel beryllium-scintillator, neutron-fluence detector for magnetized liner inertial fusion experiments," PHYS. REV. ACCEL. BEAMS 22, 042901 (2019).
https://doi.org/10.1103/PhysRevAccelBeams.22.042901.
[108] R J Leeper et al. "ZR Neutron Diagnostic Suite" (2008) J. Phys.: Conf. Ser. 112 032076. doi:10.1088/1742-6596/112/3/032076
[109] C. L. Ruiz et al, "Multichannel, triaxial, neutron time-of-flight diagnostic for experiments at the Z facility," PHYS. REV. ACCEL. BEAMS 23, 020401 (2020). https://doi.org/10.1103/PhysRevAccelBeams.23.020401
[110] G. A. Chandler, C. L. Ruiz, G. W. Cooper, J. A. Torres, M. A. Mangan, G. M. Whitlow, D. J. Ampleford, M. C. Jones, R. A. Buckles, K. J. Moy, I. Garza, M. Staska, A. Wolverton, and B. Davis, "Neutron time-of-flight detectors (nTOF) used at Sandia's Z-Machine", Review of Scientific Instruments 93, 113531 (2022)
[111] J. P. Knauer et al., "Neutron time-of-flight measurements on the national ignition facility," 2011 Abstracts IEEE International Conference on Plasma Science, 2011, pp. 1-1, doi: 10.1109/PLASMA.2011.5992961.
[112] David J. Ampleford, Carlos L. Ruiz, David N. Fittinghoff, Jeremy D. Vaughan, Kelly Hahn, Brandon Lahmann, Maria Gatu-Johnson, Johan Frenje, Richard Petrasso, Christopher R. Ball, Andrew J. Maurer, Patrick F. Knapp, Adam J. Harvey-Thompson, John Fisher, Perry Alberto, Jose A. Torres, Gary Cooper, Brent Jones, Gregory A. Rochau, and Mark J. May, "One dimensional imager of neutrons on the Z machine", Review of Scientific Instruments 89, 10I132 (2018) https://doi.org/10.1063/1.5038118
[113] Kim, Y., et al. "DT gamma-to-neutron branching ratio determined from inertial confinement fusion plasmas." Physics of Plasmas 19.5 (2012): 056313.
[114] Malone, R. M., et al. "Design and construction of a Gamma reaction history diagnostic for the National Ignition Facility." Journal of Physics: Conference Series. Vol. 244. No. 3. IOP Publishing, 2010.
Mack, J. M., et al. "Observation of high-energy deuterium–tritium fusion gamma rays using gas Cherenkov detectors." Nuclear Instruments and Methods in Physics Research Section A: Accelerators, Spectrometers, Detectors and Associated Equipment 513.3 (2003): 566-572.
[115] Herrmann, Hans W., et al. "Cherenkov radiation conversion and collection considerations for a gamma bang time/reaction history diagnostic for the NIF." Review of Scientific Instruments 79.10 (2008): 10E531.

[116]Herrmann, Hans W., et al. "Diagnosing inertial confinement fusion gamma ray physics." Review of Scientific Instruments 81.10 (2010): 10D333.

[117] Rubery, M. S., et al. "Monte Carlo validation experiments for the gas Cherenkov detectors at the National Ignition Facility and Omega." Review of Scientific Instruments 84.7 (2013): 073504.
[118] Milnes, J. S., et al. "Ultra-high speed photomultiplier tubes with nanosecond gating for fusion diagnostics." Review of Scientific Instruments 83.10 (2012): 10D301.
[119] Kim, Y., et al. "Aerogel Cherenkov detector for characterizing the intense flash x-ray source, Cygnus, spectrum." Review of Scientific Instruments 87.11 (2016): 11E723.
[120] Kim, Y., et al. "Time-resolved measurements of Cygnus x-ray production using Aerogel Cherenkov Detector." 2017 IEEE 21st International Conference on Pulsed Power (PPC). IEEE, 2017.
[121] Meaney, Kevin Daniel, et al. "Characterization of the Mercury pulsed power x-ray source spectrum using multichannel density aerogel Cherenkov detectors." Review of Scientific Instruments 89.10 (2018): 10F113.
[122] Moran, M. J., Glebov, V. Y., Stoeckl, C., Rygg, R., & Schwartz, B. E. (2005). PROTEX: A proton-recoil detector for inertial confinement fusion neutrons. Review of scientific instruments, 76(2), 023506.
[123] Rowlands, J. A., Phys. Med. Biol. 47 (2002) R123–R166
[124] Maddox et. al., Rev. Sci. Instrum. 82, 023111 (2011); https://doi.org/10.1063/1.3531979.
[125] Meadowcroft et. al. Rev. Sci. Instrum. 79, 113102 (2008); https://doi.org/10.1063/1.3013123
[126] A. Konstantinidis, "2.02 - Physical Parameters of Image Quality," Editor(s): Anders Brahme, Comprehensive Biomedical Physics, Elsevier, 2014, Pages 49-63, ISBN 9780444536334, https://doi.org/10.1016/B978-0-444-53632-7.00202-1.
[127] Dunham et. al., Rev. Sci Instrum. 87, 11E301 (2016); doi: 10.1063/1.4955482
[128] D. B. Brown, J. W. Criss, and L. S. Birks, "Sensitivity of x-ray films. I. A model for sensitivity in the 1–100-keV region", Journal of Applied Physics 47, 3722-3731 (1976) https://doi.org/10.1063/1.323137
[129] Henke et. al., J. Opt. Soc. Am. B, Vol. 1, 6, December 1984.
[130] Henke et. al., Vol 1., No. 5. December 1984. J. Opt. Soc. Am. B, pages 828-849
[131] L. Claus, L. Fang, R. Kay, M. Kimmel, J. Long, G. Robertson, M. Sanchez, J. Stahoviak, D. Trotter, J. L. Porter, "An overview of the Ultrafast X-ray Imager (UXI) program at Sandia Labs," Proc. SPIE 9591, Target Diagnostics Physics and Engineering for Inertial Confinement Fusion IV, 95910P (31 August 2015); doi: 10.1117/12.2188336
[132] Quinn Looker, Anthony P. Colombo, Mark Kimmel, and John L. Porter, "X-ray characterization of the Icarus ultrafast x-ray imager", Review of Scientific Instruments 91, 043502 (2020) https://doi.org/10.1063/5.0004711
[133] Quinn Looker, Anthony P. Colombo, and John L. Porter, "Detector thickness effects on nanosecond-gated imager response", Review of Scientific Instruments 92, 053504 (2021) https://doi.org/10.1063/5.0048519
[134] G. A. Rochau, J. E. Bailey, G. A. Chandler, T. J. Nash, D. S. Nielsen, G. S. Dunham, O. F. Garcia, N. R. Joseph, J. W. Keister, M. J. Madlener, D. V. Morgan, K. J. Moy, and M. Wu, "Energy dependent sensitivity of microchannel plate detectors", Rev. Sci. Instrum. 77, 10E323 (2006); doi: 10.1063/1.2336461.
[135] Ming Wu, Ken Moy, Craig Kruschwitz, and Greg Rochau, "Characterizations of MCP performance in the hard x-ray range (6–25 keV)", Rev. Sci. Instrum. 85, 11D607 (2014); doi: 10.1063/1.4890293.
[136] Craig A. Kruschwitz, Ming Wu and Greg A. Rochau, "Monte Carlo simulations of microchannel plate detectors. II. Pulsed voltage results", Rev. Sci. Instrum. 82, 023102 (2011); https://doi.org/10.1063/1.3530451.
[137] Craig A. Kruschwitz, Ming Wu and Ken Moy, "Performance of microchannel plate-based detectors for <25 keV x rays: Monte Carlo simulations and comparisons with experimental results", Rev. Sci. Instrum. 92, 043101 (2021); https://doi.org/10.1063/5.0030514.
[138] G. A. Rochau, M. Wu, C. Kruschwitz, N. Joseph, K. Moy, J. Bailey, M. Krane, R. Thomas, D. Nielsen, and A. Tibbitts, "Measurement and modeling of pulsed microchannel plate operation", Rev. Sci. Instrum. 79, 10E902 (2008); doi: 10.1063/1.2965787.
[139] Ken Moy, Ming Wu, Craig Kruschwitz, Aric Tibbitts, Matt Griffin, Greg Rochau, "Dynamic characterizations of an 8-frame half-strip high-speed x-ray microchannel plate imager," Proc. SPIE 7079, Hard X-Ray, Gamma-Ray, and Neutron Detector Physics X, 70791B (5 September 2008); doi: 10.1117/12.795720.
[140] Craig A. Kruschwitz, Ming Wu, Ken Moy, and Greg Rochau, "Monte Carlo simulations of high-speed, time-gated microchannel-plate-based xray detectors: Saturation effects in dc and pulsed modes and detector dynamic range", Rev. Sci. Instrum. 79, 10E911 (2008); https://doi.org/10.1063/1.2969283.

[141] Ming Wu, Craig A. Kruschwitz, Dane V. Morgan, and Jiaming Morgan, “Monte Carlo simulations of microchannel plate detectors. I. Steady-state voltage bias results”, Rev. Sci. Instrum. 79, 073104 (2008); https://doi.org/10.1063/1.2949119.

[142] S. F. Khan, P. M. Bell, D. K. Bradley, S. R. Burns, J. R. Celeste, L. S. Dauffy, M. J. Eckart, M. A. Gerhard, C. Hagmann, D. I. Headley, J. P. Holder, N. Izumi, M. C. Jones, J. W. Kellogg, H. Y. Khater, J. R. Kimbrough, A. G. Macphee, Y. P. Opachich, N. E. Palmer, R. B. Petre, J. L. Porter, R. T. Shelton, T. L. Thomas, J. B. Worden, "Measuring x-ray burn history with the Streaked Polar Instrumentation for Diagnosing Energetic Radiation (SPIDER) at the National Ignition Facility (NIF)," Proc. SPIE 8505, Target Diagnostics Physics and Engineering for Inertial Confinement Fusion, 850505 (15 October 2012); https://doi.org/10.1117/12.930032.

[143] D. A. Yager-Elorriaga, Y. Y. Lau, P. Zhang, P. C. Campbell, A. M. Steiner, N. M. Jordan, R. D. McBride, and R. M. Gilgenbach, "Evolution of sausage and helical modes in magnetized thin-foil cylindrical liners driven by a Z-pinch", Physics of Plasmas 25, 056307 (2018)

[144] T. M. Hartsfield and D. H. Dolan, "Establishing temperature from radiance of dynamically compressed metals", Journal of Applied Physics 131, 185901 (2022)